NTNU

Norwegian University of
Science and Technology

Exploring Silica from Diatom Frustules as a High Performance, Low Cost and Environmentally Friendly Anode Material for Lithium Ion Batteries

Andreas Nicolai Norberg

Nanotechnology
Submission date: June 2017
Supervisor: Ann Mari Svensson, IMA
Co-supervisor: Nils Peter Wagner, IMA

Norwegian University of Science and Technology
Department of Materials Science and Engineering

Preface

This thesis describes the work carried out in the course TMT4910 Nanotechnology, Master's Thesis, during the spring 2017. Most of the experiments and analysis described in this work was carried out by the author, with the exception of the work on silicon and silica-silicon composites. This work was conducted in collaboration with master student Henning Kaland. In this collaboration, Kaland and the author did the work on the silicon and silica respectively. In addition, Kaland did the milling of silica. The nature of this collaboration is described in more details in the Appendix, section A7. As parts of this work resembles that of the project thesis "Anion Intercalation In Graphite Cathode", conducted by the author in the fall 2016, the theory section 2.1, 2.2 and 2.6 have some similarities. However, modifications and additions have been made.

I would like to thank my supervisor, Professor Ann Mari Svensson, for guidance, supervision and last but not least, the motivation and slack, that allowed me to pursue this work with genuine curiosity and excitement. Dr. Nils Peter Wagner also deserve huge thanks for helping me out when I needed it the most, both in the lab work and in writing this thesis. I also want to express my gratitude for the collaboration with Henning Kaland. It has been a real pleasure to have a fellow student in the lab, with whom to discuss crazy ideas, failures, breakthroughs and stuff that have nothing to do with science at all. Finally, I would like to thank the rest of the battery group at NTNU, for always being helpful.

The Research Council of Norway is acknowledged for the support to the Norwegian Micro- and Nano-Fabrication Facility (NorFab), project number 245963/F50.

Andreas Nicolai Norberg
23.06.2017, Trondheim

Abstract

In this work, silica extracted from diatom frustules was explored as a potential high performance, low cost and environmentally friendly anode material for lithium ion batteries. The diatom frustules were washed and calcined, and the resulting silica was characterized by scanning electron microscopy, X-ray diffraction and nitrogen adsorption. Electrodes of milled and unmilled silica were prepared with water soluble Na-alginate, different compositions of conductive additives and carbon coatings. In addition, the effect of the electrolyte additives, fluoroethylene carbonate and vinylene carbonate was explored. Coins cells and three electrode cells were assembled and characterized by galvanostatic cycling and electrochemical impedance spectroscopy. After cycling, post mortem characterization of the electrodes was performed by scanning electron microscopy, energy dispersive X-ray spectroscopy and focused ion beam characterization.

The capacity of the silica anodes was low during regular galvanostatic cycling for all electrode and electrolyte parameters. However, an electrochemical reduction program in combination with milled silica, was found to significantly increase the capacity of the best performing silica anode to an average capacity of 723 $\mathrm{mAhg^{-1}}$ after 50 cycles. In addition, the anodes exhibited excellent cycling stability and good rate capability up to 1000 $\mathrm{mAg^{-1}}$. Differential capacity analysis revealed that the capacity was caused by the conversion of silica to silicon, and subsequent lithiation of silicon. The conversion reaction during the electrochemical reduction step was found to be mainly driven by the reaction $2\,\mathrm{SiO_2} + 4\,\mathrm{Li^+} + 4\,\mathrm{e^-} \rightarrow \mathrm{Li_4SiO_4} + \mathrm{Si}$. Carbon coating the silica improved the initial capacity. However, no improvements were observed after 50 cycles. In addition, the carbon coating was found to contribute significantly to the capacity of the cell. For wide spread application of silica from diatom frustules to take place, the drawbacks of the electrochemical reduction program and the high first cycle irreversible capacity loss must be addressed.

Sammendrag

I arbeidet ble silika fra kiselalger utforsket som et potensielt høy ytelse, miljøvennlig og billig anode materiale for litium-ionebatterier. Kisel algene ble vasket og kalsinert, og den resulterende silikaen ble karakterisert ved hjelp av elektronmikroskopi, røntgendiffraksjon og nitrogen-adsorpsjon. Elektroder ble laget med både møllet og umøllet silika, vannløselig natrium alginat som bindemiddel og ulike tilsetningsstoffer for økt elektriske ledningsevnen. I tillegg ble effekten av å karbonkle silikaen undersøkt. Fluoroetylene karbonat og vinylene karbonat ble også undersøkt som tilsetningsstoffer i elektrolytten. Knappeceller og tre-elektrodeceller ble fabrikkert, og de elektrokjemiske egenskapene til elektrodene ble karakterisert ved hjelp av galvanostatisk sykling og elektrokjemisk impedans spektroskopi. Etter sykling ble elektrodene karakterisert ved hjelp av elektronmikroskopi, fokusert ionestråle og energidispersiv røntgenspektroskopi.

Kapasiteten til silika anoden var lav for alle elektrodene ved vanlig galvanostatisk sykling. En god gjennomsnittlig kapasitet på 723 $mAhg^{-1}$ etter 50 sykler, ble oppnådd ved å mølle silikaen og utsette den for et elektrokjemisk-reduksjonsprogram. Silikaen hadde også utmerket syklisk stabilitet og god rate-egenskaper opp mot 1000 mAg^{-1}. Differensiell kapasitets analyse viste at kapasiteten skyltes konvertering av silika til silisium, og videre litsiering av silisium. Kapasitetsøkningen under det elektrokjemiske-reduksjonsprogrammet skyldtes sannsynligvis reaksjonen: $2\,SiO_2 + 4\,Li^+ + 4\,e^- \rightarrow Li_4SiO_4 +$ Si. Den karbon kledde silikaen hadde anslagsvis høyere kapasitet, men etter 50 sykler var effekten utjevnet. I tillegg ble karbonet funnet å bidra signifikant til kapasiteten av batteriet. For at batterier med silika fra kiselalger skal ha et kommersielt potensial, må utfordringene med det elektrokjemiske-reduksjonsprogrammet og den høye initiale irreversible kapasiteten løses.

Table of Contents

Preface i

Abstract iii

Sammendrag v

List Of Abbreviations xi

1 Introduction 1

2 Theory 5

2.1 Galvanic cells and secondary batteries 5

2.1.1 The fundamental principles of secondary batteries 6

2.1.2 Energy density of batteries 7

2.1.3 Battery terminology 8

2.2 Cell components 10

2.2.1 Electrolytes and the solid electrolyte interface 10

2.2.2 Anode materials 13

2.2.3 Electrode binders 16

2.3 Si anodes 17

2.3.1 The convoluted nature of Si and SiO_2 anodes 17

2.3.2 Lithiation mechanism of Si 18

2.3.3 The challenges of Si anodes 19

2.3.4 SEI formation on Si anodes 20

2.4 SiO_2 anodes 21

2.4.1 Short review of SiO_2 anodes in the literature 22

2.4.2 Lithiation of SiO_2 24

2.4.3 Importance of carbon additives and carbon coatings 28

2.4.4 Importance of porosity 30

2.4.5 Importance of size . . . 31
2.5 SiO_2 from coscinodiscus diatoms . . . 31
2.5.1 Structure, morphology and the chemical composition of coscinodiscus diatoms . . . 31
2.5.2 Diatoms as battery anodes . . . 32
2.6 Characterization techniques . . . 33
2.6.1 Electrochemical characterization techniques . . . 33
2.6.2 Structural characterization techniques . . . 37
2.7 Notes on full cells and half cells . . . 39

3 Experimental **41**
3.1 Overview . . . 41
3.2 Preparation of the active material . . . 42
3.2.1 Extraction of SiO_2 from diatom algae . . . 42
3.2.2 Milling . . . 43
3.2.3 Carbon coating of SiO_2 . . . 43
3.2.4 Preparation of the alginate binder . . . 44
3.3 Characterization of the active material . . . 44
3.3.1 Laser diffraction . . . 44
3.3.2 Thermal gravimetric analysis . . . 45
3.3.3 X-ray diffraction . . . 45
3.3.4 Nitrogen adsorption measurements . . . 45
3.4 Slurries and electrode casting . . . 46
3.5 Electrolyte preparation . . . 47
3.6 Cell assembly . . . 48
3.6.1 Coin cells . . . 48
3.6.2 Three-electrode cells . . . 49
3.7 Electrochemical characterization . . . 49
3.7.1 Galvanostatic cycling . . . 50
3.7.2 Electrochemical impedance spectroscopy . . . 52
3.8 Structural characterization . . . 52
3.9 Report terminology and conventions . . . 53

4 Results **55**
4.1 Overview . . . 55
4.2 Characterization of extracted SiO_2 and active material . . . 55
4.2.1 Crystallinity . . . 55
4.2.2 Microstructure and morphology . . . 56

4.2.3 Particel size distribution 57
4.2.4 Surface area and porosity 59
4.2.5 Thermogravimetric analysis 60
4.3 Electrochemical characterization 61
4.3.1 Carbon cells 61
4.3.2 Phase 1: Initial screening of SiO_2 derived from diatom frustules . 63
4.3.3 Phase 2: Further investigation of electrochemical reduction of SiO_2 70
4.4 Characterization of electrodes pre- and post-cycling 80
4.4.1 Electrode microstructure and morphology 80
4.4.2 EDX mapping of electrode surface 87

5 Discussion **91**
5.1 Characterization of extracted SiO_2 and active material 91
5.1.1 Notes on extracted SiO_2 91
5.1.2 Characterization of active material 92
5.2 Capacity contribution from carbon 93
5.3 Initial screening of SiO_2 derived from diatom frustules 93
5.3.1 Capacity of SiO_2 anodes 93
5.3.2 Options for improving the capacity 95
5.3.3 Summary of initial screening 96
5.4 Electrochemical reduction as a performance enhancing technique 96
5.4.1 Increase in capacity by electrochemical reduction 96
5.4.2 Cycling stability and rate performance 97
5.4.3 Identifying the lithiation mechanism of SiO_2 98
5.4.4 Effect of carbon coating 101
5.4.5 Effect of electrolyte composition 104
5.5 SiO_2 from diatom frustules as an anode material 106

6 Conclusion **109**

7 Further work **111**

Appendix **I**
A1 Supplementary notes on experimental work I
A2 Supplementary data on characterization of frustules and active material . IV
A3 Experimental matrix for electrochemcial characterization IX
A4 Supplementary data on electrochemical characterization XI

A5 Supplementary SEM micrografs of electrodes XVI
A6 Supplementary EDX spectra XVIII
A7 Notes on Si anodes and collaboration with Henning Kaland XXIII

List Of Abbreviations

CCL	Cumulative capacity loss
Ce	Counter electrode
CE	Coulombic efficiency
CEI	Cathode electrolyte interface
CMC	Sodium carboxymethyl cellulose
CNT	Carbon nanotubes
cps	Counts per second
DI-water	Deionized water
DMC	Dimethyl carbonate
EC	Ethylene carbonate
EDX	Energy dispersive X-ray (spectroscopy)
EMC	Ethyl methyl carbonate
EMS	Ethyl methyl sulfone
FEC	Fluoroethylene carbonate
HRTEM	High-resolution transmission electron microscopy
ICL	Irreversible capacity loss
IPA	Isopropanol
Li-ion	Lithium ion
$LiPF_6$	Lithium hexafluorophosphate
NMP	1-methyl-2-pyrrolidone
PC	Propylene carbonate
PVDF	Polyvinylidene fluoride
Redox	Reduction-oxidation
REF	Reference electrode
SEI	Solid electrolyte interface
SEM	Scanning electron microscope
SOC	State of charge
S(T)EM	Scanning transmission electron microscope
TGA	Thermogravimetric analysis
VC	Vinylene carbonate
V_{OC}	Open circuit voltage
WE	Working electrode
XPS	X-ray photoelectron spectroscopy
XRD	X-ray diffraction

Chapter 1: Introduction

Energy technology has a vast impact on our society, ranging from geopolitics and economic development, environmental challenges, consumer electronics to transportation. Moving forward, the importance of energy technologies, such as batteries, is only set to grow.

Development of new battery technology will have a profound impact on our personal life and society at large. The improvement of high energy density batteries will continue to shape the development of new personal electronics and our way of transportation. In emerging economies, the development of cheap battery technology has the potential of drastically improving living standards. In this context, energy storage systems such as batteries, are key for developing local solar and wind power production, offering clean and decentralized energy to communities off central powered grids [1]. This could have a major impact on economic growth and social benefits in rural areas [2]. Finally, new battery technology is essential in combating pollution and global warming. To complete the transition to a carbon natural transportation system and solve the challenges of intermittent energy production, new and improved battery technology is vital [3].

For widespread application of battery technology to take place in these sectors, a variety of challenges must be overcome. The most prevalent challenge is the need to increase the energy density of batteries, while simultaneously decreasing the associated costs [1, 4]. In addition, an increase in battery production combined with a low expected battery life span, between five and eight years, will significantly increase the waste stream produced by the battery industry [5]. Thus, there is a growing expectation for batteries of the future to be composed of materials that are sustainable, environmentally friendly and abundant. Thereby, the main challenge is to develop environmentally benign batteries with improved energy density, at reduced cost. Moreover, the expected growth of the battery market is projected to 53 billion USD by 2024, providing significant economic incentive to solutions addressing this daunting challenge.

The research community has answered this challenge by greatly increasing the amount of research in this area. Interesting progress has been made on exotic battery technologies, such as Li-air, however, the main focus is still on Li-ion batteries. Another approach, is the attempts to replace carbon based anodes with silicon based anodes, as the silicon anodes offer almost 10 times the theoretical capacity of carbon [6]. However, the poor cycling stability of silicon anodes, caused by the dramatic volume change during lithiation/delithiation, continues to hamper the development of silicon anodes [7].

Over the last decade, silica has gained traction as an alternative to silicon. In contrast to silicon, silica has excellent cycling stability and a relative high theoretical capacity, estimated between 749 $mAhg^{-1}$ and 1673 $mAhg^{-1}$. In addition, silica is one of the most abundant materials on Earth and inherently environmentally friendly [8]. Thus, silica anodes could potentially increase the energy density of batteries, at low cost and in an ecologically acceptable manner.

The many benefits of silica make it an attractive material for use in battery anodes in a variety of different ways. Today, silica is used as an inexpensive feedstock in the production of Si nanoparticles for battery applications [9], structural additive in SiO_2/Si composites [10] and as the main active material in anodes [11]. The latter will be the focus of this work.

Silica is a promising anode material, however there are three significant challenges hampering the development of the anode material. First, the lithiation mechanism of silica is not well understood. The limited knowledge on the lithiation mechanism has made it difficult to reach capacities close to the theoretical limit of 1673 $mAhg^{-1}$. To the best of the author's knowledge, the highest reported reversible capacity of a silica anodes is 1055 $mAhg^{-1}$, after 150 cycles at 500 mAg^{-1} [12]. Thus, there is room for significant improvement before the theoretical capacity of 1673 $mAhg^{-1}$ is reached. Second, extensive use of carbon additives, such as carbon black, graphene and amorphous carbon coatings, make it difficult to compare results, as the capacity contribution from carbon is rarely reported [13, 14, 15]. This makes it difficult to judge the respective capacity contribution from carbon and silica. Third, in the effort to improve the capacity of silica anodes, more and more elaborate chemical synthesis techniques and expensive precursors are used to develop advanced silica structures [8]. Though many of these structures show promising results, this approach is counterproductive to the inherent benefits of silica, as a cheap and ecologically sustainable material.

In 2016, Nyesteen attempted to use silica from diatom frustules as an anode material [16]. His work showed great promise, with a reported capacity of 600 $mAhg^{-1}$ after 100 cycles. However, this result was achieved using a low current (50 mAg^{-1}) and a wide cycling window (0.0 V - 3.0 V). Moreover, the cells consisted of large amounts of amorphous carbon, making it difficult to distinguish between the capacity contribution from the silica and the amorphous carbon.

Aim of this Work

The main goal of this work is to address the third of the aforementioned challenges of silica anodes, by continue exploring highly porous silica from diatom frustules as potential high performance, low cost and environmentally benign anode material. The performance will be assessed on the specific capacity, cycling stability and the rate performance of the anode.

Moreover, this work will be conducted within the scope of four secondary goals: (1) Only utilize low cost and environmentally benign processing. (2) Conduct cycling under practical operation parameters (cycling window and current density). (3) Attempt to assess the lithiation mechanisms of SiO_2. (4) Explore the role of carbon additives/coatings, and their capacity contribution.

Chapter 2: Theory

The goal of this chapter is to provide a theoretical framework for further discussion throughout this report. First, an introduction to galvanic cells and secondary batteries is given, before the different components of a battery cell are described in more detail. This is followed by a further description of the working principle, challenges and benefits of silicon (Si) and silica (SiO_2) anodes. The final section covers characterization techniques relevant to this project.

Even though SiO_2 anodes is the main topic of this work, this chapter will draw upon research on Si anodes. The reason for this is twofold. First, as will be further explored in section 2.4, the chemistry of SiO_2 and Si is relatively similar. Second, SiO_2 anodes are a fairly new research topic, limiting the amount of published articles on the topic. Thus, publications on Si anodes may serve as a guide for predicting the behavior of SiO_2 anodes.

2.1 Galvanic cells and secondary batteries

A battery is by all intents and purposes a galvanic cell optimized for energy storage and delivering energy on demand. A galvanic cell is comprised of two electrically isolated electrodes, that when connected by an external circuit, converts chemical energy to electrical energy by a reduction-oxidation (redox) reaction. By convention, the electrode hosting the oxidation reaction, is termed anode, and the electrode hosting the reduction reaction, cathode [17].

Based on the reversibility of the reactions described above, battery technologies are divided into two main categories; primary batteries and secondary batteries. In a primary battery, the redox reactions are irreversible, meaning that they cannot be recharged. On the other hand, in secondary batteries, the redox reactions are partially reversible, making the battery rechargeable.

The reversibility of secondary batteries causes the electrodes in the cell to alternate between hosting the reduction and the oxidation reaction, depending on whether or not the battery is charged or discharged. For the ease of reading, the words cathode will in this work refer to the electrode at which reduction takes place as a battery discharge, and anode refer to the electrode at which oxidation takes place during discharging.

Today, a vast range of different secondary battery technologies exist, including lead-acid, nickel-cadmium and lithium ion (Li-ion). Moreover, interesting progress is done in new battery technologies, such as Li-Sulphur [18]. However, over the last decade, the growing market of consumer electronics and electrical vehicles has made Li-ion batteries one of the most dominant technologies in the secondary battery industry.

2.1.1 The fundamental principles of secondary batteries

A conventional Li-ion battery is made of two intercalating electrodes. The cathode is usually made of lithium transition metal oxides, such as $LiCoO_2$, while the anode is made of graphite. In addition to the two electrodes, a battery consists of two current collectors, electrolyte, a separator and different additives.

The role of the current collector is to provide good electrical contact between the electrode and the external circuit. The electrolyte, a good ionic conductor, allows for the movement of ions between the electrodes, but has limited electrical conductivity. The role of the separator is to mechanically separate the two electrodes. The property of the separator ensures that the electrolyte is kept between the two electrodes; at the same time it allows for ionic conduction, but electrically insulate the electrodes. Thus, the electrons are forced to go through the external circle. Finally, a polymeric component is used to ensure good adhesion between the active material particles in the electrodes.

The energy storage mechanism of Li-ion batteries is based on the shuttling of Li-ions between the two electrodes, giving it the trivial name "rocking chair battery" [19]. When charging, Li-ions move from the cathode into the graphite anode, as seen in Figure 2.1. During discharging, this process is reversed and the Li-ions move from the graphite anode, into the cathode. The reactions taking place during charging and discharging can be described by the following reactions [20]:

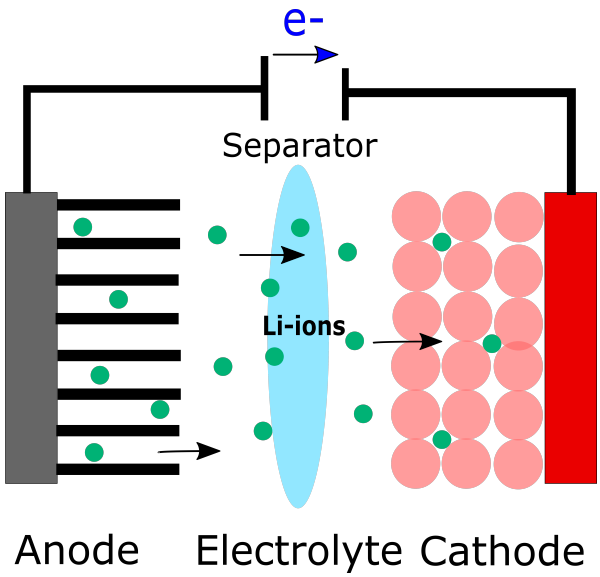

Figure 2.1: Schematic of a conventional Li-ion "rocking chair" battery with graphite anode. The directional flow of electrons and Li-ions during discharging is illustrated.

$$\text{Cathode:} \quad \mathrm{LiCoO_2} \rightleftharpoons \mathrm{Li_{1-x}CoO_2} + x\mathrm{Li^+} + x\mathrm{e^-} \tag{2.1}$$

$$\text{Anode:} \quad 6\mathrm{C} + x\mathrm{Li^+} + x\mathrm{e^-} \rightleftharpoons \mathrm{Li}_x\mathrm{C} \tag{2.2}$$

$$\text{Total Cell reaction:} \quad \mathrm{LiCoO_2} + 6\mathrm{C} \rightleftharpoons \mathrm{Li_{1-x}CoO_2} + \mathrm{Li}_x\mathrm{C} \tag{2.3}$$

2.1.2 Energy density of batteries

The amount of energy stored in this process is mainly dependent on two variables, the amount of charge transferred in reaction 2.3 and the potential at which the individual charge transfer happens. The total amount of energy stored in the charging process can then be expressed as:

$$\text{Energy} = \int_0^Q V(q)dq \tag{2.4}$$

where $V(q)$ is the potential when charge q is moved from one electrode to another, and Q is the total amount of charge taking place in process of charging the battery [21]. Equation 2.4 illustrates that the total energy of a battery can be improved by two fundamental approaches. One is to increase the total amount of charge involved in the process of charging (Q), the second to maximize the potential of the battery $(V(q))$ throughout

the charging cycle, often referred to as the voltage profile. In the latter case, one has to consider both the open circuit potential (V_{OC}) and the change in potential as a function of the state of charge (SOC).

V_{OC} of a full cell is given by the difference in electrochemical potential of the electrodes:

$$V_{\mathrm{OC}} = \frac{\mu_a - \mu_c}{e} \tag{2.5}$$

where μ_a, μ_c and e are respectively the chemical potential of the anode, the chemical potential of the cathode and the magnitude of an electron charge [21].

As a battery is charged or discharged, the potential of the cell diverge from the open circuit voltage due to two mechanisms. First, the potential of a cell varies with the state of charge (SOC), q_s, as the electrochemical potential of the two electrodes depends on SOC. Second, the potential is affected by polarization, η, creating an overpotential. Thus, the voltage profile during charging and discharging can be described by [21]:

$$V_{\mathrm{dis}} = V_{\mathrm{OC}}(q_s, I_{\mathrm{dis}}) - \eta(q_s, I_{dis}) \tag{2.6}$$

$$V_{\mathrm{ch}} = V_{\mathrm{OC}}(q_s, I_{\mathrm{ch}}) + \eta(q_s, I_{ch}) \tag{2.7}$$

The overpotential represents the deviation between the measured potential and the thermodynamically determined potential. In the context of batteries, there are three main sources of overpotentials; activation overpotential (η_{ac}), ohmic overpotential (η_{ohm}) and concentration overpotential (η_{cons}) [22]. The activation overpotential encompass the kinetic limitations of the reactions taking place at an electrode and creates an electrochemical energy barrier for activation. Ohmic overpotential represents the potential drop from the electrode to the local potential in the electrolyte. The ohmic overpotential is given by $\eta_{\mathrm{ohm}} = IR_e$, where R_e is the electrolyte resistance. The concentration overpotential results from concentration differences between the electrode surface and the bulk of the electrode, and can be seen as limitation on mass transfer. Even though the three sources of polarization have been discussed separately here, they should be considered interrelated.

2.1.3 Battery terminology

A wide range parameters have been developed to describe batteries performance. These parameters can roughly be divided into three main categories. Describing the amount of

energy a battery can store, the amount of power a battery can deliver and its life time. In addition, many of the different parameters are overlapping. Thus, satisfying information on the performance of a cell can be given by a selection of these parameters.

Energy density

The amount of energy stored in a battery is given by equation 2.4. However, to better reflect the utility of a battery in a practical setting, the energy density of a battery is usually given in terms of gravimetric energy density or volumetric energy density:

$$\text{Gravimetric Energy Density} = \frac{\int_0^Q V(q)dq}{wt} \tag{2.8}$$

$$\text{Volumetric Energy Density} = \frac{\int_0^Q V(q)dq}{vol} \tag{2.9}$$

Power density

For application of batteries in portable electronics, power tools and electrical vehicles, the power density of a battery is of great importance. The output power of a battery is given by [21]:

$$P(q) = V(q)I_{dis} \tag{2.10}$$

$$\text{Volumetric Power Density} = \frac{P(q)}{vol} \tag{2.11}$$

Battery life time and battery efficiency

The cycle life time of a battery is by convention given by the number of cycles the battery can perform until the capacity drops below 80 % of the initial reversible value [21].

The capacity loss of a single cycle is often given by the coulombic efficiency (CE) or the irreversible capacity loss (ICL), given by [21]:

$$\text{CE} = 100 \cdot \frac{Q_{\text{dis}}}{Q_{\text{ch}}} \tag{2.12}$$

$$\text{ICL} = Q_{\text{ch}} - Q_{\text{dis}} \tag{2.13}$$

where Q_{dis} is the capacity during discharging and Q_{ch} the capacity during charging of the same cycle. The total loss in capacity over multiple cycles, cumulative capacity loss (CCL), can be defined as:

$$\text{CCL} = \sum_{k} Q_{\text{ch}} - Q_{\text{dis}} \tag{2.14}$$

where k is the number of cycles.

2.2 Cell components

The goal of this section is to give a general introduction to the different components of a battery cell that are of importance to this work.

2.2.1 Electrolytes and the solid electrolyte interface

Over the last decades, there has been an enormous effort to develop new electrolytes for Li-ion batteries with the goal of increasing battery safety, the range of operation temperature and improve battery life time [23]. Moreover, with the emerging interest in alloying anodes, such as Si anodes, electrolyte compositions have become a vital tool for improving cycling stability [24].

2.2.1.1 Fundamentals of battery electrolytes

The main purpose of the electrolyte is to serve as a medium for ionic transport between the electrodes in the battery. However, to ensure good cell operation in rechargeable batteries, the electrolyte should satisfy these requirements [25]:

1. The electrolyte should be both a good ionic conductor and an electric insulator, i.e. so that the ions in the electrolyte are free to move, but self-discharge is limited.
2. The electrolyte should have a large voltage range at which it is neither oxidized nor reduced, often referred to as a electrochemical window.
3. It should be inert to the separator, electrode materials and cell packaging material.
4. It should be robust against chemical, electrical, thermal and mechanical abuse.
5. It should be non-toxic and environmental friendly.

The ability of an electrolyte to conduct ions can be quantified by the parameter, ionic conductivity, given by

$$\sigma = \sum_i N_i u_i Z_i e \tag{2.15}$$

where N_i is the number of moles of free ions, u_i the ion mobility, Z_i the valence of ionic species i and e the fundamental charge of an electron. It is often found that the ionic conductivity has a maximum at around 1 M salt. If the concentration of the electrolyte increases, it affects the N_i term in equation eq. (2.15) and the viscosity of the electrolyte, which again will reduce the ionic mobility of the electrolyte. Thus, most electrolytes have a critical concentration, at which a further increase in the concentration will cause a reduction in the ionic conductivity [26].

Electrolyte salts and solvents

To meet the aforementioned requirements, the electrolyte is usually comprised of a mixture of a salt, multiple solvents and electrolyte additives. The given composition is often dependent on the material system in question.

$LiPF_6$ is by far the most utilized salt in the industry and research community today, due to its well-balanced properties as an electrolyte salt [25]. However, electrolytes containing $LiPF_6$ have challenges related to sensitivity of moisture. If the electrolyte is contaminated with water, hydrofluoric acid might form [27]:

$$LiPF_6 \leftrightarrow LiF + PF_5 \tag{2.16}$$

$$PF_5 + H_2O \rightarrow 2\,HF + PF_3O \tag{2.17}$$

The formation of hydrofluoric acid might cause severe corrosion in the cell [27], and PF_5 is found to induce ring opening polymerization of EC, which significantly hampers the stability of the electrolyte [28, 29].

The main requirements for electrolyte solvents are to exhibit a high dielectric constant, so that the solvent can dissolve salts to sufficient concentrations and low viscosity to facilitate ion transport [25, 30]. To meet these somewhat contradicting requirements, most electrolytes are made of two or more solvents.

Non-aqueous electrolytes are often made by mixing cyclic carbonates, such as ethylene carbonate (EC) and propylene carbonate (PC), and linear carbonates such as dimethyl

carbonate (DMC) and diethyl carbonate (DEC). The chemical structure of these solvents are displayed in Figure 2.2.

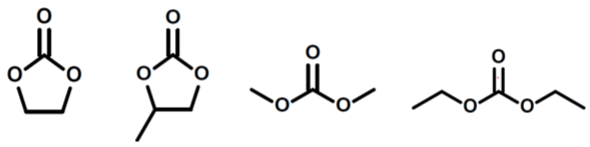

Figure 2.2: Chemical structure of common electrolyte solvents. From left to right EC, PC, DMC and DEC.

In general, the role of the cyclic carbonates is to solve the electrolyte salt, while the linear carbonates reduce the melting point and viscosity of the electrolyte. The properties of the electrolyte, such as melting point, conductivity, viscosity, reduction potential and oxidation potential, are highly dependent on the fraction of the different solvents in the mixture.

2.2.1.2 Electrolyte stability and the solid electrolyte interphase

The thermodynamic stability of electrolytes, often referred to as the electrochemical window, is given by the energy separation of the lowest unoccupied molecular orbital (LUMO) and the highest occupied molecular orbital (HOMO) [31]. For the electrolyte to be electrochemically stable, the electrochemical potentials of the electrodes must be within the electrochemical window. This is the case for some low potential batteries, such as Lithium Titanate (LTO). However, the V_{OC} of most high voltage batteries lie outside of the electrochemical window of most electrolytes. Thus, the requirement of electrolyte stability is usually met by kinetic stability, rather than thermodynamic stability [25].

The kinetic stability is mainly provided by the solid electrolyte interphase (SEI) forming on the electrodes. The interphase is formed by a complicated reduction process of electrolyte solvents and salts, resulting in a film consisting of both organic and inorganic decomposition products [33]. After formation, an ideal SEI prevents further decomposition of the electrolyte by limiting electron transport to the electrode surface. However, an ideal SEI should still enable diffusion of Li^+ from the electrolyte to the electrode surface.

An illustration of the electrochemical windows for different cell components are presented in Figure 2.3. For the electrolyte to be stable, the electrochemical potential of the electrodes must be within the electrochemical window (E_{g}). This is the case for the material

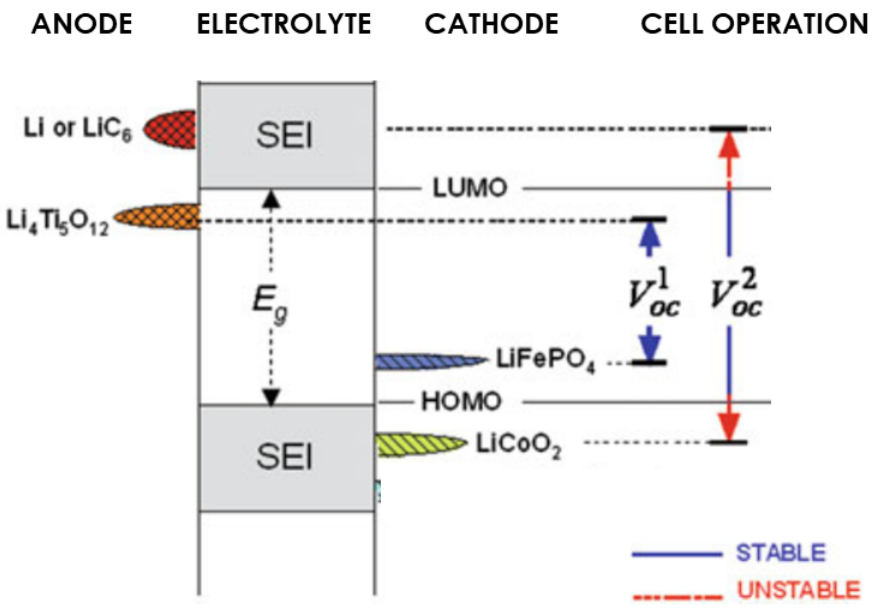

Figure 2.3: Schematic of the electrochemical window of an electrolyte. Modified illustration from [32].

system made of $Li_4Ti_5O_{12}$ and $LiFePo_4$, indicated by the potential V_{OC}^1. The electrochemical potential between the LiC_6 and $LiCoO_2$, indicated by the potential V_{OC}^2, is clearly outside the electrochemical window. However, in this case the initial decomposition of the electrolyte and the subsequent SEI formation stabilizes the cell.

Over the last years, a growing interest has been shown for the use of electrolyte additives to alter the properties of the SEI. As this topic is highly relevant to the material system in question, this topic will be discussed further in section about Si-anodes, 2.3.

2.2.2 Anode materials

Anodes materials can be divided into three main categories; intercalation anodes, alloying anodes and conversion anodes. In this section, the challenges and benefits of the different anodes are discussed. The theoretical capacity and estimated average lithiation potentials of a selection of anode material can be found in Table 2.1.

2.2.2.1 Intercalation anodes

Carbon

Intercalation refers to the reversible insertion of a guest molecule into a host lattice without altering the basic structure of the host lattice [34]. Due to its highly anisotropic structure, graphitic carbon is one of the most used intercalation compounds and is widely used in commercial batteries. The final product of reversible lithiated graphite is given by the reaction:

$$C_6 + Li^+ + e^- \rightleftharpoons LiC_6 \tag{2.18}$$

yielding a reversible capacity of 372 $mAhg^{-1}$ [35]. Due to the reasonable reversible capacity, low lithiation potential over almost the entire charge/discharge curve, graphite is one of the most used anode materials [36]. The capacity of amorphous carbon is well above graphite, over 900 $mAhg^{-1}$, but the material is hampered by low density and extensive SEI formation [37].

Table 2.1: Overview of theoretical capacity and estimated lithiation potentials of different anode materials.

Material	Type	Theoretical Capacity [$mAhg^{-1}$]	Approximate potential for lithiation [V vs Li/Li^+]
Graphite	Intercalation	372 $mAhg^{-1}$ [35]	0.2 [38]
Amorphous carbon	Intercalation	900 $mAhg^{-1}$ [37]	-
LTO	Intercalation	175 $mAhg^{-1}$ [39]	1.5[39]
Si	Alloying	4200 $mAhg^{-1}$ [7]	0.4 [7]
SiO_2	Conversion/ Alloying	1961 $mAhg^{-1}$ [14]/ 1673	-

Lithium titanate

In addition to graphite, $Li_4Ti_5O_{12}$ (LTO) is considered to be a viable intercalation anode. Due to its spinel structure, LTO can store lithium ions without any volume expansion, making it a "zero strain" material [40]. Moreover, the high operating voltage of LTO anodes ($\sim 1.5\ V$ vs Li/Li^+) prevents growth of Li dendrites, improving the safety of

operation [40]. The downside of LTO anodes is a low theoretical capacity of 175 $\mathrm{mAhg^{-1}}$ and low conductivity [40, 39].

In general, the insertion of Li species into intercalation compounds lead to small strains and minimum irreversible structural changes in the host material, giving intercalation anodes with good capacity retention [6]. However, the capacity of these anodes are usually far below that of alloy anodes and conversion anodes.

2.2.2.2 Alloy anodes

Lithium can also form alloys with different metals and metalloids, such as $\mathrm{Li}_x M_y$ (M = Al, Sb, Si, Sn, etc.) compounds [41]. In contrast to the intercalation mechanism, the alloying mechanism cause breaking of bonds between atoms in the host material, leading to significant structural changes [6]. However, the structural changes allow for higher specific capacities than seen in intercalation compounds. One example of this is the Li-Si alloy, were the $\mathrm{Li}_{4.4}\mathrm{Si}$ phase has a theoretical capacity of 4200 $\mathrm{mAhg^{-1}}$ [42]. Common for most alloy anodes are that they exhibit higher theoretical capacity than traditional intercalation compounds, but low cycling stability [43].

2.2.2.3 Conversion anodes

Conversion anodes are based on a conversion reaction between Li binary transition-metal $M_x y X_y$ compounds (M= Fe, Mn, Ni, Co, Cu, Si; X = O, S, P, S), exemplified by the general reaction [44]:

$$M_x X_y + y n_\mathrm{o} \mathrm{e}^- + y n_\mathrm{o} \mathrm{Li}^+ \leftrightarrow x M^0 + y \mathrm{Li}_{\mathrm{n_o}} X \qquad (M = \text{transition metal}) \tag{2.19}$$

where $\mathrm{n_o}$ is the oxidation state of the anion. Conversion anodes have theoretical discharge capacities exceeding traditional intercalation anodes. However, they also exhibit quite large voltage hysteresis, especially in the first cycle, reducing the efficiency of the electrode [45, 46]. In addition, because displacement reaction often occur at higher potentials and undergo structural changes during cycling, they tend to have quite sloping potential curves [47]. As alluded to in section 2.1.1, this could impede the energy density of batteries in accordance with equation 2.4.

2.2.2.4 Requirements of anode materials

Common for all anode materials is that they should fulfill six basic requirements [48]:

1. Accommodate as much Li as possible, but still be low weight.
2. The redox potential towards Li/Li^+ should be as small as possible at any concentration of Li^+.
3. Good electronic and ionic conductivity, allowing for fast transport of electrons and Li-ions.
4. The anode should not be soluble in the electrolyte solvent, or react with the electrolyte salt.
5. The material should be inherently safe
6. Low cost and environmentally friendly.

Today, these requirements are best met by the intercalation compound, graphite. However, with a theoretical capacity of only 372 $mAhg^{-1}$, graphite only satisfy requirement 1 to a limited degree. In addition, graphite anodes have challenges related to Li deposition and dendrite growth, which is a severe safety issue. Thus, efforts are made to develop new anode materials, which better satisfy the requirements above.

2.2.3 Electrode binders

In most electrodes, binders ensure good adhesion between the particles of the active material. In the case of Si anodes, the binder is also found to be of great importance in mitigating the volume expansion during cycling [49].

The most conventional binder is by far poly(vinylidenefluoride)(PVDF). However, as PVDF only forms week van der waals bonds to Si, it fails to accommodate the large volume expansion of Si [50]. Therefore, research on binders for Si anodes has focused on polymeric binders such as sodium carboxymethyl cellulose (CMC) and sodium alginate.

In contrast to Si, research on binders for SiO_2 is quite limited. However, as the surface chemistry of SiO_2 and Si is relatively similar, the choice of binder in this work was based on Si studies. Based on a literature review of Si anodes, sodium alginate was chosen as the preferred binder for this project. In contrast to CMC, Alginate is found to have a uniform distribution of carboxyl groups, which can form bonds to Si particles [49]. In

addition, alginate is found to facilitate transport of Li^+ through the binder layer and assist in the creation of the SEI layer [51].

The benefits of alginate compared to PVDF far exceed the improvement of cell performance. As PVDF is not water soluble, the Li-ion battery industry use 1-Methyl-2-pyrrolidone (NMP) as solvent. This imposes significant costs on Li-ion battery production, as the use of NMP requires heating systems for solvent evaporation and expensive recovery systems due to its toxicity [4]. Thus, the use of water soluble and environmentally benign binders, such as alginate, could significantly reduce production costs.

2.3 Si anodes

Si has long been a promising candidate to replace graphite as an anode material. This is mostly due to the desirable traits of Si [7]:

1. A high theoretical capacity.
2. The lithiation voltage of Si (0.10 V - 0.3 V [52]) gives a good balance between yielding a reasonable V_{OC} in a full cell and limiting lithium plating.
3. Si is abundant and relatively low cost.
4. Si is environmental friendly and non-toxic.

From the aforementioned reasons it is clear that Si satisfies many of the requirements for anode materials mentioned section 2.2.2.4. However, widespread commercialization of Si anodes has so far been hampered by the massive volume expansion of Si during lithiation [53]. To an extent, the emerging interest for SiO_2 anodes can be seen as a response to the challenging volume expansion of Si. Moreover, due to the many similarities of Si and SiO_2, a fundamental insight into Si anodes is necessary to understand the working principles, benefits and challenges of SiO_2 anodes.

2.3.1 The convoluted nature of Si and SiO_2 anodes

The convoluted nature of Si and SiO_2 anodes is best appreciated by the fact that the two materials are respectively oxidation and reduction products of each other. Thus, Si particles are often covered by a thin layer of SiO_2 [54], and the lithiation mechanism of SiO_2 involves the reduction of SiO_2 to Si. The latter will be covered in great detail when the lithiation mechanism of SiO_2 is discussed in section 2.4.2.

The relation between Si and SiO_2 is important to this work for two main reasons. First, the lithiation mechanism of SiO_2 involves the reduction of SiO_2 to Si [11]. Therefore, a fundamental understanding of the lithiation mechanism of Si is necessary to fully understand lithiation mechanism of SiO_2. Second, while SiO_2 anodes are a relative new research topic, Si anodes have been an area of intense research. Thus, based on the similar surface chemistry of Si and SiO_2, published articles on Si anodes may be assumed to serve as reasonable guidelines for research on SiO_2 anodes.

Following the arguments in the previous section, publications on the lithiation mechanism of Si, the effect of electrolyte composition on the performance of Si anodes and SEI formation on Si anodes are found to be of special interest to this work.

2.3.2 Lithiation mechanism of Si

Even tough Si anodes have been an area of intense research, the reaction mechanism between Si and Li^+ is not yet fully understood. Multiple Li_xSi compounds have been identified during lithiation, and the formation of these compounds are found to depend on both the speed of cycling and the lithiation cut-off potential [52].

Initially, the lithiation of Si was believed to lead to the formation of the most Li rich phase of the Li-Si system, $Li_{4.4}Si$, yielding a theoretical reversible capacity of 4200 $mAhg^{-1}$ [55, 7]. However, later studies have claimed that the $Li_{4.4}Si$ phase is not stable in room temperature and that the final lithiation product of Si in practical operation conditions is crystalline $Li_{3.75}Si$, yielding a theoretical capacity of 3579 $mAhg^{-1}$ [6, 56].

By studying the lithiation mechanism of Si-nanowires, Ogata et al. proposed a lithiation mechanism by which Li^+ first reacts with crystalline Si, forming a variety of amorphous Li_xSi phases, before crystalline $Li_{3.75}Si$ and an eventually an over-lithiated $Li_{3.75+\delta}Si$ phase is formed [52]. An overview of the proposed mechanism by Ogata et al is found in Table 2.2.

Ogata at al. also found that the composition of lithiated Si depends on the cycling rate and the lower cut-off potential. At slow cycling and a cut-off potential of 0.00 V, only the over-lithiated phase ($Li_{3.75+\delta}Si$) was identified. However, at medium cycling (119 mAg^{-1}) and a cut-off potential of 0.00 V multiple phases was present (a-Li_xSi for x = 2.0 - 3.5, a-Li_xSi for x = 3.5 - 3.75 , c-$Li_{3.75+\delta}Si$, c-$Li_{3.75-\delta}Si$).

Table 2.2: Lithiation and delithiation mechanism of Si proposed by Ogata et al [52]. Crystalline and amorphous phases are denoted by a and c respectively. δ describe the over-lithiated phase, were δ is in the range of 0.2 - 0.3.

Cycle/Stage	Reaction	Potential [V]
1st Lithiation		
	c-Si $\rightarrow$ a-Li_xSi $\rightarrow$ C-$Li_{3.75}Si$ $\rightarrow$ C-$Li_{3.75+\delta}Si$	0.10
$\geq$ 2nd Lithiation		
2	a-Si $\rightarrow$ a-$Li_{2.0}Si$	0.30-0.25
3	a-$Li_{2.0}Si$$\rightarrow$ a-$Li_{3.5}Si$	0.10
4	a-$Li_{3.75}Si$$\rightarrow$ c-$Li_{3.5}Si$	0.05
5	c-$Li_{3.75}Si$$\rightarrow$ c-$Li_{3.5+\delta}Si$	0.03
Delithiation		
1	$Li_{3.5+\delta}Si$ $\rightarrow$ c-$Li_{3.5}Si$ + c-$Li_{3.5-\delta}Si$	0.05 - 0.15
2	a-$Li_{3.5}Si$ $\rightarrow$ a-$Li_{2.0}Si$	0.27
3	c-$Li_{3.5}Si$ $\rightarrow$ a-$Li_{1.1}Si$	0.43
4	a-$Li_{2.0}Si$ $\rightarrow$ a-Si	0.50

2.3.3 The challenges of Si anodes

The main challenge of Si anodes is volume expansion, which during lithiation/delithiation could be as high as 400 % [42]. This structural change has a devastating effect on the cycling stability of the electrode due to multiple reasons [7]:

1. The electrode structure deteriorates during cycling and is gradually pulverized.
2. The expansion of Si may cause disconnection between the active material and the current collector.
3. The expansion and contraction of Si cause a "break and reform" mechanism of the SEI layer, causing continuous consumption of Li and SEI growth.

Over the last years, tremendous efforts have been made to address the challenges of volume expansion. The most common strategies are size reduction and nano structuring of Si to accommodate volume expansion [57], engineering stress relief matrices around the Si particles [42] and electrolyte additives that contributes to maintain the structural integrity of the electrode by forming more a durable and flexible SEI layer[58].

In the scope of this work, the latter approach is of interest, as research on SEI formation

on Si particles may provide useful insight into SEI formation on SiO_2 particles.

2.3.4 SEI formation on Si anodes

The electrolyte degradation mechanisms and subsequent film formation on Si surfaces during lithiation and delithiation, is to a large extent the same as for graphite, resulting in a film composed of mostly carbonates species and inorganic salts, such as Li_2CO_3, RCO_2Li and LiF respectively [59]. The major difference between the SEI on carbon and Si, is that the volume expansion of Si during lithiation prevents the formation of a stable SEI [59]. This leads to the continuous fracture of the SEI, exposing electrolyte to a fresh Si surface, causing continuous consumption of Li^+ and the formation of a thick SEI [42].

A successful approach to stabilize the SEI has been the addition of electrolyte additives such as Fluoroethylene carbonate (FEC) and Vinylene carbonate (VC) [60, 61]. These additives have reduction potentials above common electrolyte solvents, such as EC, enabling them to decompose and form stronger and more flexible SEI layers than traditional electrolyte solvents [60, 58].

2.3.4.1 Effect of electrolyte additives

VC is a well-known battery electrolyte additive and is believed to decompose to $ROCO_2Li$ and polycarbonates [61, 58]. On the other hand, the decomposition mechanism of FEC is still debated. One proposal is that FEC decomposes to LiF and polyene-compounds [62]. However, it has also been claimed that FEC first decompose to VC and HF, followed by the subsequent reduction of VC and the formation of polycarbonates [63].

The two additives are believed to improve the performance of Si anodes by different mechanism. VC is believed to produce a thin, smooth and flexible film which can withstand the volume expansion of Si without cracking [61, 58]. However, the downside of the dense film is that it is believed to exhibit a relative high resistance towards Li^+ diffusion [58]. In contrast, the film formed by FEC is believed to be less flexible and more porous leading to better conductivity of Li^+ through the film [58]. Thus, a combination of the two properties might be ideal.

A study comparing film formation caused by electrolytes with and without FEC on Si particles with different thickness of the outer SiO_2 layer found that increasing the SiO_2 thickness significantly reduced film formation [64]. This might suggest that less SEI is formed on SiO_2 relative to Si.

Reduction potentials of common electrolyte solvents and additives

A brief overview of the reduction potential of common electrolyte solvents and electrolyte additives is presented in Table 2.3. However, it should be noted that experimental values might deviate from tabulated values due to a variety of reasons, including differences in material system, electrolyte compositions and experimental parameters.

Table 2.3: Experimental reduction potential of common electrolyte solvents and additives.

Solvent	E_{red}(V vs. Li/Li^+)
EC	0.65 -0.9 [65]
DEC	0.80 [66]
EC/DEC	0.79 [11]
FEC	1.47 [58]
VC	1.04 -1.40 [65]

2.4 SiO_2 anodes

SiO_2 was long considered an electrochemical inactive material in the context of battery applications. However, in 2001 Gao et al. reported that SiO_2 nanoparticles were reactive towards Li^+ at potentials between 0.0 V and 1.0 V [67]. Later, the theoretical reversible capacity of SiO_2 has been estimated to be between 749 $mAhg^{-1}$ [68] and 1961 $mAhg^{-1}$ [11], depending on the lithiation mechanism. In addition to high capacity, SiO_2 is found to have excellent cycling stability [69]. Together, the high theoretical capacity of SiO_2, improved cycling stability, low cost and low toxicity, make SiO_2 an interesting material for anode applications in accordance with the requirements of anode materials.

In the literature, the topics of SiO_2 and silicon oxide (SiO_x for $0 < x < 2$) are discussed somewhat interchangeable. This is further complicated by the fact that there is no strict convention for SiO_x either. SiO_x is used both to describe core shell structures of Si and SiO_2, and homogeneous SiO_x particles [70]. Whether or not the homogeneous SiO_x particles consist of small nano domains of Si in a matrix SiO_2, or is one phase with both Si-Si and Si-O bonds, is still unknown, as both have been reported [71, 72]. This work will follow a convention where materials with large distinct regions of Si and SiO_2 (such as core shell Si/SiO_2 structures) are referred to as SiO_2/Si composites. The term SiO_x will only be used to describe homogeneous SiO_x particles, where the distribution of Si and SiO_2 is unknown.

2.4.1 Short review of SiO_2 anodes in the literature

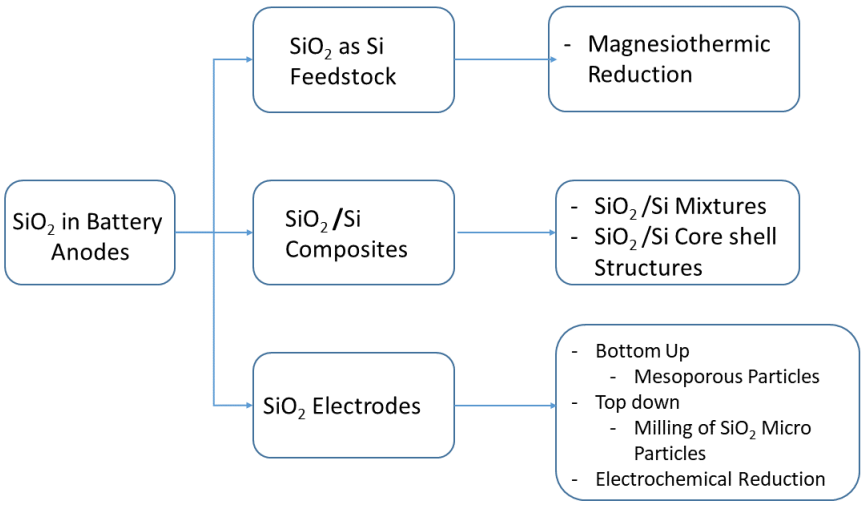

Figure 2.4: Schematic illustrating the use of SiO_2 as an anode material in the literature.

The discussion regarding SiO_2 as an anode material in the literature can be divided into three categories; SiO_2 as a feedstock for Si anodes, SiO_2/Si composites and anodes with SiO_2 as the main active materials.

SiO_2 as a feedstock for production of Si

Due to the abundancy and low cost of SiO_2, attempts have been made to use SiO_2 as a cheap feedstock for production of Si anodes. The SiO_2 feedstock comes from a variety of sources, including SiO_2 fumes collected as a waste product from elemental silicon production [73] and SiO_2 from algae frustules [74]. SiO_2 nanoparticles may also be produced by chemical methods and later reduced to Si nanoparticles [75]. Common for these approaches are that the preferred reduction technique is magnesiothermic reduction[73, 9, 75, 76].

SiO_2/Si composites

Due to the many similar properties of SiO_2 and Si explored in section 2.3.1, multiple attempts have been made to make SiO_2/Si composites. In these composites, the presence of SiO_2 and subsequent formation of $Li_2Si_2O_5$, Li_4SiO_4 and Li_2O, is believed to improve cyclability by buffering the expansion of Si [77, 78, 10, 79].

Table 2.4: Overview of reported capacities of anodes where SiO_2 is used as a feedstock for Si production.

Material		Current density [mAg^{-1}]	Reversible capacity [$mAhg^{-1}$]	Cycles
Diatomite-derived nanosilicon	[74]	700	1102	50
Reduced SiO_2 fumes	[73]	1800	1539	1000
Reduced porous SiO_2	[75]	1000	1639	100
Reduced mesoporous SiO_2	[76]	2000	715	100

The SiO_2 composites can roughly be divided into three different categories. In the first category, SiO_2 and Si particles are simply mixed together [78]. A second approach is to derive core shell structures, where the Si is covered by a layer of SiO_2 [10, 80]. In this case, the outer SiO_2 layer is showed to form a compressive shell around the Si particle and thereby limit the volume expansion of Si [80]. A final approach is to prepare SiO_2/Si composites through reduction or oxidation. This can be done by either partially reducing SiO_2 into Si by magnesiothermic reduction [77], or oxidizing Si into SiO_2 through ball milling [81]. An overview of reported capacities of SiO_2/Si composites can be seen in Table 2.5.

Table 2.5: Overview of reported capacities of anodes with SiO_2/Si composites as the main active material

Material		Current density [mAg^{-1}]	Reversible capacity [$mAhg^{-1}$]	Cycles
Nano SiO_x/C composite	[82]	100	$\sim$ 800	50
Graphene/SiO_x/C composite	[83]	100	630	250
Si/SiO_2/C composite	[77]	50	482	100
Si/SiO_2 composite	[79]	100	700	90
Core shell Si/SiO_2/C structure	[10]	100	786	100
Si/SiO_2/C nanofibers	[78]	100	$\sim$ 750	100
Mesoporous carbon-Si-SiO2 composite	[84]	100	920	100

Anodes with SiO_2 as the main active material

SiO_2 is also utilized as the main active material. In this case, the use of SiO_2 can be further divided into three categories. Synthesis of porous SiO_2 structures by wet

chemical methods [13, 85, 83, 86, 14, 87, 15, 88], milling of SiO_2 microparticles [8] and electrochemical reduction of SiO_2 by implementing hold steps at low potentials [70]. In most of these cases, carbon is added to further improve the performance of the electrode. The beneficial effects of carbon will be further discussed in section 2.4.3. An overview of the reported capacities in the literature can be found in Table 2.6. To the best of the authors knowledge, the highest capacity reported so far for SiO_2 anodes is 1055 $mAhg^{-1}$ at a current density of 500 mAg^{-1} after 150 cycles, reported by Cao et al. [12].

Over the last years, porous SiO_2 structures have by far been the most studied. In general, these structures have a relatively high capacity, improved cycling stability relative to Si and Si/SiO_2 anodes, and good rate capabilities. The role of the porous structure in achieving these results will be further discussed in section 2.4.4.

Milling of as received SiO_2 microparticles have also shown great promise. Chang et al. showed in 2012 that 300 nm SiO_2 particles from milled microparticles could achieve capacities up to 800 $mAhg^{-1}$ after 200 cycles at 100 mAg^{-1} [8]. In 2016 Lepoivre et al. demonstrated that SiO_2 nanoparticles could be electrochemical activated by holding electrodes at 2 mV for longer time periods, increasing the capacity of the cell by $\sim$ 150 $mAhg^{-1}$ after a hold time of 48 h [70].

2.4.2 Lithiation of SiO_2

Lithiation mechanism of SiO_2

The lithiation mechanism of SiO_2 was first examined by Sun et al. [68]. Experimental data from High-resolution transmission electron microscopy (HRTEM) and XPS (X-ray photoelectron spectroscopy), suggested the following reversibly conversion reactions and subsequent alloying reaction:

$$5\,SiO_2 + 4\,Li^+ + 4\,e^- \leftrightarrow 2Li_2Si_2O_5 + Si \tag{2.20a}$$

$$Si + xLi^+ \leftrightarrow Li_xSi \tag{2.20b}$$

The reversibility of this reaction was in particular attributed to the reversible O 1S shift in XPS measurements during cycling, indicating that $Li_2Si_2O_5 + Si$ is reversible formed [68]. Furthermore, Sun et al. measured a reversible discharge capacity above 416 $mAhg^{-1}$, which is above the theoretical capacity of reaction 2.20a (357.3 $mAhg^{-1}$). Thus, they argued that reaction 2.20a had to be followed by reaction 2.20b. However, in 2008 Guo

Table 2.6: Overview of reported capacities of anodes with SiO_2 as the main active material.

Material		Current density [mAg^{-1}]	Reversible capacity [$mAhg^{-1}$]	Cycles
Porous SiO_2 structures				
SiO_2 nanoporous tree-like SiO_2 film	[87]	120	247	300
SiO_2-graphene aerogel composite	[15]	500	$\sim$ 300	300
Hollow porous SiO_2 nanocubes	[14]	100	919	30
Amorphous SiO_2/C composite	[88]	100	600	100
SiO_2/C nanospheres	[85]	-	$\sim$ 876	500
Mesoporous SiO_2/C composite	[13]	100	$\sim$ 550	180
Nano SiO_2/C composite	[11]	100	$\sim$ 550	180
Mesoporous C/SiO_2/C composite	[12]	500	$\sim$ 1055	150
Mesoporous SiO_2/C/graphene composite	[89]	50	428.5	100
Porous SiO_2-carbon nanocaomposites	[90]	100	635.7	200
Hollow submicron SiO_2 carbon composite	[86]	70	662	100
As Received micro/nano particles				
7 nm SiO_2 Nanoparticles	[67]	50	$\sim$ 200	-
Nanosilica/carbon composites	[91]	100	620	100
Milled SiO_2				
Milled SiO_2	[8]	100	$\sim$800	200
Electrochemical activated SiO_2	[70]	480	$\sim$ 400	150

et al. observed a permanent redshift in XPS data of the O 1s peak attributed to Li_4SiO_4, suggesting the presence of an irreversible reaction and an alternative reaction mechanism [11]. In addition, they observed a broadening of the Si 2p peak, which suggested that multiple Si compounds were present after cycling. Without excluding the formation of additional silicates, Guo et al. proposed the following reaction mechanism:

$$SiO_2 + 4\,Li^+ + 4\,e^- \rightarrow 2Li_2O + Si \tag{2.21a}$$

$$2\,SiO_2 + 4\,Li^+ + 4\,e^- \rightarrow Li_4SiO_4 + Si \tag{2.21b}$$

$$Si + xLi^+ \leftrightarrow Li_xSi \tag{2.21c}$$

In this case both, reaction 2.21a and reaction 2.21b are irreversible, while reaction 2.21c

is responsible for the reversible capacity. A later study by Chang et al. proposed the lithiation mechanism of SiO_2 to be a combination of reaction 2.20a, reaction 2.21a and reaction 2.21c [8]. However, the reaction mechanism is still debated, illustrated by the study of Tekazawa et al, who claimed to have identified the formation of an additional lithium silicate, $Li_2Si_2O_3$ in the reaction with nonstoichimetric SiO_x and Li^+ [92].

Based on this short review, the lithiation mechanism of SiO_2 appears to be driven by at least three main reactions, followed by the lithiation mechanism of Si:

$$5\,SiO_2 + 4\,Li^+ + 4\,e^- \leftrightarrow 2Li_2Si_2O_5 + Si \tag{2.22a}$$

$$2\,SiO_2 + 4\,Li^+ + 4\,e^- \rightarrow Li_4SiO_4 + Si \tag{2.22b}$$

$$SiO_2 + 4\,Li^+ + 4\,e^- \rightarrow 2Li_2O + Si \tag{2.22c}$$

$$Si + xLi^+ \leftrightarrow Li_xSi \tag{2.22d}$$

Lithiation potentials of SiO_2

The reported onset potentials for the different reactions vary in the literature. This is expected as these potentials will vary with factors such as particle size, crystallinity and electrode composition. Attempts to probe the lithiation potential of SiO_2 has also been done with density functional theory. A brief overview of the reported onset potentials for lithiation and delithiation of SiO_2 can be found in Table 2.7. Please note that some of the cited articles in the table identify a potential for multiple reactions, i.e. do not distinguish between reactions 2.22a-2.22c.

2.4.2.1 Theoretical capacity of SiO_2 anodes

The discussion above illustrates the complex nature of SiO_2 anodes. SiO_2 can be viewed as a combination of a conversion anode (reactions 2.22a-2.22c) and an alloying anode (reaction 2.22d). The complex nature of SiO_2 anodes also makes it difficult to estimate a theoretical capacity, as it is highly dependent on the relative contribution from the conversion reaction, and the alloying reaction of Si.

Most publications on the topic cite a theoretical reversible capacity of SiO_2 at 1961 $mAhg^{-1}$, based on reaction2.22c. However, this is based on the formation of $Li_{4.4}Si$, which according to the discussion on the lithiation mechanism of Si in section 2.3.2, is highly unlikely. This is also supported by the fact that only $Li_{3.75}Si$ has been identified in post mortem analysis of SiO_2 anodes so far [8].

Table 2.7: Reported lithiation and delithiation potential of different Si compounds found in the literature on SiO_2 anodes.

Reaction	Potential [V]
Theoretical	
$0.8\ SiO_2 \rightarrow 0.4\ Li_2Si_2O_5 + 0.2\,Si$	1.38 [93]
$0.4\ Li_2Si_2O_5 + 0.533\,Li \rightarrow 0.133\ Si + 0.667\ Li_2SiO_3$	1.32 [93]
$Li_2SiO_3 + 0.667Li \rightarrow 0.167\ Si + 0.5\ Li_4SiO_4$	0.68 [93]
$SiO_2 + 4Li \rightarrow Si + Li_2O$	0.19 [94]
Experimental, lithiation	
$5SiO_2 + 4\,Li^+ + 4\,e^- \leftrightarrow Li_2Si_2O_5 + Si$	0.27 [8]
$2\ SiO_2 + 4\ Li \rightarrow Si + Li_4SiO_4$	0.24 [8, 11]
$SiO_2 + 4Li \rightarrow Si + 2Li_2O$	0.72 [85]
$15\ Li^+ + 4Si + 15\ e^- \rightarrow Li_{15}Si_4$	0.00 [8], 0.24 [11], 0.4 [85]
Experimental, delithiation	
$Li_2Si_2O_5 + Si \leftrightarrow 5SiO_2 + 4\,Li^+ + 4\,e^-$	0.27 [8]
$Li_{15}Si_4 \rightarrow 15\ Li^+ + 4Si + 15\ e^-$	0.34 [8]

The theoretical capacity of an anode based on the mass of the anode material before lithiation is given by:

$$Q_{\mathrm{T}}[\mathrm{mAhg}^{-1}] = \frac{n\mathrm{F}}{3.6 \cdot M_{\mathrm{w}}} \tag{2.23}$$

were n is the number of charge carriers (electrons), F is Faraday constant and M_{w} is the molecular weight of the anode material. The theoretical capacity of SiO_2 calculated on the basis of the resulting Si formed by reactions 2.22a-2.22c are presented in Table 2.8.The calculations are based on $Li_{3.75}Si$ being the fully lithiated state of Si, and that the reactions reactions 2.22a-2.22c are irreversible.

Table 2.8: Theoretical capacity of different lithiation mechanism of SiO_2, based on the subsequent alloying of Si (formation of $Li_{3.75}Si$) and weight of the anode material before lithiation.

Reaction	Q_T [$mAhg^{-1}$]
$5\,SiO_2 + 4\,Li^+ + 4\,e^- \rightarrow 2Li_2Si_2O_5 + Si$	335
$2\,SiO_2 + 4\,Li^+ + 4\,e^- \rightarrow Li_4SiO_4 + Si$	836
$SiO_2 + 4\,Li^+ + 4\,e^- \rightarrow 2Li_2O + Si$	1673

Optimizing the capacity of SiO_2 anode

In order to achieve the highest possible capacity, attempts should be made to increase the yield of reaction 2.22c. Guo et al. hypothesized that larger SiO_2 particles tend to form Li_4SiO_4, while smaller SiO_2 particles form Li_2O [11]. However, data supporting this argument have not been found elsewhere in the literature.

Cycling stability

In addition to the high capacity, SiO_2 is found to have excellent cycling stability compared to Si. The cycling stability is believed to be caused by the formation of $Li_2Si_2O_5$, Li_4SiO_4 and Li_2O during cycling. During the initial cite a matrix with domains of the reaction products and Si is believed to be formed, which provides structural support that buffer the volume expansion of the Si [77, 78, 10, 79].

Ionic and electric conductivity

In general, SiO_2 has a low electric conductivity, caused by a large band gap of approximately 3.5 eV [95]. However, Zhang et al. have shown that the conductivity of SiO_2 may increase with the addition of Li, significantly decreasing the band gap with the formation of compounds such as Li_xSiO_2.

Whether or not SiO_2 materials are good ion conductors is debated. In some cases, SiO_2 is reported to be an ionic insulator, preventing Li^+ diffusion through electrodes [54]. However, other studies have pointed out that Li^+ diffusion in SiO_2 is relatively fast [93].

Furthermore, is has been suggested that some of the formation products, Li_4SiO_4 and $Li_2Si_2O_5$, may increase Li^+ diffusion. Especially Li_4SiO_4 has been shown to exhibit excellente ion conductivity [96]. $Li_2Si_2O_5$ has a open tunnel structure along one the crystal axis, which have been proposed to serve as an easy diffusion path for Li^+ [8]. However, the author have found limited other evidence supporting these claims.

2.4.3 Importance of carbon additives and carbon coatings

By studying Table 2.6, it is evident that carbon has been important in the development of SiO_2 anodes. Carbon is usually used in two different ways, as conductive additives in the electrode matrix, or as a coating on the SiO_2 particles. Carbon black (CB) and graphene

are usually used as conductive additives, while carbon precursors, such as cornstarch and sucrose, are used to form carbon coatings.

The carbon additives, such as CB, improve the conductivity of the electrode by improving particle-particle conductivity and by forming a conductive network within the electrode [97]. This network allows for easy transport of electrons form the current collector to the active material. However, by investigating the effect of both CB and carbon coatings, Yao et al. found that carbon coated SiO_2 showed lower charge transfer resistance than cells with equal amounts carbon, but in the form of CB [98].

The main role of the carbon coating is to reduce particle-particle resistance, improve mechanical strength against volume expansion and provide chemical stability that protects the active material against corrosion [99]. As SiO_2 is a relatively poor electrical conductor, carbon coating the SiO_2 particles might reduce the interface resistance by distributing accessible electrons around the particles, resulting in homogeneous diffusion of ions through the particle, as illustrated in Figure 2.5 [99]. There by the active area of the particle is increased. By improving the conductivity of the electrode, conversion of SiO_2 to Si might be improved and heat generation during charging and discharging is reduced, thereby improving the efficiency, safety and calendar life of the cell.

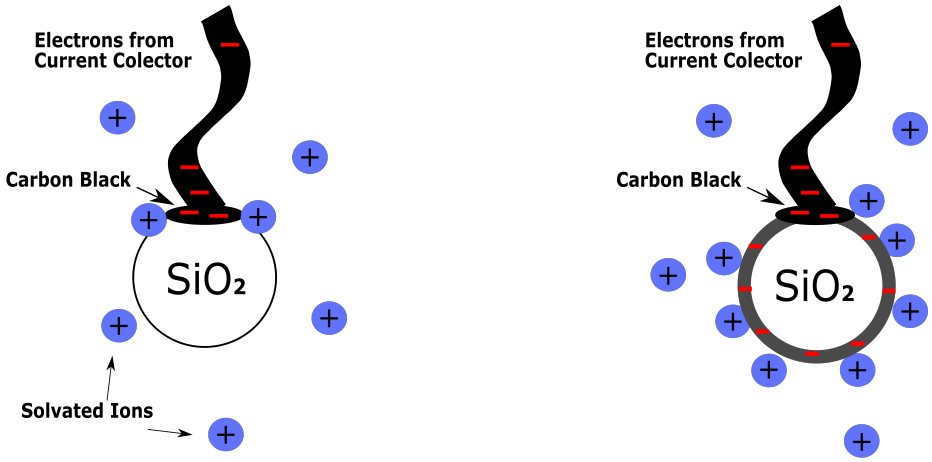

Figure 2.5: Schematic illustrating the effect of carbon coating. (a) Electrons are only supplied through the point of contact of carbon black. (b) Carbon coating allowing for even distribution of electrons around the entire surface of the particle. With inspiration from [99].

The wide use of carbon coatings in SiO_2 anodes also impose a challenge. The coating have a catalytic effect on SEI formation, and thereby increase the amount of SEI formed on the electrode. In addition, as noted by Dahn et al, different types or carbon and carbons

produced under varying processing conditions, such as pyrolysis time, might results in carbons with different capacities [37]. This makes it difficult to compare the reported capacities of different SiO_2/C or Si/SiO_2/C anodes, as the capacity contribution from carbon is rarely stated. Thus, great care must be taken when comparing results from electrodes with different types or carbon.

2.4.4 Importance of porosity

Over the last years a wide variety of nanoporous SiO_2 structures have been made, including porous nanocubes [14], porous nanospheres [85], hollow porous nanospheres [13] and nanoporous SiO_2 trees [87].

The porous structures are believed to be beneficial in multiple ways. First, the porous structure provide easy electrolyte penetration into the electrode [84]. Second, the mesoporous structure provide a short diffusion path for Li ions between the electrolyte and the active material, providing excellent rate capabilities [88, 83]. Third, the porous structure also buffers the volume change during lithiation, thereby preventing reformation of SEI during cycling.

Furthermore, it has been hypothesized that the porous structure can serve as a Li^+ surface storing cite, where Li^+ can be accommodated on the surface of the porous structure [87]. Lepoivre at al. have also hypothesized that the low conductivity of SiO_2 prevents the lithiation beyond a depth of 45 nm - 50 nm [70]. If this is the case, increase the surface area tough porosity might be vital to achieve high capacity SiO_2 anodes. However, these benefits of porosity may only be realized if the pores are larger than the volume of a solvated ion. In this case, microporous structures (2nm $<$) are considered too small to readily accommodate solvated Li-ions [100]. Thus, mesoporous structures (2 nm $\geq$) should be ideal.

There are also some challenges related to porous structures. In general, the porous structure result in a quite large first cycle ICL [13]. This capacity loss is mainly attributed to the irreversible formation of compounds such as Li_2O and Li_4SiO_4 and extensive SEI formation due to the high surface area. In addition to the high capacity loss, the synthesis of porous materials require quite complex procedures and high cost precursors [8]. This could add significant cost to material production, which directly work against the initial benefit of SiO_2 being a low cost alternative.

2.4.5 Importance of size

As noted earlier, it was long believed that SiO_2 was unreactive towards Li in conditions suitable for battery applications. However, since Gao et al demonstrated the reactivity of 7 nm SiO_2 nanoparticles towards lithium, it has been believed that a sufficient small size is crucial to make SiO_2 electrode reactive. As noted by Gao et al., the theoretical explanation for the increased reactivity with size reduction is based on the changes in thermodynamic properties with large changes in surface to volume rations of nanoparticles [67].

A short review of the literature summarized in Table 2.6, reveals that most of the particles studied are in the size range 100 nm - 500 nm [84, 85, 14, 87, 88]. In some cases, good electrochemical performance is also reported for SiO_2 particles between 500 nm - 1000 nm [86, 13]. Even tough these are quite large structures, most of them have porous structures on the order of 10 nm - 100 nm. The importance of size is exemplified by the work of Lv et al., which demonstrated that milling of 200 nm - 300 nm amorphous SiO_2 particles significantly increase the capacity from approximately 100 $mAhg^{-1}$ to 600 $mAhg^{-1}$ [88].

2.5 SiO_2 from coscinodiscus diatoms

Coscinodiscus diatoms, a unicellular algae, have long been studied for different applications ranging from filtration systems to optoelectronics [101]. The main feature of interest is in the algae the shell, often called the frustule. The frustule is a highly porous three dimensional bioinorganic scaffold made of SiO_2.

2.5.1 Structure, morphology and the chemical composition of coscinodiscus diatoms

As seen in Figure 2.6, the frustule of Coscinodiscus diatoms consists of four main structures; foramen, areola, cribrum and cribellum. According to Losic et al., the layers have different morphology and microstructure, that roughly can be described as follows [101]:

- Cribellum: Hexagonal array of pores, with a pore size of around 45 nm.
- Cribrum: Hexagonal packed pores roughly 200 nm in diameter.

- Foramen: Inner structure consisting of large holes with a diameter around 1150 nm.

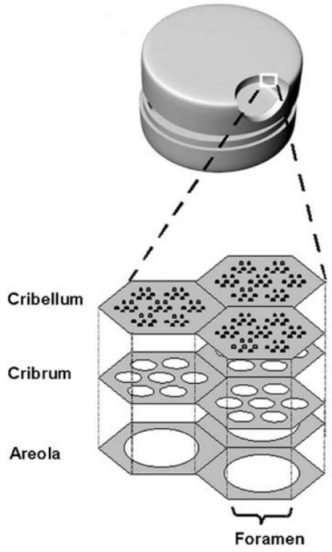

Figure 2.6: Schematic of Coscinodiscus frustule structure [101].

The frustule is formed by the mechanism of biomineralization. However, in contrast to mammals, which make biostructures such as bones of calcium carbonate, the frustules of coscinodiscus diatoms is formed by a composite of amorphous SiO_2 [102] and different organic components such as amino acids [103]. According to Schmid et al., the main building block of the SiO_2 structure is spherical SiO_2 units on the order of 12-30 nm, that aggregate together and form the larger frustule structure [104].

2.5.2 Diatoms as battery anodes

The combination of the macroporous structures of the different frustules layers, and the mesoporous structure of the spherical SiO_2 building blocks gives the frustules many of the desired properties described in the previous sections (section 2.4.4 and section 2.4.5). Additional benefits of the diatoms frustules are that they do not require advanced synthesis techniques/expensive precursors and that they are inherently environmentally friendly.

In 2016, Nysteen showed that carbon coated frustules from coscinodiscus diatoms cycled at 50 mAg^{-1} could achieved capacities over 600 $mAhg^{-1}$ after 100 cycles [16]. However, the reported capacities did not account for the capacity from carbon, making it difficult to estimate the capacity contribution from the SiO_2 frustules.

2.6 Characterization techniques

The goal of this section is to give a brief introduction to some of the experimental techniques used in this work and describe some of the limitations of teach technique in relation to the work in described in this report.

2.6.1 Electrochemical characterization techniques

2.6.1.1 Galvanostatic cycling

Galvanostatic cycling is a widely used electrochemical method for characterizing galvanic cells. Galvanostatic methods can easily be conducted under practical operation conditions and provides valuable insight to the capacity and reversibility of a cell[105].

In galvanostatic cycling, the working electrode is subjected to a constant current and the resulting potential is measured versus time. The current is applied until an upper voltage limit V_2 is reached, before the current is reversed and applied until a higher potential V_1 is reached.

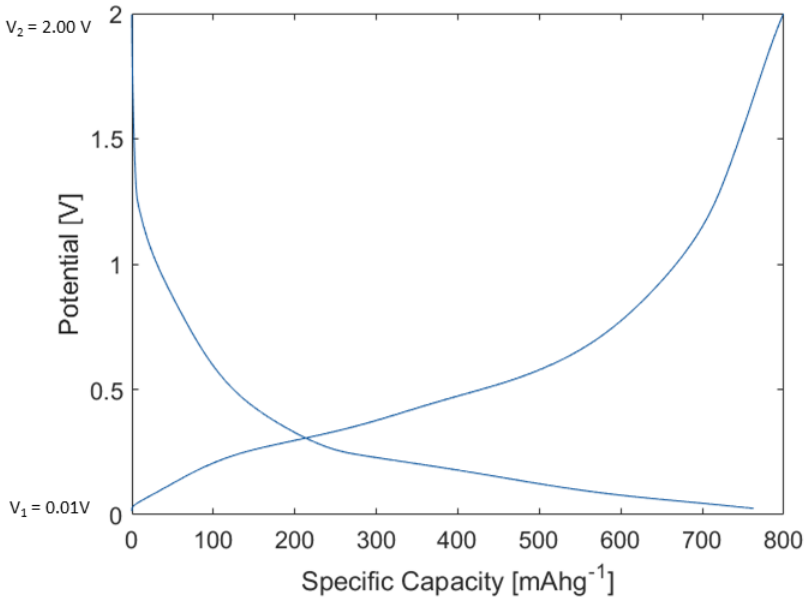

Figure 2.7: Schematic of galvanostatic cycling. Higher cut-off potential: 2 V. Lower cut-off potential 0.01 V.

A characteristic plot of the potential as a function of capacity can be seen in Figure 2.7. As the current is applied, the potential increase, before the potential stabilizes as an electrochemical reaction takes place. When all species around the electrode is consumed, the potential increases abruptly again. This increase will continue until a new electrochemical reaction takes place, the current is stopped or reversed. Then the cycle is repeated.

2.6.1.2 Differential capacity analysis

The first derivative of a galvanostatic curve dQ/dV, shown in Figure 2.8, can be used to gain insight into reactions occurring in a galvanic cell under galvanostatic cycling. The peaks in a differential capacity curves corresponds to the sharp increase in charge at voltage plateaus in galvanostatic curves, and the area under each peak corresponds to the charge related to the particular chemical reaction causing the plateaus [106]. Thus, the potentials at which peak are located can be used to determine the presence of a chemical reaction occurring at that potential. One of the main challenges of differential capacity analysis is that the presence of multiple reactions may result in convoluted peaks, where the peaks resulting from the individual reactions might be difficult to distinguish.

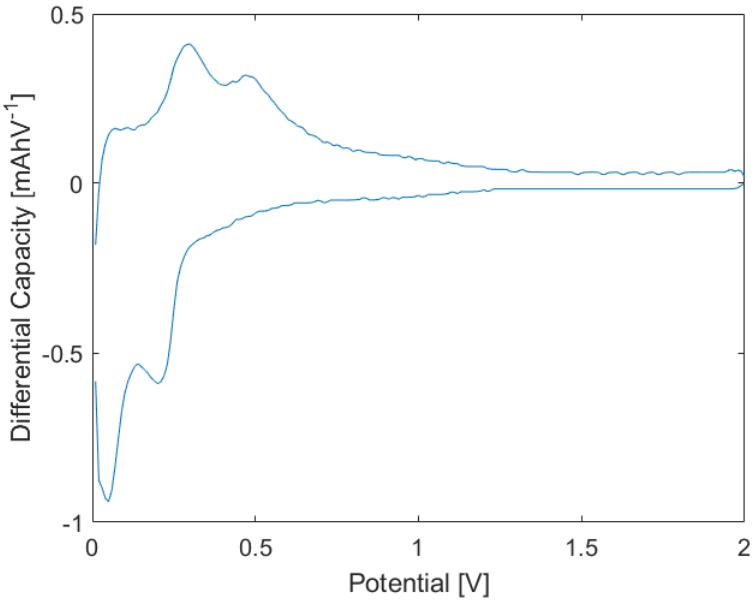

Figure 2.8: Differential capacity curve of Figure 2.7

2.6.1.3 Potentiostatic electrochemical impedance spectroscopy

Electrochemical impedance spectroscopy (EIS) is a great tool for studying the different reactions taking place in an electrochemical system. An electrochemical system subjected to a perturbation, leads to a change in the steady state of the system, and the rate at which the system proceeds to a new state is characterized by physical parameters such as reaction rate constants, diffusion constants, charge transfer constants and double layer capacity [107]. In potentiostatic EIS, electrochemical systems are subjected to a small potential perturbation at different frequencies ($\delta E(\omega)$) and the resulting current measured. The current signal is the sum of sinusoidal currents, where each current and its phase shift represents an electrochemical process. At high frequencies, the signal is dominated by high rate electrochemical processes, such as charge transfer, and at low frequencies the signal is limited by low rate processes such as diffusion [108]. The impedance of each process is then represented by the magnitude of the current and its phases shift.

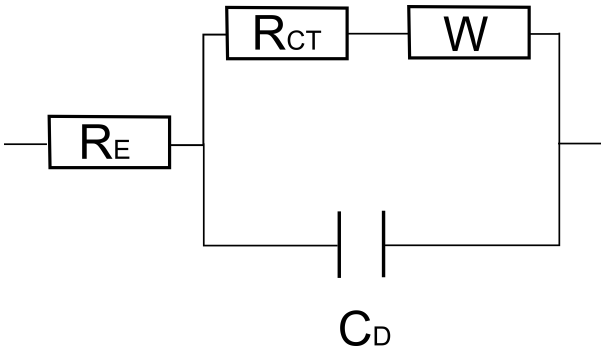

Figure 2.9: Schematic of equivalent circuit for battery (Randles circuit), showing the electrolyte resistance (R_e), charge transfer resistance (R_{ct}) and the double layer capacitance (C_D).

By comparing the measurement to equivalent circuits with ideal resistors and capacitors, the resistance and capacitance of a batter can be modelled. One of the simplest equivalent circuits used for modelling batteries is Randles circuit. However, in this case surface films are excluded. The Randles circuit is an ideal representation of the electrode/electrolyte interface, illustrated by the equivalent circuit in Figure 2.9a, where R_e represents the resistance of the electrolyte, C_{DL} the double layer capacitance on the electrode and the Warburg impedance W. The Warburg impedance corresponding to the semi-infinite diffusion of charged particles [109]. Nyquist plots are a simple way of illustrating EIS data. The Nyquist plot of a Randles circuit is presented in Figure 2.10, where the resistances are identified at the intercept between the plot and the real axis.

More complicated processes can be models by expanding the ideal circuit in Figure 2.9.

For example, the SEI layer on an electrode surface can be modelled with the addition of a resistor and capacitor in parallel.

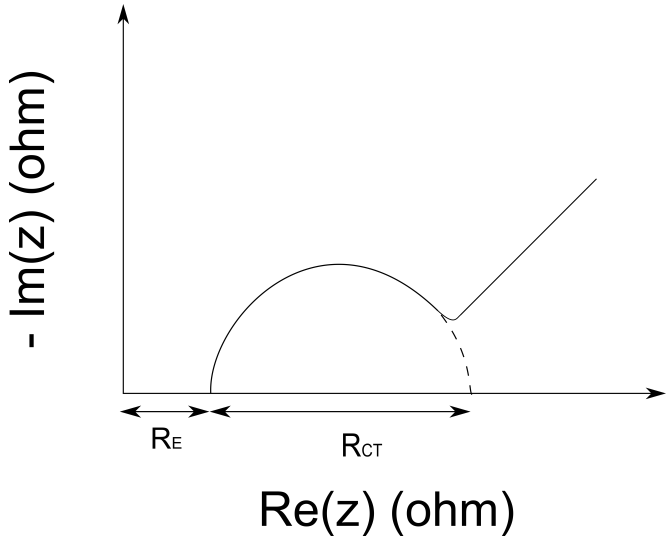

Figure 2.10: Schematic illustrating Nyquist plot of Randles circuit.

Double layer capacitance and surface area

The double layer capacitance (C_{dl}) can be obtained from a Nyquist plot by the following equation:

$$R_{\mathrm{CT}} \cdot C_{\mathrm{dl}} \cdot \omega_{\mathrm{max}} = 1 \tag{2.24}$$

were ω_{max} is the frequency on the at the highest point in the semicircle in Figure 2.10 [110]. As the double layer extend about 1-10 nm from the surface of the electrode, it follows the curvature of the surface with ease, and can therefore be assumed to be proportional to the surface area of the electrode [110]. Thus, impedance measurements can be used to estimate relative changes in the surface area of an electrode through cycling by equation:

$$A \propto C_{\mathrm{dl}} = \frac{1}{R_{\mathrm{CT}} \cdot \omega_{\mathrm{max}}} \tag{2.25}$$

2.6.2 Structural characterization techniques

2.6.2.1 Nitrogen adsorption and BET theory

Physisorption of an inert gas is a widely-used technique for investigating the surface area and the porosity of the a material. The basic principle of physisorption is to determine how many molecules of a certain gas, usually an inert gas such as N_2, adsorb on an surface. The total surface area is then calculated based on the area on N_2 molecule. However, this technique is complicated by the fact that most gasses form multilayers, not monolayers. With the use of Brunauer Emmett and Teller (BET) theory and t-plot theory this is accounted for, and physisorption can be utilized to estimate the surface area, the type of pores present in a material system and the pore distribution.

The derivation of the BET equation is beyond the scope of this project. However, if the absorbed amount of N_2 gas on a surface as a function of the pressure is known, the BET equation can be used to calculate the volume absorbed monolayers [111].

T-plot theory can be seen as an extension of BET theory and utilizes the absorbed volume as a function of the film thickness to determine the distribution of micropores ($<$ 2 nm) in a structure, relative to the amount of mesopores (2 nm - 50 nm) and macropores ($>$ 50) (the total volume of mesopores and macropores is often called external area). These measurements utilize the fact that there is an distinct difference in the absorbed volume as a function of thickens during filling of micropores and adsorption the outer surface of the pores, as illustrated in Figure 2.11 [112].

2.6.2.2 Scanning electron microscopy

The information in the section is based on the book, "Microstructural Characterization of Materials", by David Brandon and Wayne Kaplan [113].

Scanning electron Microscopy (SEM) is a great technique for investigating the surface morphology, material composition and structure of materials. An image is produced as an electron beam raster across the surface of a sample. In this process, three main signals are produced and processed. These are secondary electrons, backscattered electrons and excited x-rays.

Secondary electrons are emitted from the sample as incident electrons from the electron beam inelastically collide with the sample. Emission of secondary electrons is highly localized around the area of the incident electron beam, and decreases exponentially

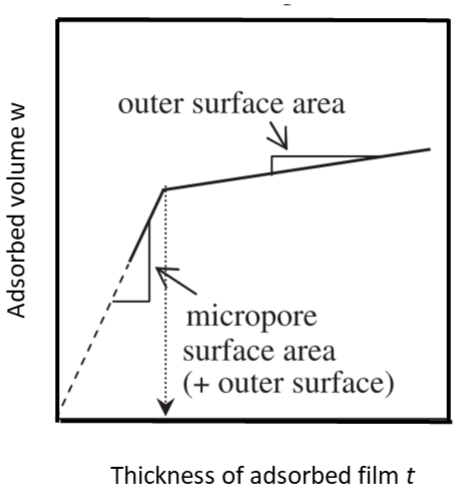

Figure 2.11: Illustration of underlying principle of t-plot theory, illustrating the difference in adsorption volume as a function of film thickness for micropores and outer surfaces. With alterations from [112].

with penetration depth. In addition, the probability of a secondary electron escaping the surface of the sample is highly dependent on the curvature of the sample and the angle of the incident electron probe. This makes secondary electrons ideal for characterizing surface morphology.

The fraction of the incident high electron energies which are scattered by angels more than π degrees are called backscattered electrons. The fraction of backscattered electrons is highly dependent on the atomic number of the specimens in the sample, increasing with increasing atomic number of the sample. Thus, backscattered electrons provide excellent contrast between phases in samples with different atomic numbers. The volume at which backscattered electrons are emitted from is much greater than that of secondary electrons, limiting the potential resolution.

2.6.2.3 Energy dispersive X-ray spectroscopy

As secondary electrons are produced, electrons in ionized atoms will transition from a higher orbitals to the vacant orbital caused by the secondary electron. These transi-

tions are accompanied by the emission of photons which lies in the x-ray region of the electromagnetic spectrum. The X-ray spectrum emitted constitutes a fingerprint of the chemical elements present in the sample. This spectrum can then be utilized to identify elements present in the sample and their spatial distribution and the technique is often referred to as energy dispersive X-ray spectroscopy (EDX).

2.6.2.4 Focused ion beam

Focused ion beam (FIB) systems is a powerful tool for direct nano-scale deposition and material removal. Today, most FIB system comes in dual-beam configurations, were a SEM and FIB can be operated in the same chamber, allowing for detailed characterization and manipulation of materials. In a FIB the ion beam is created by heating a reservoir of ions, usually gallium ions, to near evaporation temperature over a tungsten tips, and then accelerate the ions by an electric field, causing them evaporate and accelerate down the column [114].

The challenge of used a FIB to manipulate matter, is that the interactions with the ions beam and sample might significantly change the morphology of the material [115]. Thus, characterization of surfaces manipulated by an ion beams must be interpreted with great care.

2.7 Notes on full cells and half cells

Most research on battery materials is done in a half cell configuration, where Li-metal is used as a counter electrode. The benefits of using half cells is twofold. First, the use of the same counter electrode makes it simple to compare results in the literature. Second, the lithium metal provides a near limitless source of Li^+ to the system. However, the use of half cell have some other implications that should be noted.

Due to the low standard reduction potential of Li-metal, most anodes operate as a cathode in a half cell configuration. This is also the case for SiO_2 anodes. Nevertheless, throughout this work, materials that operate as an anode in a full cell configuration, will also be referred to as anodes in a half cell configuration. Moreover, this fact makes it necessary

to redefine some of the metrics defined in section 2.1.3 in the context of half cells.

$$\mathrm{CE} = 100 \cdot \frac{Q_{\mathrm{ch}}}{Q_{\mathrm{dis}}} \tag{2.26}$$

$$\mathrm{ICL} = Q_{\mathrm{dis}} - Q_{\mathrm{ch}} \tag{2.27}$$

$$\mathrm{CCL} = \sum_{k} Q_{\mathrm{dis}} - Q_{\mathrm{ch}} \tag{2.28}$$

The use of half cells also have some limitations that there are crucial to be aware of. First of all, the abundance of Li^+ in half cells is unrealistic in the context of full cells, as there is a limited availability of Li^+ in full cells. Thus, in a full cell, any consumption of Li^+ might lower the capacity of the cell, due to the reduces availability of Li^+. However, the challenge of Li^+ depletion could be hampered by pre-lithiation techniques such as electrochemical lithiation, chemical lithiation and the use of sacrificial electrodes [116].

The use of half cells also limits the study of compatibility between anode materials, cathode materials and electrolytes. This is exemplified by the electrolyte additive FEC, an electrolyte additive often used when studying Si anodes in half cell. However, in full cell test, some potential negative effect of FEC have been discovered [58]. Thus, it is not clear if FEC may be used in practice. This example serves to illustrate the importance of having an holistic approach when researching new battery materials.

Chapter 3: Experimental

3.1 Overview

This section gives a detailed description of the experimental procedures, equipment and experimental techniques used in this work. The experimental work consisted of four main steps. In the first step, the individual components of the electrode slurry were prepared. In the second step, the different components were mixed and the slurry was cast on to a current collectors. In the third step, electrolytes were prepared and coin cells, as well as three-electrode cells were assembled. The final step involved electrochemical and structural characterization of the electrodes before and after cycling. Due to the limited literature available on the use of SiO_2 from diatom frustules as an anode material and to ease the reproducibility, this experimental section has deliberately been written quite detailed.

The experimental work was divided into two phases. In phase 1, initial trails was conducted to explore the effect of variables such as carbon coatings, carbon additives, electrolyte additives and size reduction of the SiO_2 by milling. In addition, two capacity enhancing techniques were explored. The preparation of SiO_2/Si composite and electrochemical reduction of SiO_2. The capacity contribution from carbon coatings and carbon additives was also investigated.

In phase 2, electrochemical reduction was further investigated as a capacity enhancing technique. To ensure some degree of statistical significance, the galvanostatic cycling of all materials systems were conducted two times. To reduce uncertainty, both cells had the same loading of active material.

3.2 Preparation of the active material

The SiO_2 used in this project was derived from diatom frustules. The diatoms was supplied from Planktonic AS, delivered as a mixture of sea water, algae and other impurities. The SiO_2 was extracted from this mixture by a combination of washing and calcination. The role of the washing step was to remove any water soluble inorganic substances such as NaCl, and calcination was conducted to remove organic impurities.

The main processing steps used for purification (section 3.2.1) and carbon coating of the SiO_2 (section 3.2.3) is based on the experimental process done by Nysteen in 2016 [16].

3.2.1 Extraction of SiO_2 from diatom algae

The SiO_2 frustules were extracted from the diatom algae according to the following scheme [16]:

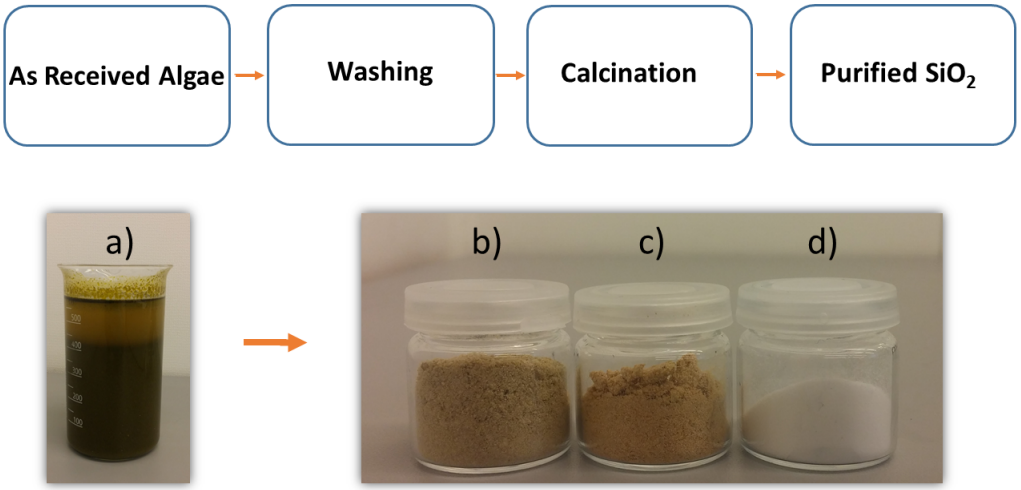

Figure 3.1: Schematic of the process adopted to extract the SiO_2 frustules from the algae. Images showing the algae; a) as received, b) dried, c) washed, d) calcined.

1. As received diatoms was left in a beaker for 1 h for the oil, water and diatoms to separate. Oil and water was poured off, and the algae separated from the remaining water with a 36 um mesh sieve. The diatoms were then dried for 24 h at 90 °C.
2. The dried diatoms were rinsed under running water and added to a beaker of deionized water (DI-water). The mass ratio of diatoms to water was 1:100.

3. The beaker was heated on a hotplate to 130 °C and stirred with a magnetic stirrer at 500 rpm for two hours.
4. A sieve with a 36 um mesh was used to separate the diatoms and the water, before fresh DI-water was added to the beaker. The mass ratio of diatoms to water was kept at 1:100.
5. The beaker was then sonicated for 30 min in an ultrasonic bath.
6. The diatoms were washed under flowing DI-water for five minutes. Finally, the diatoms were dried in a drying cabinet at 90 °C for 24 h, before the temperature was increased to 150 °C for 24 h. This approach was adopted to prevent the excess water from boiling.
7. The diatoms were calcined at 650 °C for 2 hours in flowing synthetic air atmosphere (80 Lh^{-1}) to remove any remaining organic compounds, forming pure nanostructured SiO_2.
8. XRD, Laser Diffraction and SEM were utilized to characterize the phase purity and morphology of the frustules SiO_2. The use of these characterization techniques are described in more detail in section 3.3.3 and section 3.8.

3.2.2 Milling

Planetary milling (PM100, Retsch) was conducted in a stainless-steel vile (50 ml) with one ball (4g, 10mm diameter) and a 5:1 ball to powder ratio. The SiO_2 powder was milled for 10 min at 600rpm. The process was repeated 4 times with a 5 min break between each interval to allow the system to cool down. To improve the homogeneity of the milling, the rotary direction was alternated between each run.

3.2.3 Carbon coating of SiO_2

The carbon coating on the SiO_2 was prepared as follows [16]. An overview of the exact amount of SiO_2, carbon precursor and solvent used can be found in the Appendix section A1.1.1.

1. 20 wt% SiO_2 and 80 wt% carbon precursor was wet mixed. Both corn starch (Corn Starch,1kg, Roth) and sucrose (Sucrose, 1 kg, Sigma Aldrich) was used as a precursor. The slurry was wet mixed in ethanol at 300 rpm, and evaporated at 40

°C for 1-2 h until the solvent had evaporated. In the case of sucrose, ethanol was replaced by DI-water and the slurry evaporated at 80 °C.

2. The dried slurry was transferred into an Al_2O_3 crucible and pyrolysed at 650 °C in a flowing argon atmosphere (80 Lh^{-1}). The pyrolysis time was 2 hours for the corn starch precursor and 6 hours for the sucrose precursor.

3.2.4 Preparation of the alginate binder

The alginate binder was prepared according to the following procedure and not kept for longer than 5 days.

1. Sodium alginate (Na-Alg, 100 g, Sigma Aldrich) and DI-water was mixed at a mass ratio of 1:60 in a beaker.
2. The beaker was place on a hot plate, the temperature set to 70 °C and stirred for 4 hours at 500 rpm with a magnetic stirrer.

3.3 Characterization of the active material

3.3.1 Laser diffraction

To evaluate the size of the diatoms, laser scattering (Partica Analyser La-960, Horiba) analysis was conducted. The measurement was conducted in wet mode, by using a suspension made of 0.03 g of SiO_2 in 4 g isopropanol (IPA). To prevent agglomeration, the suspension was sonicated for 30 min before the analysis was conducted. Following sonication, the suspension was added to the Particia by a pipette until the transmission dropped below 95 %. Before measurements were conducted, the de-bobbling function of the Particia were used. The measurements were repeated three times for statistical significance. Data processing was done with 1.450 and 1.378 as the real part of the refractive index of SiO_2 (Quarts) and IPA.

To confirm that most of the agglomerates were dissolved by the sonication step before the measurement, an additional 5 min of sonication was conducted in the Particia after the initial measurements. Following the extra sonication step, measurements were conducted once more to confirm that the additional sonication did not change the size distribution significantly.

3.3.2 Thermal gravimetric analysis

Thermogravimetric analysis (STA 449C Thermal analysis system, Netzch) was conducted to determine the gravimetric content of carbon in the active material. The active material was placed in an Al_2O_3 crucible until the crucible was half full. The following program was used:

- Temperature ramp from 26 °C to 100 °C at 10 °Cmin^{-1}.
- Hold at 1000 °C for 15 min.
- Temperature ramp from 1000 °C to 26 °C at 10 °Cmin^{-1}.

The hold step was to confirm that no mass loss was taking place at this point.

3.3.3 X-ray diffraction

X-ray powder diffractograms (XRD) (D8 Advanced DaVinci X-Ray Diffractometer, CuK_α radiation, Bruker) of the calcined SiO_2 diatoms were performed to identify any crystalline impurities in the samples. XRD samples were prepared by mixing 0.05 g SiO_2 and 1.5 IPA. The mix was then added to a silicon sample holder and the IPA evaporated.

The scan was conducted between 5 ° - 75 ° at 1.167 °min^{-1} and a fixed slit of 6 mm. The low scanning rate was chosen to increase the intensity from possible crystalline impurities at low concentrations.

3.3.4 Nitrogen adsorption measurements

The surface area of the active material was measured using nitrogen adsorption (Tristar 3000 Surface Area and Porosity Analyser), according to Brunauer-Emmett-Teller (BET) theory and t-plot theory. The measurements were carried out in liquid nitrogen (-195.85 °C). The samples were degassed under vacuum at 250 °C for a minimum of 12 h.

3.4 Slurries and electrode casting

Electrode slurries were prepared by mixing different compositions of an active material, alginate binder and a conductive additives (CB (C-Nergy C65, Timcal) or CNT (MWCNT, >95%, Sigma Aldrich). The slurry was mixed by ball milling (NM 400 mill, Retsch) at 25 Hz for 45 min.

After mixing, the slurry was cast onto a copper current collector (Plainstainproof, 10 um thick, Circuit Foil) using a tape caster (model K101, The K control coater), and a coating head calibrated to give a 40 um thick wet film. To remove excess water, the cast was left if a fume hood until the cast appeared dry, before it was placed in a vacuum oven (VD23, Binder) for overnight drying at 90 °C. Following drying, 16 mm diameter electrodes were punched from the cast, weighted and stored for future coin cell assembly. Electrode loadings can be found in the Appendix section A3.

Three types of casts were made; cast with SiO_2 as the main active material, SiO_2/Si (Silgrain e-Si 400, Elkem) composites and cast only containing carbon. An overview of the composition of all casts prepared is presented in Table 3.1. A detailed overview of the actual amount used of the different components in each cast, is given in the Appendix section A1.1.

The nomenclature of the casts are given according to the following algorithm. The letters before the hyphen describe the active material. P denotes pristine/uncoated SiO_2, C denotes SiO_2 carbon coated by a cornstarch precursor, S denotes SiO_2 carbon coated by a sucrose precursor and M denotes that the SiO_2 is milled. For the SiO_2/Si composites, the number behind Si denotes the wt % Si of the active material. For carbon casts, CD, SD and CB denotes, "cornstarch dummy", "sucrose dummy" and carbon black. The number and letter following the hyphen describe the carbon additive and the amount used. additives and the additive used. A further exploration on the naming convention used for electrodes and cast if presented in section 3.9.

Note on the used of binder

Alginate was used as the binder in all casts with the exception of CD and Si50M. Alginate was initially deemed insufficient as a binder for the carbon casts, thus PVDF was used for CD. However, later experimentation showed that alginate also could be used for the carbon cells. Alginate was therefore later used for the SD and CB cast. In the case of Si50M, CMC was used. This cast is describe in more detail in the Appendix section A7,

as it was prepared in collaboration with Kaland.

Table 3.1: Overview of casts prepared in this work, their composition and the name used to refer to the individual casts. Alginate was used as the binder in all cells with exception of CD and Si50M, where PVDF and CMC was used respectively.

Nomenclature	Active material [wt %]	Conductive additive [wt %]	Binder [wt %]
SiO_2 casts:			
P-25CB	60 % Pristin SiO_2	25 % CB	15 %
C-25CB	60 % Cornstarch coated SiO_2	25 % CB	15 %
S-25CB	60 % Sucrose coated SiO_2	25 % CB	15 %
P-35CB	50 % Pristine SiO_2	35 % CB	15%
P-35CBCNT	50 % Pristine SiO_2	17.5 % CB + 17.5 % CNT	15 %
PM-35CB	50 % Milled pristine SiO_2	35 %CB	15 %
SM-35CB	50 % Sucrose coated milled SiO_2	35 % CB	15 %
SiO_2/Si casts			
Si25	15 % Si + 45 % Cornstarch coated SiO_2	25 % CB	15 %
Si50	30 % Si + 30 % Cornstarch coated SiO_2	25 % CB	15 %
Si75	45 % Si + 15 % Cornstarch coated SiO_2	25 % CB	15 %
Si50M	25 % Si + 25 % Milled pristine SiO_2	17.5 % CB + 17.5 % CNT	15 %
Carbon casts:			
CD	60 % Pyrolysed Cornstarch	25 % CB	15 %
SD	60 % Pyrolysed Sucrose	25 % CB	15 %
CB	100 % CB	-	15 %

3.5 Electrolyte preparation

Two electrolytes were used in this project. A 1 M $LiPF_6$ in 50:50 vol% EC:DEC electrolyte (1 M $LiPF_6$ EC:DEC 50/50 vol%, 100 ml, Sigma Aldrich) and an electrolyte with FEC and VC as additives was prepared, with the volume ratio 94:5:1 vol %.

The electrolyte with FEC and VC was prepared by mixing the commercial electrolyte, FEC ($\geq$ 99.7 %, 25 g, Sigma Aldrich) and VC (Vinylene Carbonate, 2% bht, $\geq$ 97%, 5g , Sigma Aldrich) by the volume ratio, 94:5:1 vol%.

The electrolyte preparation was conducted in a glove box (Labmaster SP, MBraun) under argon atmosphere, with H_2O and O_2 levels below 0.1 ppm. The different components were mixed together in a polytetrafluoroethylene coated aluminium flask, and stirred overnight. An overview of the exact volumes used are presented in the Appendix section A1.2 . From this point out, EC will denote the commercial electrolyte, while FEC denote the electrolyte with FEC and VC as additives.

Table 3.2: Overview of electrolytes prepared.

Nomenclature	Ratio	Composition
EC	100 vol %	1 M $LiPF_6$ EC:DEC 50/50 vol%
FEC	94:5:1 vol%	$\sim$ 0.94 M $LiPF_6$ EC:DEC 50/50 vol%, FEC, VC [1]

3.6 Cell assembly

Two types of electrochemical cells were assembled, coin cells and three-electrode cells. All cells were assembled as half cell, with the electrodes from the casts described in section 3.4 as working electrodes (We) and lithium foils as the counter electrode (Ce).

3.6.1 Coin cells

Coin cell parts were supplied by Hohsen Corp (CR2016/SUS316L, 20.25 mm diameter and 1.6 mm high). The general schematic of the cell and the different components can be seen in Figure 3.2. A full overview of all cells assembled can be seen in the Appendix section A3.

The 16 mm diameter anodes were placed in the bottom of the coin cell, 20 uL electrolyte added on the top of the anode and a separator (Celgard 2400, 20 um thick, Celgard) placed on the top of the anode, followed by 20 uL more electrolyte added on the top of the separator. A 14 mm diameter Li metal counter electrode was punch out from a Li-foil (99.9 %, 0.75 mm thick, Alfa Aesar), brushed on both sides to remove any surface films and placed on top of the separator, followed by a stainless-steel spacer (CR 2016, 0.3 mm thick, Hohsen corp). Finally, the cell cap with a plastic gasket was placed on top and the cell hermetically sealed using a crimping machine (Automatic crimping machine, Hohsen Corp).

[1] Molarity calculated based on ideal mixing of solvents.

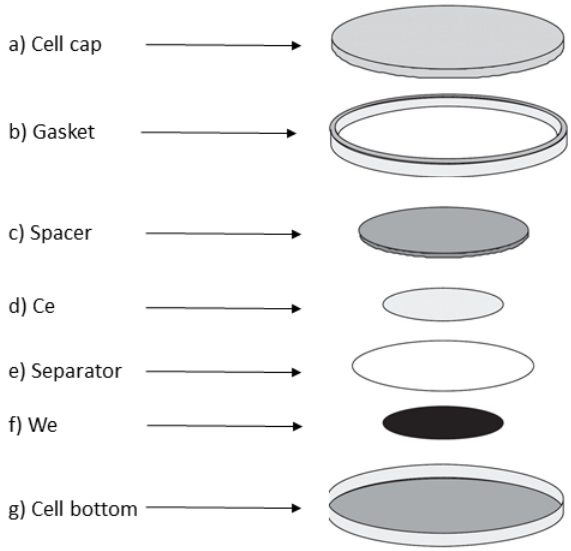

Figure 3.2: Schematic of coin cell and the order of the different cell components. With modifications from [117].

3.6.2 Three-electrode cells

For the three-electrode cell, ECC-REF (Figure 3.3) from EL-CELL, a 14 mm diameter Li metal counter electrode was punch from a Li-foil (99.9 %, 0.75 mm thick, Alfa Aesar), brushed on both sides to remove any surface films and placed in the cell base. Following the Li counter electrode, a thin piece of Li metal was rolled together and placed in the feed through hole of the sleeve, before the reference electrode pin was screwed in placed. A glass fiber separator (1.55 mm thick, EL-Cell) was place on top of the counter electrode, before 500 uL electrolyte was added. The WE electrode was then placed on top of the separator. Finally, the piston and compressive spring was placed on top of the electrode, before the lid was put in place and the cell placed in the bracket and tighten.

3.7 Electrochemical characterization

Before characterization, all cells were rested for 12 h to allow the electrolyte to penetrate the electrode. Moreover, the health of all cells was probed with EIS. Any cell with a high frequency resistance over 5 ohm was discarded.

The coin cells were cycled galvanostaically using two galvanostats: 1) LANHE CT2001A and 2) BioLogic BCS 805. The three-electrode cells were cycled on a BioLogic VMP3.

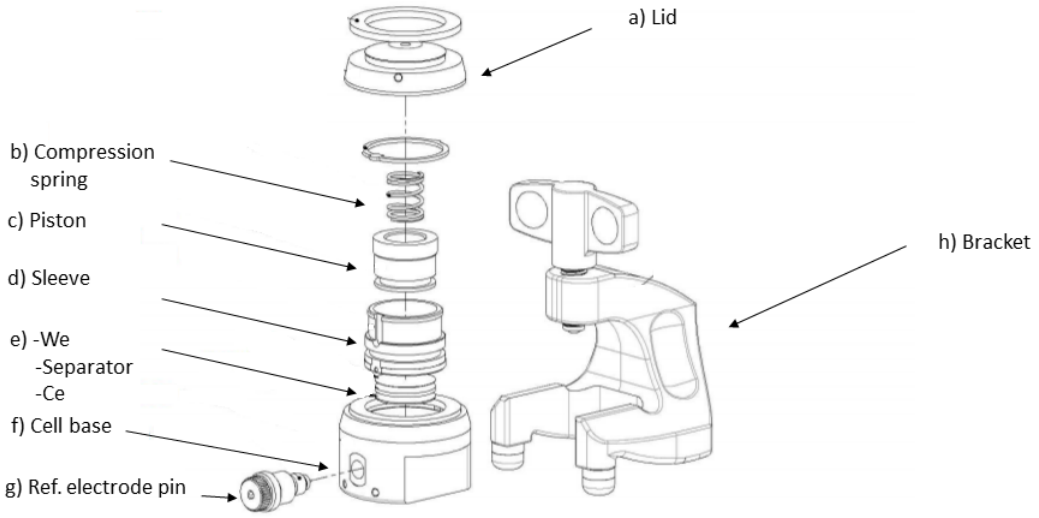

Figure 3.3: Schematic of three-electrode cell and the different components. With modifications from [118].

After the cycling, a selection of the coin cells was disassembled and the working electrodes collected for post-mortem SEM characterization.

In phase 1, only one cell from each material system with SiO_2 was cycled. In the case of the carbon cells, three cells were cycle for statistical significance. In phase 2, three cells of the reference were cycled. However, due to limitations on the equipment capable of conducting the electrochemical reduction step, only two cells were cycled with this program.

3.7.1 Galvanostatic cycling

To investigate the electrochemical behaviour of the cells, five different programs were used. Three programs involved galvanostatic cycling between two limiting potentials at a constant current. In addition, an electrochemical reduction program was used, which included a potentiostatic hold step at 0.002 V for a given time, followed by galvanostatic cycling. Finally, a rate capability program was used to probe the rate performance of the cells at higher currents. A formation cycle at 50 mAg^{-1} was used in all programs, with the exception of Si50M, were a formation cycle of 200 mAg^{-1} was used.

The electrochemical reduction program involved a hold step at 0.002 V in the second cycle. Three different time intervals were used in the hold step; 12 h, 48 h, and 132 h.

The rate capability tests were only conducted on cells from phase 2, which had been

subjected to a 48 h electrochemical reduction step and completed 50 cycles. This, to allow for conversion of SiO_2 to Si before testing.

Differential capacity analysis was conducted on the data retrieved from the BioLogic BCS galvanostat and calculated with the BT lab software supplied by Biologic. The calculation was done with a resolution (ΔE) of 10 mV.

An overview of all programs are presented in Table 3.3. The following nomenclature will be used in the report; L denotes regular galvanostatic cycling between 0.01 V - 2.00 V. L3 denote galvanostatic cycling between 0.01 - 2.00 V. L1 denotes galvanostatic cycling between 0.05 V - 1.00 V. Hx (for x = 12, 48, 132) denotes the electrochemical reduction program. Where x represents the time the electrode was held at 0.002 V.

Table 3.3: Overview of cycling programs used in this project. GS and PS denotes galvanostatic and potentiostatic respectively.

Nomenclature	Current density [mAg^{-1}]	Potential window [V] vs Li/Li^+	GS/PS	Comment
Formation cycle 1	50	0.01 - 2.00	GS	-
Formation cycle 2	200	0.05 - 1.00	GS	-
Long-1V (L1)	500	0.05 - 1.00	GS	-
Long-2V (L)	200	0.01 - 2.00	GS	-
Long-3V (L3)	200	0.00 - 3.00	GS	-
Hold (Hx)	a) 50	2.00 - 0.002	GS	-
	b) $*$	0.002	PS	12 h, 48 h and 132 h tested.
	c) 50	0.002 - 2.00	GS	-
	d) 200	2.00 - 0.01, 0.01 - 2.00	GC	Step d) repeated.
Rate	100, 200, 300, 500, 1000, 2000	0.01 - 2	GC	Conducted after 50 cycles.

3.7.2 Electrochemical impedance spectroscopy

EIS was conducted on a BioLogic VMP3 multichannel potentiostat. Two different programs were applied:

- EIS 1: Frequency range: 500 000 000 Hz - 1 Hz. Amplitude: 10.0 mV.
- EIS 2: Frequency range: 500 000 000 Hz - 0.01 Hz. Amplitude: 10.0 mV.

EIS 1 was mainly used to verify the health of individual cells before cycling.

In order to explore the effect of SiO_2 conversion to Si on the impedance of the electrode, EIS was carried out in combination with a electrochemical reduction program. EIS was conducted before cycling (EIS 1), after the formation cycle (EIS 2), after the electrochemical reduction step (EIS 2) and after 10 cycles (EIS 2), in both lithiated and delithiated state.

3.8 Structural characterization

Post mortem characterization was conducted on selected electrodes. The electrodes were collected by disassembling coin cells in a glove box, and rinsed in DMC before they were dried. Afterwards they were stored in a clean room (ISO7, NTNU Nanolab), to limit contamination.

Scanning electron microscopy

Two SEMs were used for structural characterization. An in-lens S(T)EM (S-5500, Hitachi) was used to obtain high resolution micrographs of the SiO_2 frustules. As this is an in-lens system, no specific working distance is given. The acceleration voltage was 2 kV.

In addition, a field emission SEM (Apreon, FEI) was used to obtain micrographs of the electrodes before and after cycling. The micrographs were captured at a working distance of 2 mm. The acceleration voltage was 2-5 kV. A range of potentials had to be used as the electrodes had different conductivity after cycling. The EDX (Xmaz 80 mm2, Oxford Instruments) analysis was conducted on the Apreon SEM at a 10 mm working distance, and a 5 kV acceleration voltage.

FIB cross-section analysis

FIB cross-section analysis was conducted with a dual beam FIB (Helios NanoLab Dual-Beam FIB, FEI). The FIB was used to make cross section samples of the electrodes.

The cross section was obtained with a gallium ion beam. First, a square was cut with a high beam current at 9.3 nA. Finally, a low current, 0.46 nA was used to "polish" the surface of the cross section. This was done in an attempt to limit the effect of the ion beam on the morphology of the material.

3.9 Report terminology and conventions

- **Reference for potentials:**
  All potentials are hereafter given vs Li/Li^+ unless otherwise stated.
- **Use of the word active material:**
  Active material will in this work describe all material in the electrode which is not the binder or conductive additives, i.e. in cells with SiO_2, the active material is defined as the the amount of SiO_2 or the amount of the carbon coated SiO_2. In carbon cells, the active material is defined as the total amount carbon tested for. Therefore, in cells with pyrolyzed carbon, the CB is not counted as an active material.
- **Use of the word capacity:**
  The word capacity will unless otherwise stated refer to the specific charge capacity of a cell (the capacity during delithiation). The specific charge capacity reported is normalized to the active material in the cell. Thus, the weight of the binder and the conductive additives is not accounted for.
- **Use of the word frustules and SiO_2:**
  The word frustules will be used to describe the SiO_2 frustules before it is added to an electrode cast. At this point, the SiO_2 frustules will simply be referred to as SiO_2.

- **Naming convention for casts and cells:**
  The naming convention for casts and cells used in this work is illustrated in Figure 3.4. The two first section combined describe a given cast (active material + conductive additive). The three first sections combined describe a cell (active material + conductive additive + electrolyte). The four sections combined describe a cell and the experimental program the cell has been subjected to.

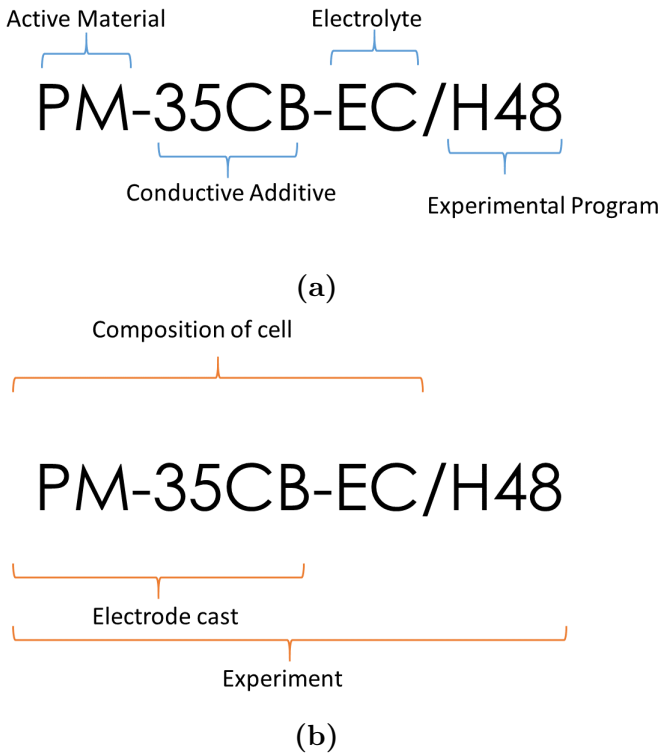

Figure 3.4: Illustration of naming convention for electrodes and cells used in this work.

Chapter 4: Results

4.1 Overview

The results in this chapter are divided into three main parts. First, the results from the characterization of the purified diatoms and the active material are presented. The goal of this part is to provide insight into the nature of the extracted SiO_2 frustules. This section include SEM micrographs and XRD analysis of the processed diatoms, and laser diffraction, BET and TGA analysis of the active material used. This part is followed by electrochemical characterization of the SiO_2 anodes by galvanostatic cycling and EIS, aiming to determine the electrochemical performance of the SiO_2 anodes. Finally, post mortem analysis is conducted by SEM, FIB-cross section and EDX. This is done in an effort to better understand the electrochemical results

4.2 Characterization of extracted SiO_2 and active material

4.2.1 Crystallinity

XRD diffractograms of the extracted SiO_2 and the carbon coated SiO_2 in Figure 4.1 indicates that no crystalline phases are present in the sample. The broad peak centered at 22 ° is associated with amorphous SiO_2 [88, 119]. Thus, both the extracted SiO_2 and the carbon coating appears to be amorphous. XRD diffractograms of all batches prepared in this work can be found in the Appendix A2.1.

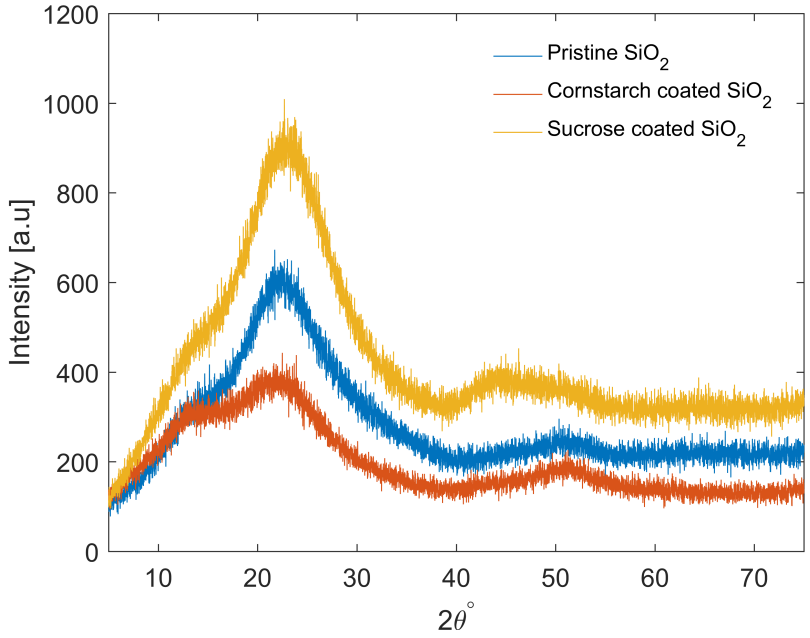

Figure 4.1: XRD diffractogram of pristine SiO_2 and carbon coated SiO_2 extracted from diatom frustules.

4.2.2 Microstructure and morphology

The microstructure and morphology of the extracted diatoms can be seen in Figure 4.2a, 4.2b. A close-up view of the surface in Figure 4.2b, can be seen in Figure 4.2c. Figure 4.2d show a high resolution micrograph of the porous surface of a frustule layer. A comparison with the AFM study by Losic et al, indicates that a large fraction of the structures are of the species coscinodiscus [101].

The main structures of the frustules appear to be in the range of 50 nm - 3 um, which is in agreement with the literature [101]. In Figure 4.2d, even smaller structures at the sub 50 nm level can be seen. These structures may be the fundamental building blocks of silica described by Schmid et al [104]. Even though the microstructures of the diatom frustules are quite small, the whole frustules (i.e. whole pieces of frustule) can be seen to be at the order of tens of microns. Additional micrographs of the different frustules layers and their features are presented in the Appendix section A5.

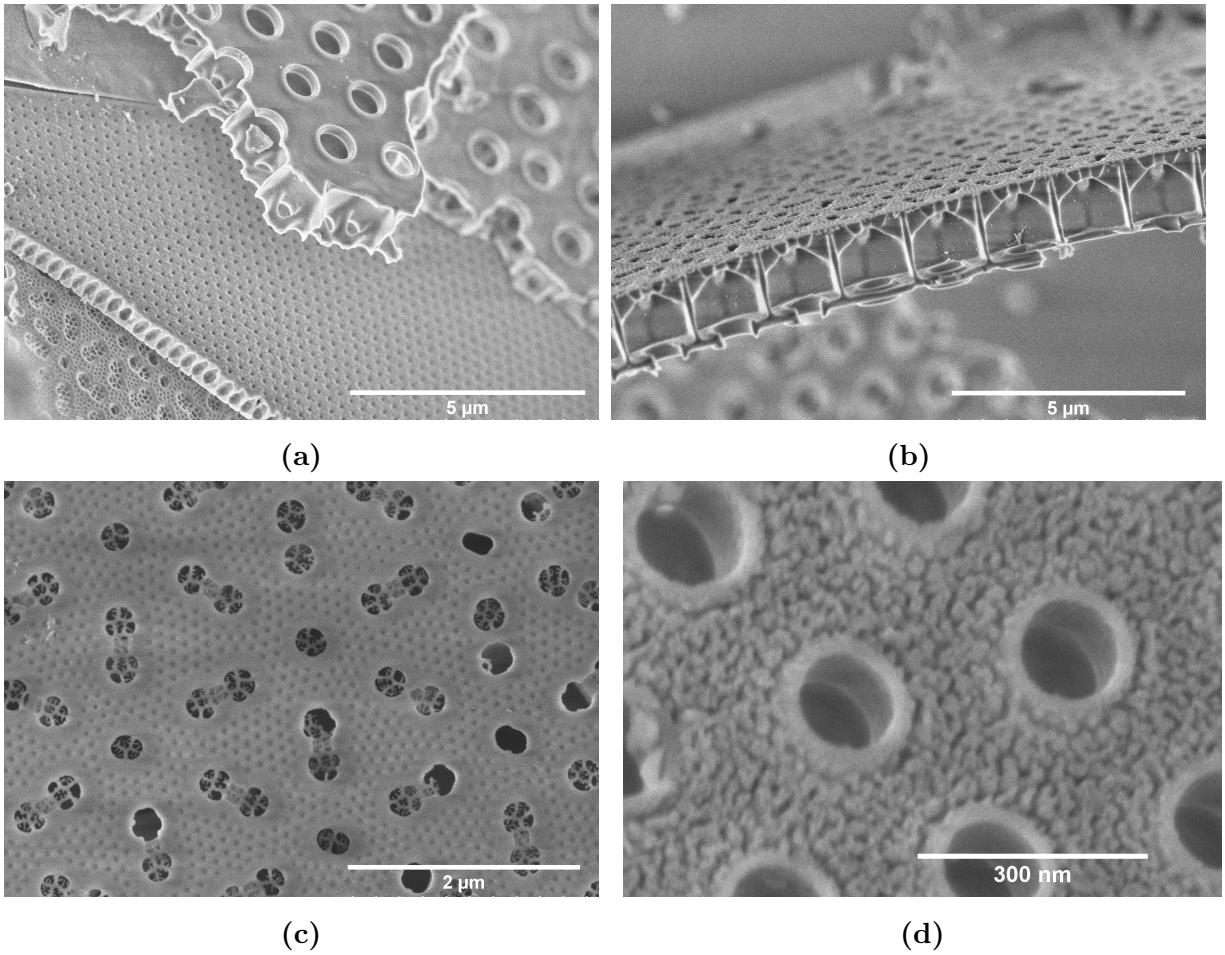

Figure 4.2: SEM micrographs of the diatom frustules. (a) Overview of multiple frustule layers, (b) cross section of frustule, (c) surface of frustule in (b), (d) high resolution micrograph of frustule surface.

4.2.3 Particel size distribution

The particle size distributions of the milled and unmilled SiO_2 determined by laser diffraction can be seen in Figure 4.3. The mean and the median size, calculated on a numbers basis, are presented in Table 4.1. These calculations were conducted on the basis of three subsequent measurements for statistical significance. The results from all measurements are found in the Appendix section A2.2.

The size distribution (Figure 4.3) demonstrates a significant size reduction by milling. The median of the SiO_2 was reduced from 40.00 $\pm$ 2.016 um to 3.086 $\pm$ 0.1783 um. The milling also result in a bimodal size distribution, with the peak intensity of the two size distributions at 0.445 um and 5.87 um.

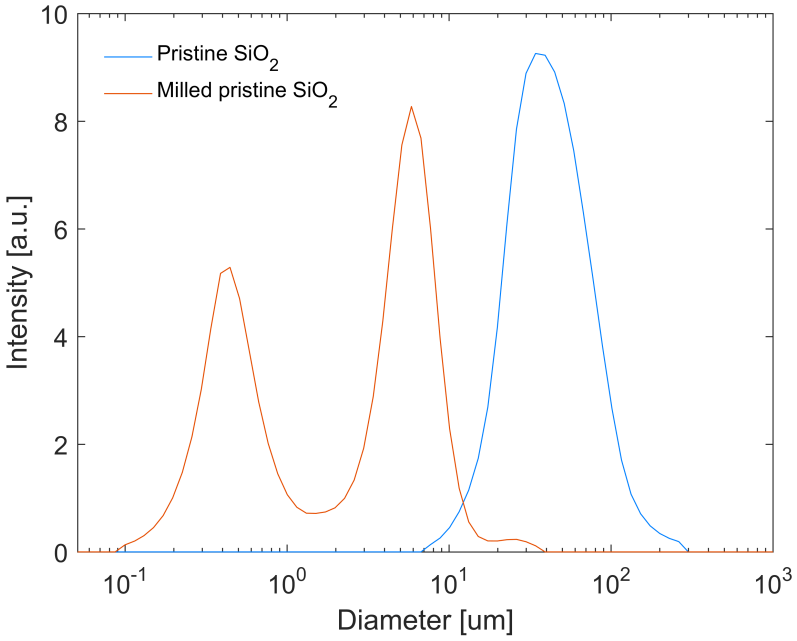

Figure 4.3: Size distribution of milled and unmilled SiO_2 by laser diffraction.

Table 4.1: Overview of the mean, median and the standard deviation of the laser diffraction measurements.

Material	Median [um]	Mean [um]	Std [um]
SiO_2	40.00 ± 2.015	51.29 ± 4.9854	38.2300 ± 7.307
Milled SiO_2	3.086 ± 0.1783	3.379 ± 0.1687	3.402 ± 0.2432

Based on the observation made by SEM (Figure 4.2) and laser diffraction (Table 4.1), the features on the frustules may be divided into three different size ranges.

- Macro structure: The size of a frustule particle.
- Microstructure: The size of the main features on a frustule particle.
- Nanostructure: The size of smaller building blocks that make up the frustules.

The laser diffraction indicate that the macrostructure of the frustules has a median size of 40.00 ± 38.23 um before milling, reduced to 3.086 ± 0.1783 by milling. The SEM micrographs (Figure 4.2) show the microstructures of frustules to be in the range of 50 nm - 3 um, and the nanostructures (Figure 4.2) on is on the order of <50 nm.

4.2.4 Surface area and porosity

Based on the nitrogen adsorption data, the BET surface area and the t-plot areas (micropore area and external area) were calculated. The data is presented in Figure 4.4 and Table 4.2. The BET surface area of the SiO_2 was 8.19 m^2g^{-1}, where 4.47 m^2g^{-1} resulted from micropores and 3.48 m^2g^{-1} from external area (mesopores and macropores). Milling of the SiO_2 increased the BET surface are to 17.2 m^2g^{-1} and this increase was almost exclusively in external area.

The carbon coated SiO_2 shows a significant increase in BET surface area, ranging from 168 m^2g^{-1} to 289 m^2g^{-1} for cornstarch and sucrose precursors respectively. Furthermore, the increase in surface area results from an increase in both micropores and external area (Figure 4.4).

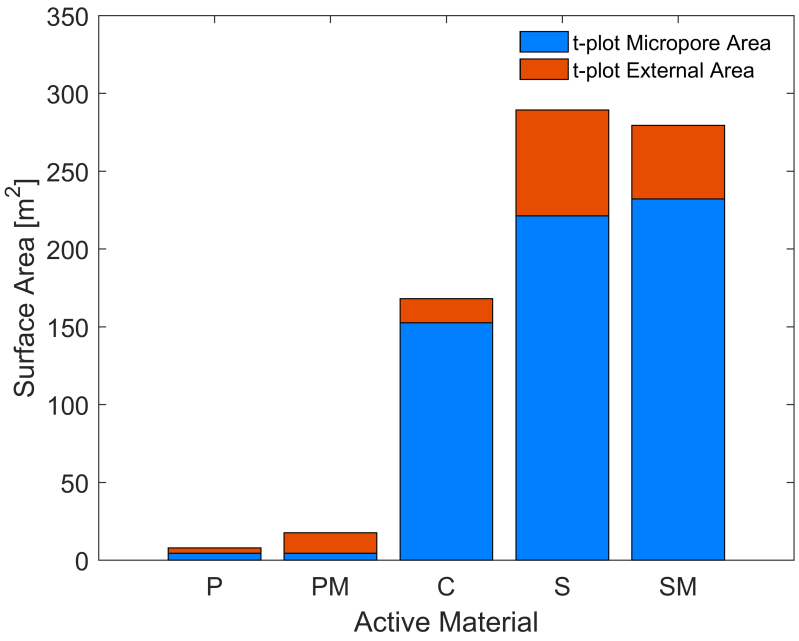

Figure 4.4: Blue bar indicates the surface area of micropores. Red bar indicates the surface area of external area (mesopores and macropores). Sum of the blue and the red bar equals the BET surface area.

Table 4.2: BET surface area and t-plot micropore/external of SiO_2 calculated from nitrogen adsorption data.

Material	BET surface area [m^2g^{-1}]	t-plot micropore area [m^2g^{-1}]	t-plot external area [m^2g^{-1}]
P SiO_2	8.19	4.47	3.47
PM SiO_2	17.2	4.46	13.2
C SiO_2	168	153	15.4
S SiO_2	289	221	67.9
SM SiO_2	279	232	47.2

4.2.5 Thermogravimetric analysis

Thermogravimetric curves of the carbon coated diatoms are presented in Figure 4.5. The cornstarch coated SiO_2 experience a sharp mass loss at 510 °C, that continues until 584 °C, after which the mass loss is negligible. The sucrose coated SiO_2 experience a more gradual mass loss from 580 °C to 1000 °C. The carbon content of the different active materials was calculated by evaluating the mass loss upon heating, and is presented in Table 4.3.

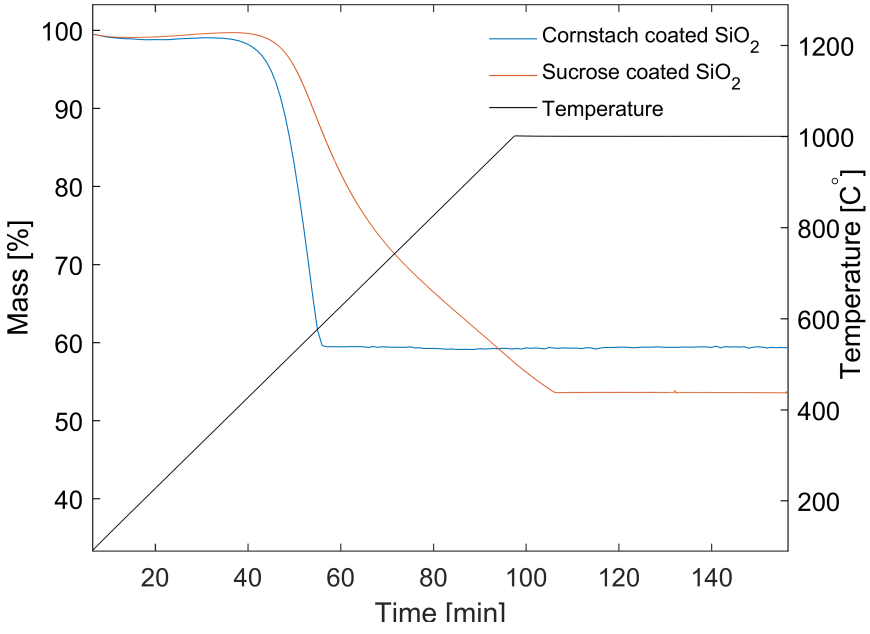

Figure 4.5: Thermogravimetric curves of carbon coated SiO_2, with both cornstarch and sucrose as carbon precursors. Sample heated from 25 °C to 1000 °C at 10 °Cmin^{-1} .

Table 4.3: Calculated carbon content of the silica with different carbon coatings. Calculation based on thermogravimetric curves.

Material	Carbon content [wt%]
Cornstarch coated SiO_2	40.6
Sucrose coated SiO_2	46.5

4.3 Electrochemical characterization

4.3.1 Carbon cells

The average capacity of the carbon cells is presented in Figure 4.6, with the error bar indicating 1 standard deviation. Over the first cycles the capacity dropped in all cells before stabilizing around cycle 20. At cycle 20, the capacity is 560 mAhg $\pm$ 92.0 $mAhg^{-1}$, 286 $\pm$ 36.3 $mAhg^{-1}$ and 274 $mAhg^{-1}$ $\pm$ 1.98 $mAhg^{-1}$ for pyrolyzed sucrose, pyrolyzed cornstarch and CB respectively. Both pyrolyzed sucrose and pyrolyzed cornstarch show large variations in the dataset, indicated by the large standard deviation. Table 4.4 presents coulombic efficiency of the carbon cells.

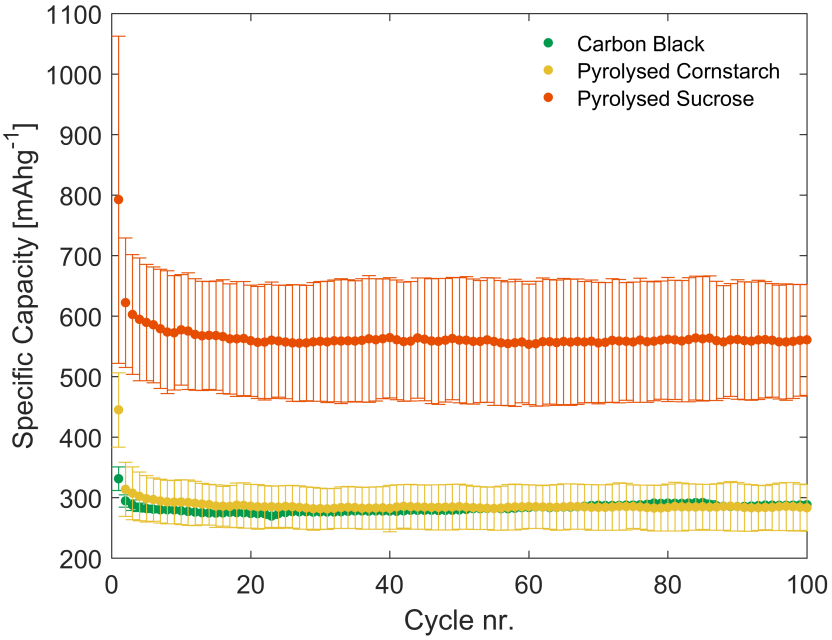

Figure 4.6: Specific charge capacity of all carbon cells. Error bar indicates one standard deviation. All cells cycled between 0.01 V - 2.00 V vs Li/Li^+. First cycle at 50 $mAhg^{-1}$ and subsequent cycles at 200 $mAhg^{-1}$.

Table 4.4: Average coulombic efficiency of carbon cells, ± 1 standard deviation.

Cycle	CB	CD	SD
	Coulombic Efficiency [%]	Coulombic Efficiency [%]	Coulombic Efficiency [%]
1	58.47 ±16.29	61.13 ± 14.8525	56.59 ± 8.552
2	91.58 ±0.7686	92.00 ± 6.928	86.66 ± 0.6104
3	94.33 ±0.3102	97.81 ± 2.926	96.89 ± 0.2950
10	96.93 ±0.1150	99.79 ± 1.911	99.32 ± 0.8430
20	97.93 ±0.0473	99.79 ± 1.911	99.32 ± 0.8430
50	98.88 ±0.0351	99.74 ± 0.9623	99.05 ± 0.2138
100	99.14 ±0.1343	99.97 ± 0.3660	99.73 ± 0.0872

Estimated capacity contribution from carbon

In Table 4.5, the estimated capacity contribution from carbon for a selection of cells is presented. The estimates were made based on the wt % of pyrolysed sucrose, pyrolysed

cornstarch and CB in each cell and the average capacity of the respective carbons at cycle 20.

Table 4.5: Estimated capacity contribution of carbon in different electrodes. Horizontally the carbon contribution from different carbons at a certain wt % is given. The total capacity contribution from carbon in each electrode is given in the last column to the right.

Cast	25 wt% CB [$mAhg^{-1}$]	35 wt% CB [$mAhg^{-1}$]	50 wt% C [$mAhg^{-1}$]	50 wt% S [$mAhg^{-1}$]	60 wt% S [$mAhg^{-1}$]	Total [$mAhg^{-1}$]
Carbon	68.5	95.9	58	130	-	-
P-25CB	68.5	-	-	-	-	68.5
PM-35CB	-	95.0	-	-	-	95.0
C-35CB	-	95.9	58.1	-	-	154
S-25CB	68.5	-	-	-	156	225
SM-35CB	-	95.9	-	130	-	226

4.3.2 Phase 1: Initial screening of SiO_2 derived from diatom frustules

4.3.2.1 Capacity curves

Two general observation can be made of all cells with SiO_2. First, cells with SiO_2 exhibited a high first cycle capacity and a subsequent decrease in the charge capacity at the second cycle. Second, the capacity is found to increase with cycle number in most cells. Based on these observations, the capacity of the 2nd cycle will be used as the initial capacity of the cells. Moreover, the capacity increase of a cell is given by the difference in capacity between cycle 100 and cycle 2.

Figure 4.7a presents all cells with pristine SiO_2 as the active material. The initial capacity is observed to be between 140 $mAhg^{-1}$ and 165 $mAhg^{-1}$. The largest capacity observed after 100 cycles is in PM-35CB-EC/L, and the lowest in P-35CBCNT-EC/L, at 186 $mAhg^{-1}$ and 161 $mAhg^{-1}$ respectively.

Cells with carbon coated SiO_2 as the active material exhibit higher capacity than cells with pristine SiO_2. Figure 4.7b, show that the initial capacity is in the range of 181 $mAhg^{-1}$ to 328 $mAhg^{-1}$, and between 185 $mAhg^{-1}$ and 409 $mAhg^{-1}$ after 100 cycles. The highest initial and final capacity was observed for SM-35CB-EC/L. Limited increase

in capacity was experience in cell with unmilled SiO_2. However, the cell with milled SiO_2, SM-35CB-EC/L, experience an increase of 80 $mAhg^{-1}$ over the first 100 cycles.

The two electrolytes were tested on four different electrodes, two with pristine SiO_2 (P-35CB and PM-35CB) and two with carbon coated SiO_2 (S-25CB, SM-35CB). In Figure 4.7c, the capacity of cells with PM-35CB and SM-35CB electrodes cycled in the two electrolytes are presented. PM-35CB experience an increase in initial capacity from 162 $mAhg^{-1}$ to 181 $mAhg^{-1}$ with the FEC electrolyte (PM-35CB-FEC/L) compared to EC (PM-35CB-EC/L). Moreover, a larger increase in capacity with cycle number can also be observed in PM-35CB-FEC/L, relative to PM-35CB-EC/L. In the case of SM-25CB, the opposite trend is observed, with an initial capacity of the cell with FEC (SM-35CB-FEC/L) and EC (SM-35CB-EC/L) at 241 $mAhg^{-1}$ and 328 $mAhg^{-1}$ respectively. The capacity of the cell with the EC electrolyte (SM-35CB-EC/L) also increase more with cycle number. Cells with unmilled SiO_2, P-35CB and S-25CB, are presented in the Appendix Figure A6a, showed no significant difference in capacity when cycled in the two different electrolytes.

The capacity of cells with the same compositions, but with milled and unmilled SiO_2 are presented in Figure 4.7d. Both cells with pristine SiO_2 and carbon coated SiO_2 experience an increase in initial and final capacity with milled SiO_2. The greatest increase was observed in the carbon coated and milled SiO_2, with an initial and final capacity of 328 $mAhg^{-1}$ and 409 $mAhg^{-1}$ for SM-35CB-EC/L , compared to 181 $mAhg^{-1}$ and 188 $mAhg^{-1}$ for S-25CB-EC/L. The increase in capacity by milling observed for pristine SiO_2 can be seen in the Appendix Figure A6b.

The capacity of cells with different composition of conductive additives is given in Figure 4.7e. The initial capacity is in the range of 145 $mAhg^{-1}$ - 155 $mAhg^{-1}$ for all cells. The highest capacity after 100 cycles, 171 $mAhg^{-1}$, was achieved by the cell with the lowest amount of CB, P-25CB-EC/L. The lowest capacity was observed in the cell with CNT, at 161 $mAhg^{-1}$ after 100 cycles.

In Figure 4.7f, a significant increase in both initial and final capacity can be observed by increasing the cycling window from 0.01 V - 2.00 V to 0.00 V - 3.00 V. After 100 cycles, the capacity of P-35CB-EC/L3 was 51 $mAhg^{-1}$ higher than P-35CB-EC/L.

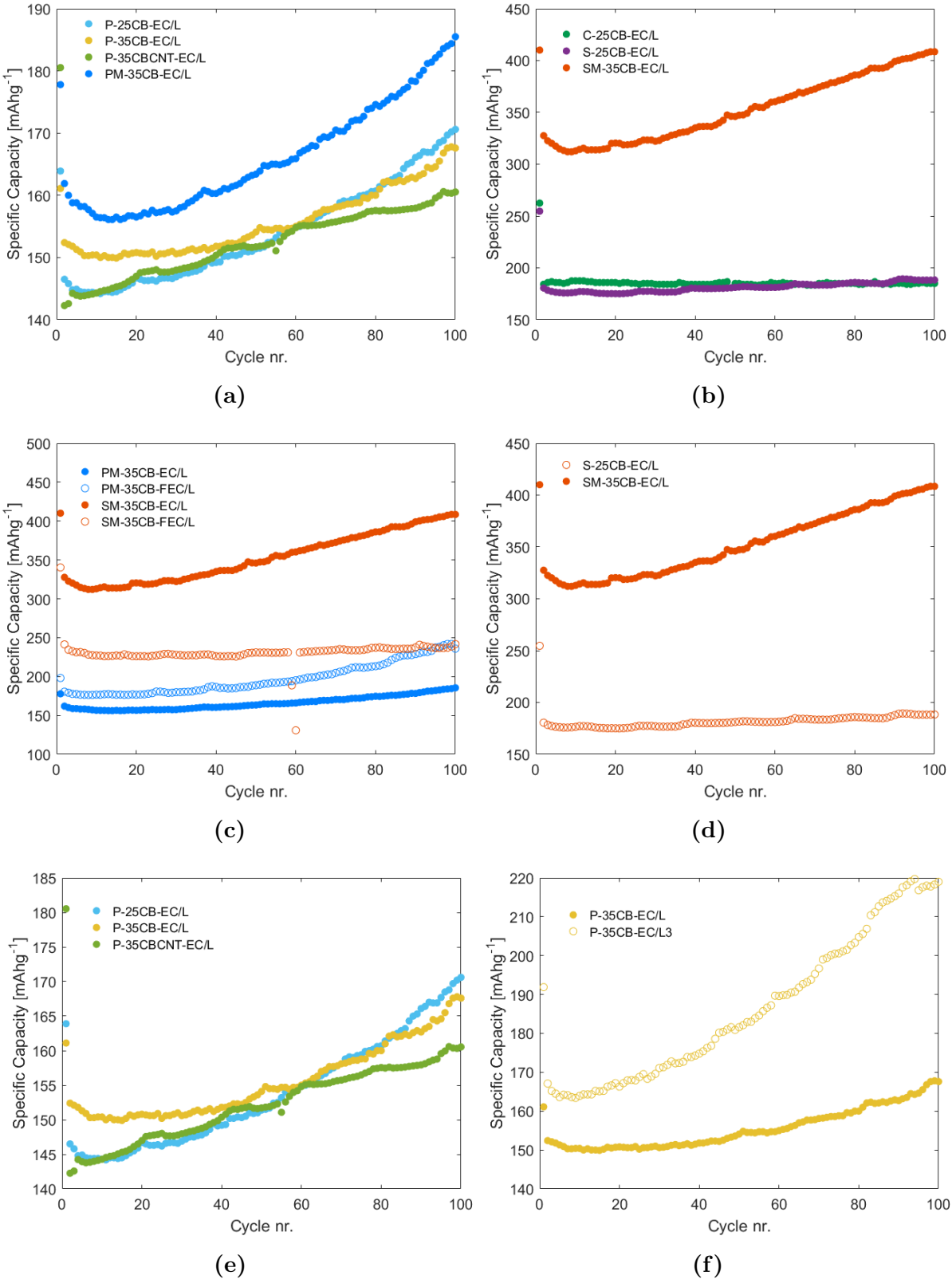

Figure 4.7: Specific charge capacity of SiO_2 cells cycled in phase 1. (a) Cells with pristine SiO_2, (b) cells with carbon coated SiO_2, (c) cells with same electrode composition, but different electrolytes, (d) cells with milled and unmilled SiO_2, (e) cells with different composition of conductive additives and (f) cells cycled with different voltage windows. Details on the cycling programs can be found in Table 3.3.

4.3.2.2 Si and SiO_2/Si composites

The capacity of cells with Si and SiO_2/Si composites as the active material can be seen in Figure 4.8. The initial capacity of the composite cells; Si25, Si50, Si75, is significantly higher than the initial capacity of the SiO_2 anodes, with 792 $mAhg^{-1}$ as the lowest first cycle capacity (Si25). Moreover, the initial capacity is found to increase with Si content. However, the cycling stability of the composite cells is poor and the capacity is rapidly reduced with cycle number. At cycle 100, the capacity is equal to that of cells with SiO_2 as the only active material.

The improved composite cell, Si50M-Improved (milled SiO_2 and Si, optimized binder and reduced cycling window), initially demonstrated better cycling stability compared to Si and SiO_2/Si composites. Nevertheless, the capacity is reduced with cycling and after 100 cycles the capacity is reduced to 209 $mAhg^{-1}$.

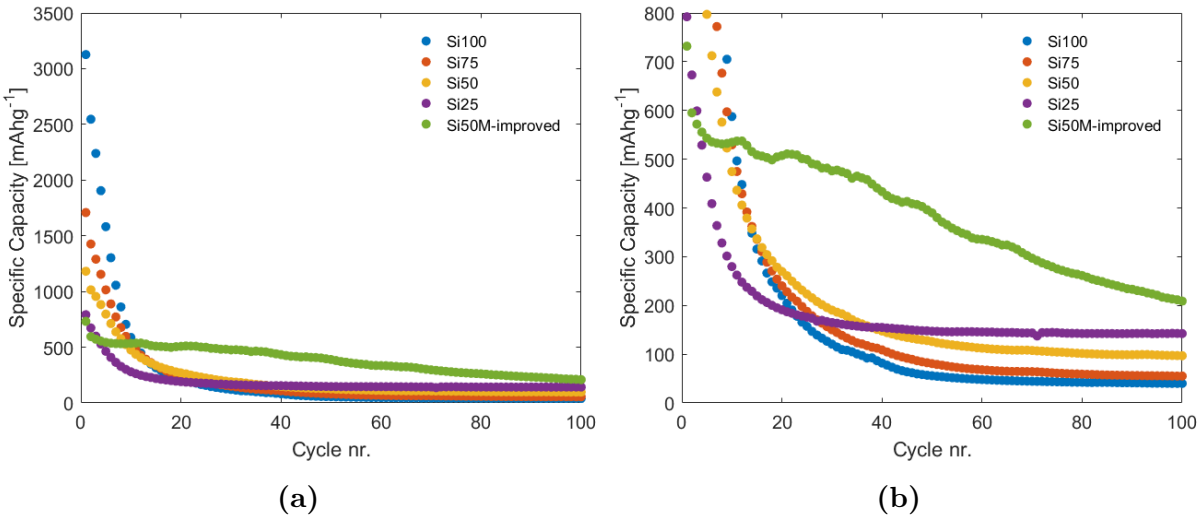

Figure 4.8: (a) Specific charge capacity of Si and SiO_2/Si composites. (b) Close up of (a). Details on the cycling programs can be found in Table 3.3

4.3.2.3 Electrochemical reduction

The effect of the electrochemical reduction program can be observed in Figure 4.9. PM-35CB-EC/H48 and SM-35CB-EC/H48 is plotted a against a reference P-35CB-EC/L, which did not undergo any reduction step. The best performing cell, PM-35CB-EC/H48 had a final capacity of 800 $mAhg^{-1}$ after 100 cycles, compared to 168 $mAhg^{-1}$ for P-35CB-EC/L.

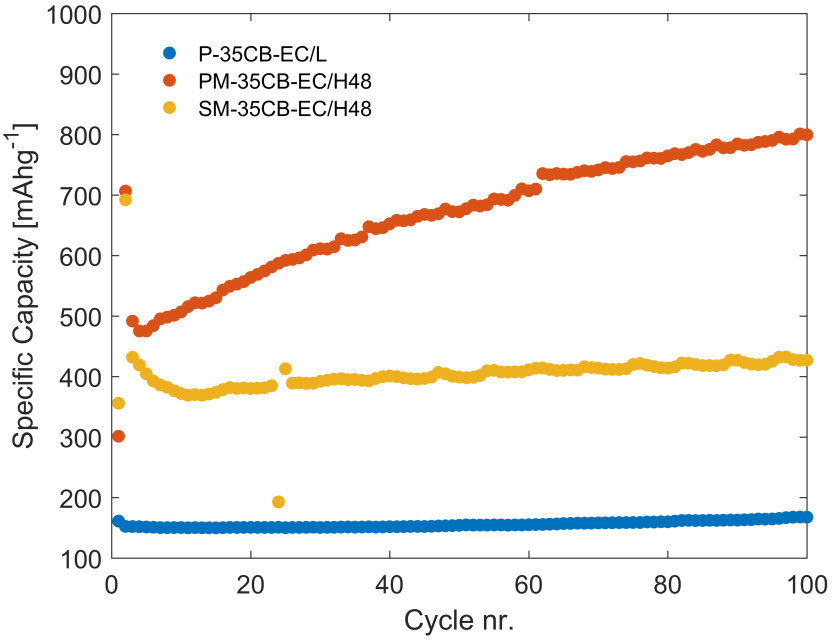

Figure 4.9: Specific charge capacity curves for cells undergone a 48h electrochemical reduction step at 0.002 V, with P-35CB-EC/L as a reference. Details on the cycling programs can be found in Table 3.3.

4.3.2.4 Differential capacity analysis

Differential capacity plots of a selection of cell from phase 1 are presented in Figure 4.10. Figure 4.10a, 4.10b, show the first 100 cycles of cells that did note undergo the electrochemical reduction step (S-25CB-EC/L and P-35CB-EC/L). In both cases, two large peaks can be seen in the cathodic direction of the first cycle at 0.75 and 0.02 for S-25CB-EC/L, 0.79 V and 0.02 V for P-35CB-EC/L respectively. In the anodic direction, two broad peaks can be observed at 0.17 V and 0.98 V for S-25CB-EC/L, and for P-35CB-EC/L peaks can be observed at 0.09 V and 0.93 V.

In the next 100 cycles only one broad peak can be seen in both the cathodic and the anodic direction for both cells. In S-25CB-EC/L, the cathodic and anodic peak is at 0.02 V and 0.16 V respectively. The cathodic and anodic peak in P-35CB-EC/L is located at 0.02 and 0.09. Moreover, in both cells, the peaks in the cathodic direction move to higher potentials with cycle number, and the peaks in the anodic direction move to lower potentials.

Figure 4.10c show the differential capacity plot of P-35CB-EC/H48, which has undergone a electrochemical reduction step. In the first cycle, cathodic peaks can be observed at

0.79 V and 0.02 V, and a large anodic peak from 0.05 V - 0.4 V. The reduction step of the second cycle can be seen as the narrow peak at 0.002 V. After the reduction step, peak formation can be observed in the subsequent 100 cycles (Figure 4.10d). Cathodic peaks are formed at 0.19 V and 0.03 V, and anodic peaks at 0.08 V, 0.31 V and 0.48 V. Furthermore, the onset potentials of the peaks can be seen to simultaneously move to higher and lower potentials in the anodic direction and to higher potentials in the cathodic direction. A superimposed plot of the last cycle of all cells can be seen in Figure 4.10e.

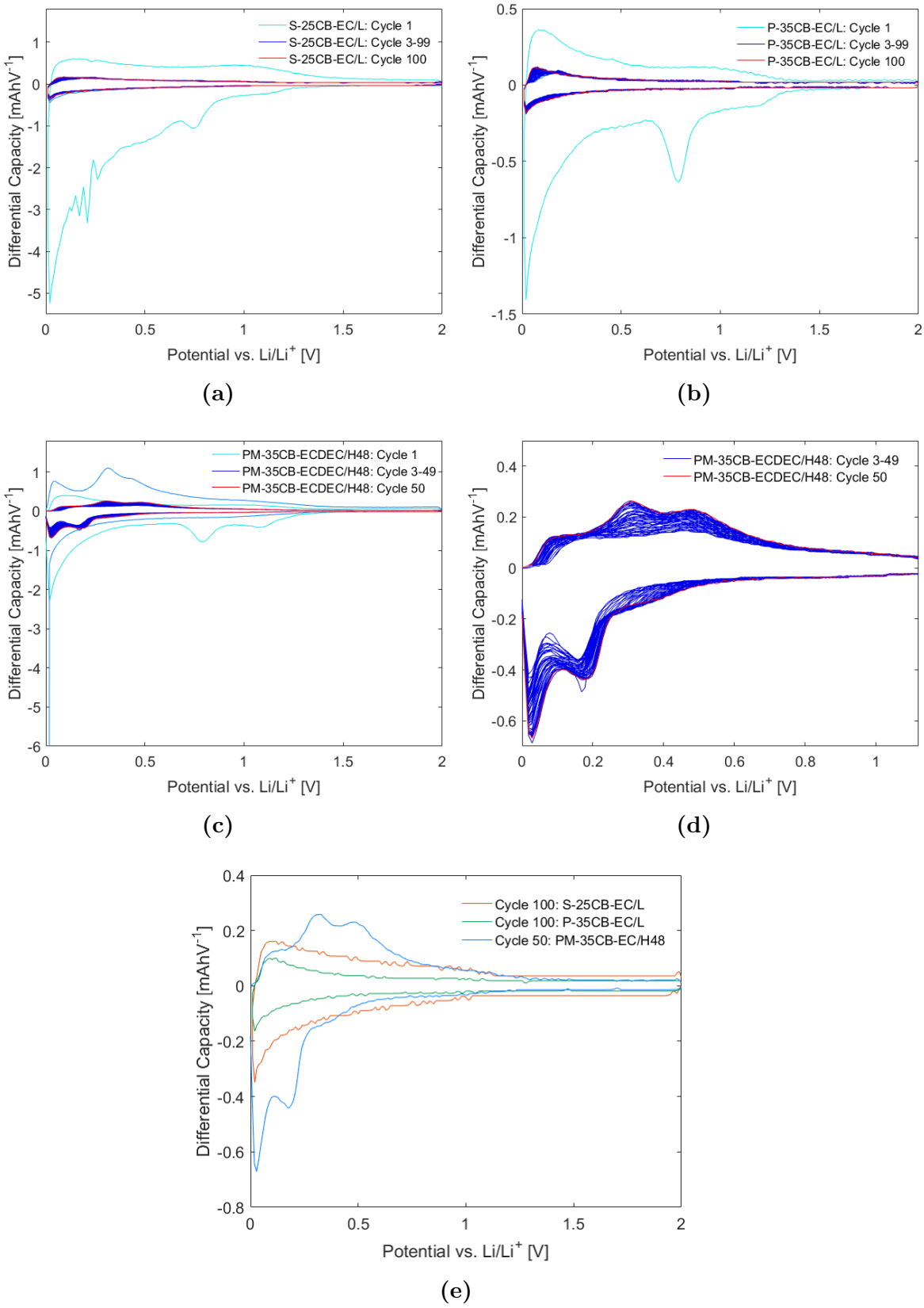

Figure 4.10: Differential capacity plot of the first 100 cycles of a selection of cell from phase 1. (a) S-25CB-EC/L, (b) P-35CB-EC/L, (c) P-35CB-EC/48h, (d) up-close view of (c). (e) Superimposed plot of the last cycle from (a), (b) and (c). Resolution of differential capacity analysis, $\Delta E = 10$ mV.

The peak potentials of PM-35CB-EC/H48 at cycle 100 (Figure 4.10d) and the peak potential of an Si-anode (presented in the Appendix section A7) are tabulated in Table 4.6. The peak potential in the SiO_2 anode can be seen to be shifted by Δ = 0.05 V - 0.06 V relative to the Si anode.

Table 4.6: Potential of anodic and cathodic peaks in differential capacity plot of Si and SiO2M-35CB see in Figure A15, 4.10. Δ indicates the difference in peak potential between Si and PM-35CB-EC.

	Potential, anodic direction vs Li/Li^+	[V]	Potential, cathodic direction vs Li/Li^+	[V]
	Peak 1	Peak 2	Peak 1	Peak 2
Si	0.26	0.43	0.09	0.25
PM-35CB-EC	0.31	0.48	0.03	0.19
Δ	0.05	0.05	0.06	0.06

4.3.3 Phase 2: Further investigation of electrochemical reduction of SiO_2

4.3.3.1 Electrochemical performance

In Figure 4.11, a representative voltage profile of the cells that have undergone electrochemical reduction is presented. The voltage profile for the reference cell in phase 2, P-35CB-EC/L, is located the Appendix, section A4.1 Figure A5.

In the initial discharge cycle, plateaus are initiated at approximately 1.3 V and 0.85 V, suggesting electrolyte decomposition. In the 3rd discharge cycle, two distinct plateaus can be observed. A sloping plateau is initiated at 1.2 V and a flatter plateau is initiated at 0.26 V. In the 100 discharge cycle of PM-35CB-EC/H48, the onset potential for the second plateau has increases to 0.28 V and the plateau has become. Comparing the voltage profile of PM-35CB-EC/H48 to P-35CB-EC/L at cycle 100, the low potential plateau is significantly longer for PM-35CB-EC/H48.

Figure 4.12 show the current profile during the electrochemical reduction step as the electrode is held at 2 mV.

Initially, the current profile of cells with pristine SiO_2 is significantly lower then that of the carbon coated SiO_2. However, after approximately 1 h the current increase in the

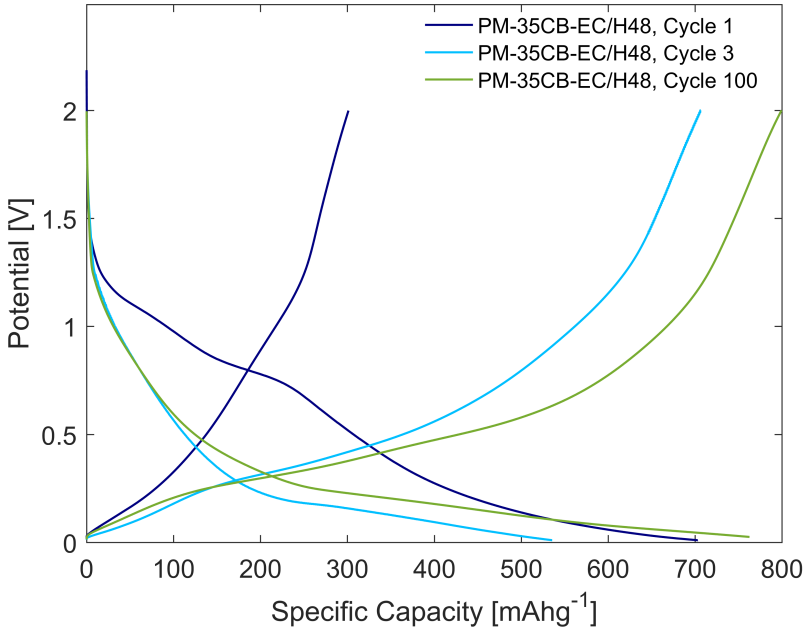

Figure 4.11: Voltage profile of cycle 1, cycle 3 and cycle 100 for PM-35CB-EC/H48.

cells with pristine SiO_2 and after 3 h the current going through the cells with pristine SiO_2 is higher compared to that of the carbon coated SiO_2. In the cells with pristine SiO_2 the presence of FEC and VC seems to reduce the current. However, in cells with carbon coated SiO_2, FEC and VC result in a higher current going through the cell.

The capacity curves of all cells in phase 2 can be seen in Figure 4.13, with P-35CB-EC/L as a reference. The capacity as a function of cycle number follow two trends. Initially, cells with pristine SiO_2 (PM-35CB-EC/H48 and PM-35CB-FEC/H48) exhibit lower capacity than cells with carbon coated SiO_2 (SM-35CB-EC/H48 and SM-35CB-FEC/H48). However, the cells with pristine SiO_2 experience a greater increase in capacity over the subsequent 50 cycles, than the cells with carbon coated SiO_2. This trend is illustrated in Table 4.7, which presents the capacity before electrochemical reduction, after electrochemical reduction and at cycle 50. In addition, the table show the gain in capacity over electrochemical reduction step (cycle 1 - cycle 3) and subsequent cycles (cycle 3 to cycle 50). Another trend observed, is that cells with FEC have a lower capacity in cell with pristine SiO_2, while cell with FEC have a higher capacity in cells with carbon coated SiO_2.

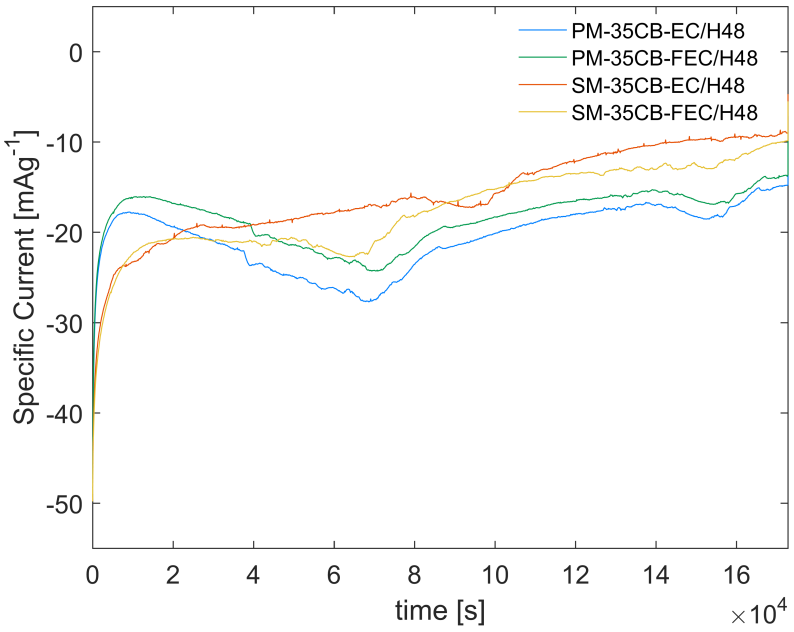

Figure 4.12: Current profiles of cells held for 48h at 0.002 V. Time normalized to t = 0, equalling the start of the hold step.

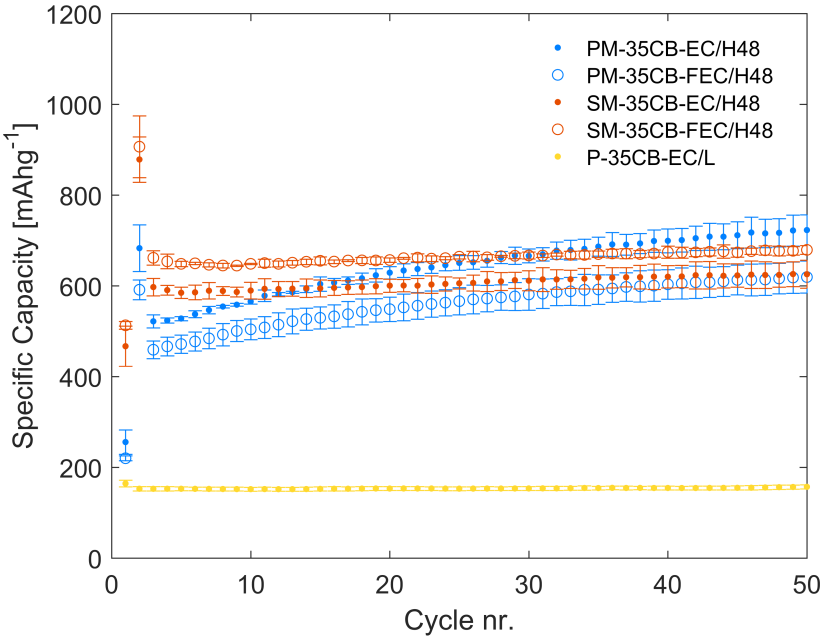

Figure 4.13: Average capacity of all cells in phase 2, with P-35CB-EC/L as a reference. Error bare indicates one standard deviation. Details on the cycling programs can be found in Table 3.3.

Table 4.7: Average capacity before reduction step, after reduction step and at cycle 50. $\Delta_{3,1}$ and $\Delta_{50,3}$, indicates the capacity increase from cycle 1 - cycle 3 and cycle 3 - cycle 50 respectively.

Cell	Cycle 1 [mAhg^{-1}]	Cycle 3 [mAhg^{-1}]	Cycle 50 [mAhg^{-1}]	$\Delta_{3,1}$ [mAhg^{-1}]	$\Delta_{50,3}$ [mAhg^{-1}]
PM-35CB-EC/H48	256	522	723	266	201
PM-35CB-FEC/H48	220	449	619	229	170
SM-35CB-EC/H48	466	597	626	130	30
SM-35CB-FEC/H48	512	662	679	150	17
P-35CB-EC/L	164	152	157	-12	5

The CE of cells in phase 2 can be seen in Figure 4.14. The same plots with error bars and tabulated values can be found in the Appendix section A4.3. In the first cycle, the CE is low for all cells, ranging from 38.91 ± 0.36 % to 46.06 ± 0.74 % for PM-35CB-FEC/H48 and SM-35CB-EC/H48 respectively. It should be noted that this is lower than the CE reported for the carbon cells in Table 4.4. However, the CE rapidly increase and approach 99%. Comparing cells with pristine SiO_2 and carbon coated SiO_2, the first cycle CE of cells with pristine SiO_2 is lower than cells with carbon coated SiO_2. Moreover, the FEC electrolyte yield a lower first cycle CE than cells with EC. However, in the last cycle, cells with FEC have the highest CE.

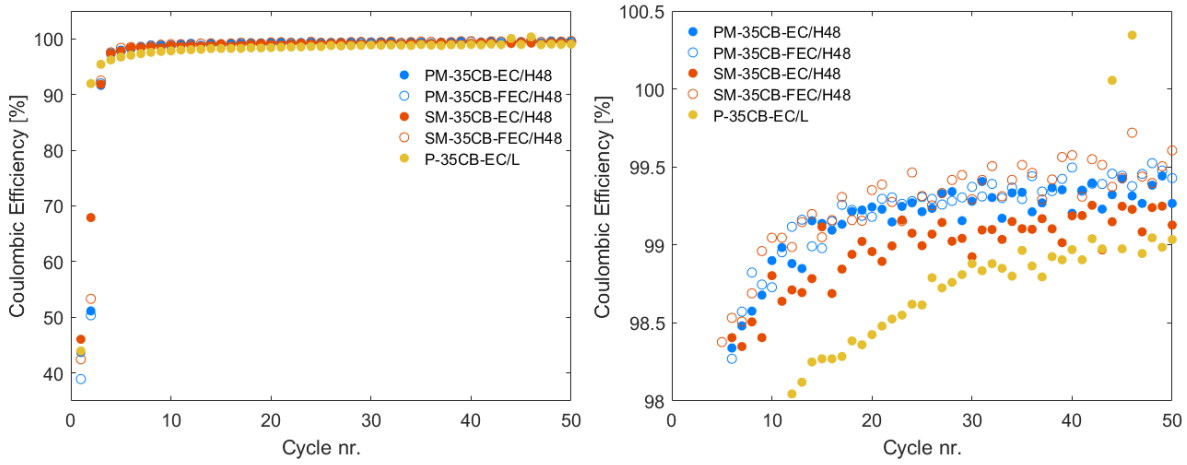

Figure 4.14: Average coulombic efficiency of cells in phase 2. (a) General trend of the coulombic efficiency over 50 cycles. (b) Enlarged view of (a).

4.3.3.2 Differential capacity analysis

Differential capacity plot of all cells in phase 2 are found in Figure 4.15. All materials systems exhibit the same general trend. In the first cycle, three main cathodic peaks can be seen. In cells with the EC electrolyte (Figure 4.15a, 4.15c), the first peak is located at 1.12 V for PM-35CB-EC/H48 and 1.46 V for SM-35CB-EC/H48. The second and third peak is located at approximately 0.800 V and 0.02 V for both PM-35CB-EC/H48 and SM-35CB-EC/H48. In the cathodic direction, PM-35CB-EC/H48 has a broad peak at 0.03 V, while SM-35CB-EC/H48 has two peaks at 0.03 V and 1.01 V. In cells with the FEC electrolyte (Figure 4.15b, 4.15d), the first cathodic peak is located at approximately 1.40 V, the second at approximately 0.09 V and the third at 0.02 V. In the anodic direction, the peaks are located at the same potential as the cells with the EC electrolyte.

During the electrochemical reduction step in cycle 2, all cells exhibit one narrow cathodic peak at 0.002 V. In the subsequent 50 cycles, peak formation can be seen in all cells. However, as seen in Figure 4.16d, the peak formation most is prevalent in cells with pristine SiO_2. Table 4.8 presents the peak potential at the 50th cycle of all materials system.

In cells with the pristine SiO_2 (Figure 4.15a, 4.15b), it can be observed that onset potential for the peak formation change significantly through cycling. In the cathodic direction, the onset potential for peak formation shifts to higher potentials. In the anodic direction, the onset potential can be seen to shift to both higher and lower potentials. Some shift in the onset potential can also be seen in cell with the carbon coated SiO_2 (Figure 4.15c, 4.15d). However, this shift is small compared to cells with pristine SiO_2.

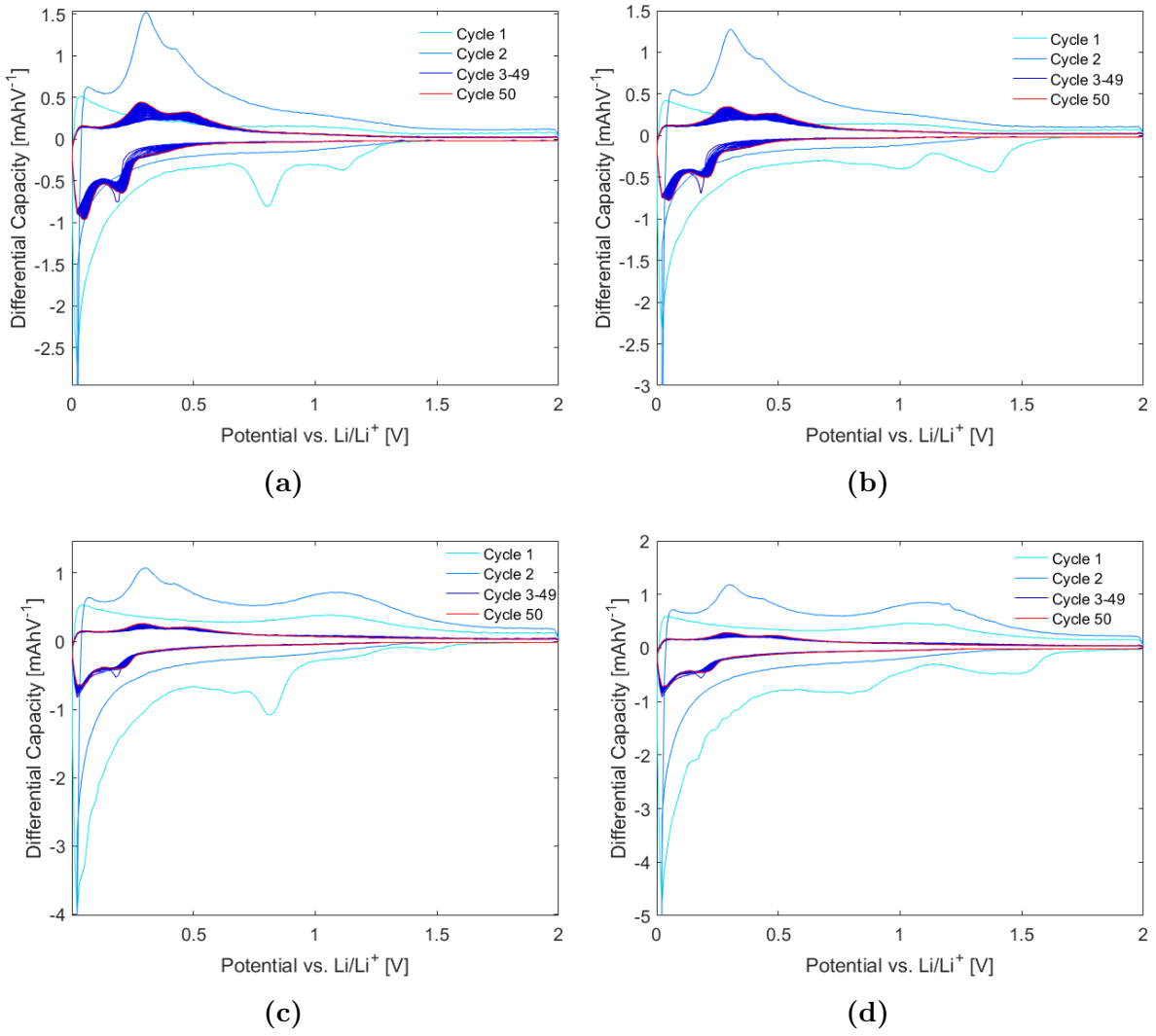

Figure 4.15: Differential capacity plots of all cells in phase 2, displaying cycle 1 - cycle 50. (a) PM-35CB-EC/H48, (b) PM-35CB-FEC/H48, (c) SM-35CB-EC/H48 and (d) SM-35CB-FEC/H48. Resolution of differential capacity analysis, $\Delta E = 10$ mV.

In Figure 4.16, superimposed plots of all materials systems in phase 2 at different cycles are presented. Figure 4.16a, shows the first cycle. The initial cathodic peak of cells with the FEC, can be seen to limit the peak formation at 0.80 V, relative to cells with the EC electrolyte. In the 3rd cycle (Figure 4.16b), peaks in both the cathodic and anodic direction can be seen to reside at the same potential for all cells. In Figure 4.16c, some difference in the potential of the second peak in the cathodic direction can be seen. In cells with carbon coated SiO_2 this peak is at 0.022 V, while the same peak is located at 0.05 V in cells with pristine SiO_2. In Figure 4.16d, cycle 3-50 of all material systems are superimposed, demonstrating the relative height and width of all peaks.

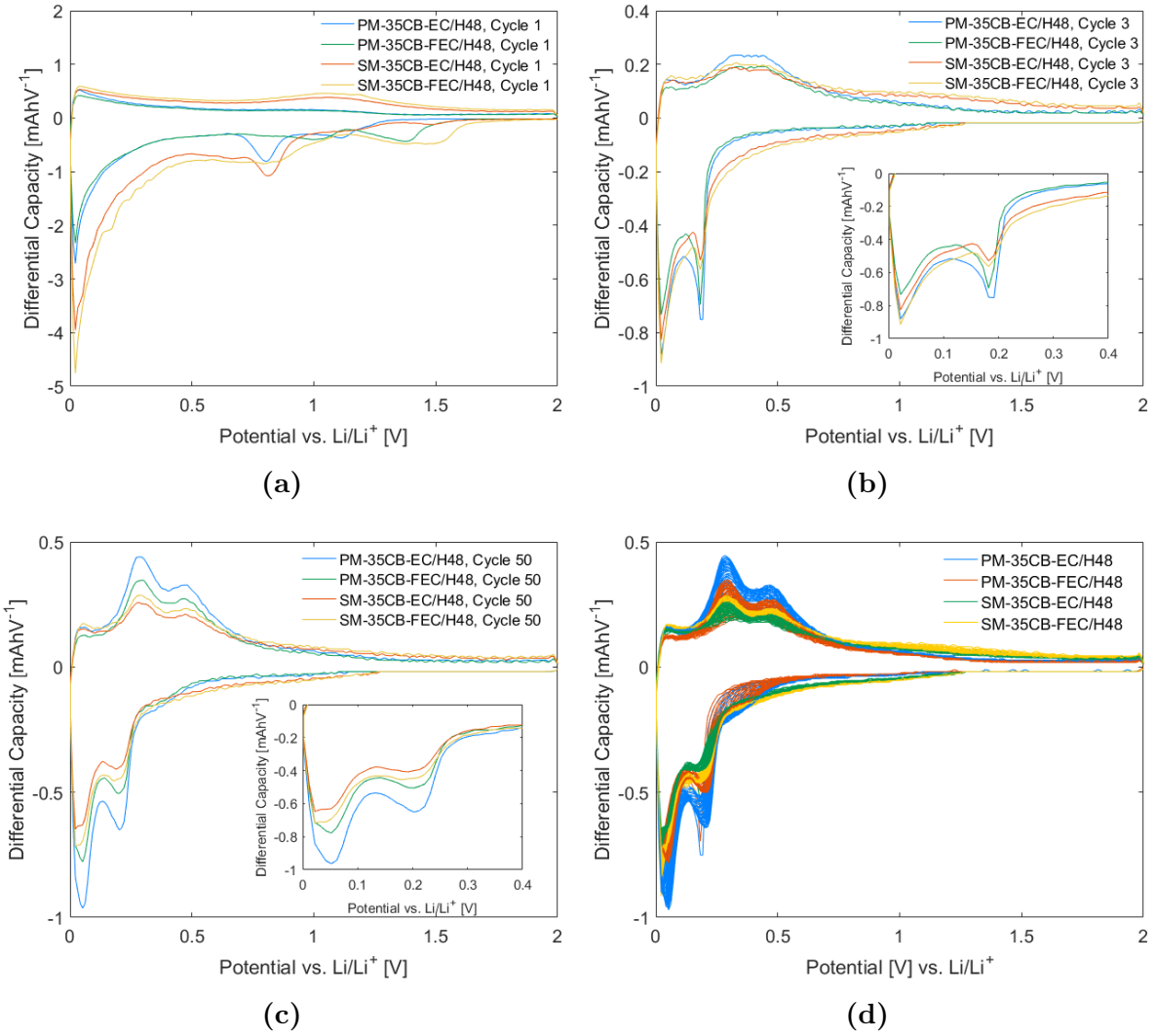

Figure 4.16: Superimposed differential capacity plots of all material systems in phase 2. (a) cycle 1, (b) cycle 3 and (c) cycle 50, (d) cycle 3-50. Resolution of differential capacity analysis, $\Delta E = 10$ mV.

4.3.3.3 Rate performance

In Figure 4.17, the rate performance of all cells in phase 2 is presented. All the cells demonstrate excellent rate performance up to 1000 mAg^{-1}. However, at 2000 mAg^{-1}, the capacity of the cells collapse. When the specific current is reversed back to 100 mAg^{-1} the capacity is recovered by more than 100 % in all cells with the exception of SM-35CB-EC/H. The capacity retention of the last cycle at 1000 mAg^{-1} and 100 mAg^{-1}, is presented in Table 4.9.

Table 4.8: Peak potentials in differential capacity plot of cells in phase 2 after 50 cycles.

Cell	Peak potentials anodic direction vs Li/Li^+ [V]		Peak potentials cathodic direction vs Li/Li^+ [V]	
	Peak 1	Peak 2	Peak 1	Peak 2
PM-35CB-EC/H48	0.28	0.49	0.05	0.20
PM-35CB-FEC/H48	0.28	0.47	0.05	0.21
SM-35CB-EC/H48	0.29	0.47	0.03	0.20
SM-35CB-FEC/H48	0.29	0.48	0.02	0.19

The CE of the cells under the rate capability test is reduced compared to regular cycling (Figure 4.18a, 4.18b). Nevertheless, with exception of the cycles at 2000 mAg^{-1}, the CE of all cells is above 97 % for all currents.

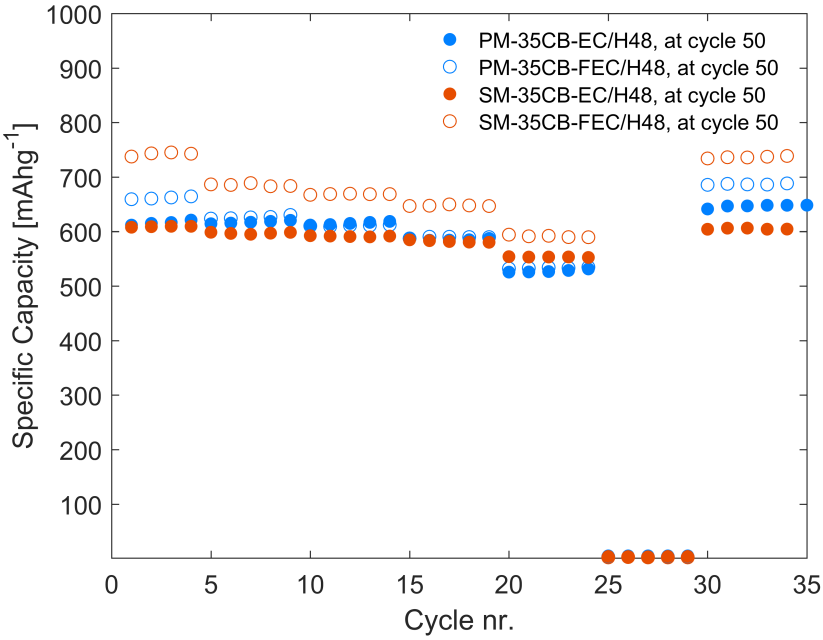

Figure 4.17: Rate performance of cells in phase 2. Specific currents: 100 mAg^{-1}, 200 mAg^{-1}, 300 mAg^{-1}, 500 mAg^{-1}, 1000 mAg^{-1}, 2000 mAg^{-1} and 100 mAg^{-1}.

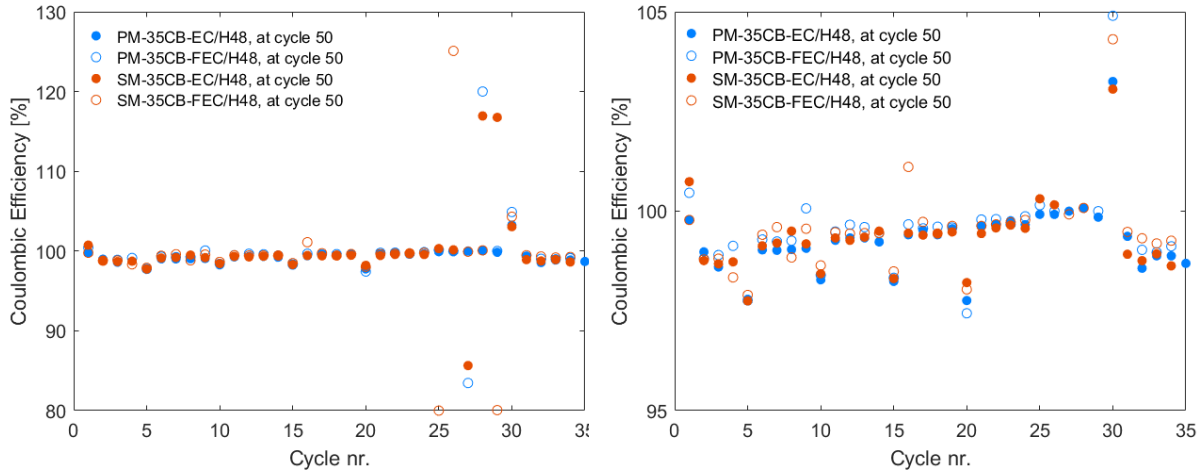

Figure 4.18: (a) Coulombic efficiency of cells under rate performance test. (b) Up-close view of (a). Currents: 100 mAg^{-1}, 200 mAg^{-1}, 300 mAg^{-1}, 500 mAg^{-1}, 1000 mAg^{-1} and 2000 mAg^{-1}.

Table 4.9: Overview of capacity retention of the last cycle at 1000 mAg^{-1} and 100 mAg^{-1} (cycle 35), relative to first cycle at 100 mAg^{-1}.

Electrode	Cap. retention at 1000 mAg^{-1} [%]	Cap. retention at 100 mAg^{-1} [%]
PM-35CB-EC/48H	86.9	106
PM-35CB-FEC/48H	81.1	104
SM-35CB-EC/48H	90.9	99.4
SM-35CB-FEC/48H	80.0	100

4.3.3.4 Electrochemical impedance spectroscopy

Nyquist plot of EIS measurements carried out in fully lithiated state (0.01 V) after cycle 1, cycle 3 and cycle 3 are presented in Figure 4.19. Due to limited time, only three of the four material systems explored in phase 2 were tested. Thus, no EIS measurements were conducted on SM-35CB-FEC/H48. Nyquist plot of EIS measurements conducted both in lithiated and delithiated state (2.00 V) are located in the Appendix section A4.4. Tabulated values of R_1, R_2, R_3 and C_1, calculated on the basis of the equivalent circuit presented if Figure 4.19a, are presented in Table 4.10.

Based on the equivalent circuit, R_1, R_2 and R_3 can be view as representative of the

resistance of the electrolyte (R_e), resistance of the SEI layer (R_{SEI}) and the charge transfer resistance (R_{CT}) respectively. The fitted data appears to be in good agreement with the experimental data.

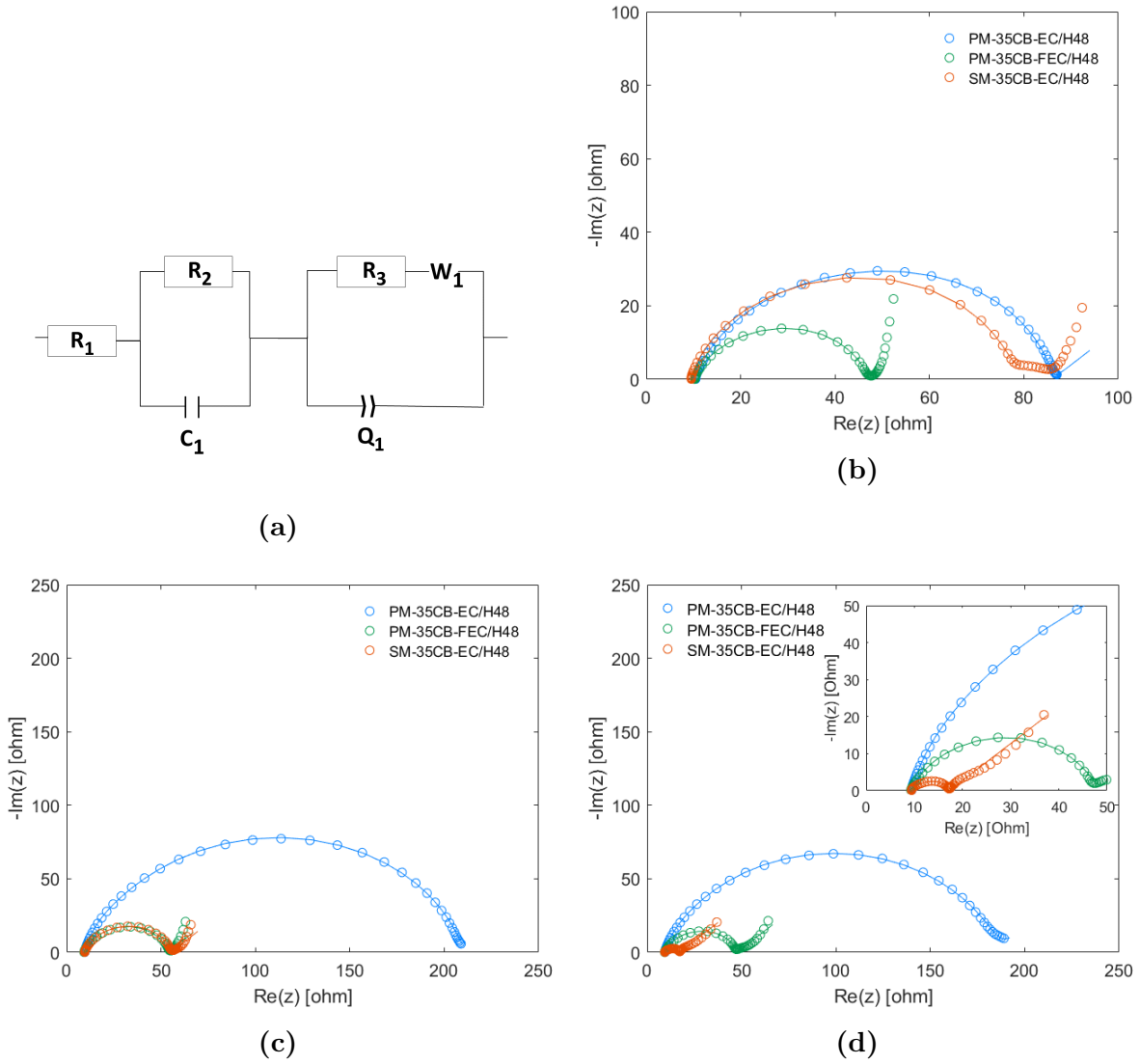

Figure 4.19: Nyquist plot of three electrode cells with different anode and electrolyte composition. (a) Equivalent circuit used for data fitting. Nyquist plot of lithiated state at (b) cycle 1, (c) cycle 3 and (d) cycle 10. Q_1 represents a constant phase element. Frequency range: 500 000 000 - 0.01 Hz. Amplitude: 10 mV vs Li/Li^+. V_{cell} = 0.01 V vs Li/Li^+.

Table 4.10: Estimated values of R and C based on fitting of the equivalent circuit in Figure 4.19.

Cell	R_1 [ohm]	R_2 [ohm]	R_3 [ohm]	C_1 [F]
PM-35CB-EC/H48				
Cycle 1	10.31	19.31	56.48	21.81e-6
Cycle 3	9.67	8.68	191	12.17e-6
Cycle 10	9.29	3.98	171.5	24.68e-6
PM-35CB-FEC/H48				
Cycle 1	10.13	7.85	29.01	30.52e-6
Cycle 3	9.28	2.03	42.25	9.58e-6
Cycle 10	9.416	4.22	34.09	85.66e-6
SM-35CB-EC/H48				
Cycle 1	9.39	19.67	49.28	18.89e-6
Cycle 3	9.46	8.60	37.17	28.84 e-6
Cycle 10	9.62	1.45	6.2	5.64e-6

4.4 Characterization of electrodes pre- and post-cycling

4.4.1 Electrode microstructure and morphology

In this section, SEM micrographs of the electrodes before and after cycling are presented. As the electrodes were taken from phase 2, all cycled electrodes had undergone an electrochemical reduction step and were cycled for 50 cycles.

4.4.1.1 Surface overview

An overview of the electrodes surface before and after cycling is presented in Figure 4.20. Figure 4.20a and Figure 4.20b show electrodes with unmilled and milled SiO_2 frustules respectively. The Figures indicates a massive reduction of size after milling, and that there is some crack formation in the electrodes before cycling.

Figure 4.20c, presents the surface of SM-35CB-EC/H48 after cycling, which is representative of all electrode after cycling. An overview of all cycled electrodes is found in the Appendix section A5.1. Crack formation is slightly more prevalent in cycled electrodes

(Figure 4.20b) relative to the uncycled electrodes (Figure 4.20b). No significant difference in crack formation could be seen in the cycled cells in phase 2.

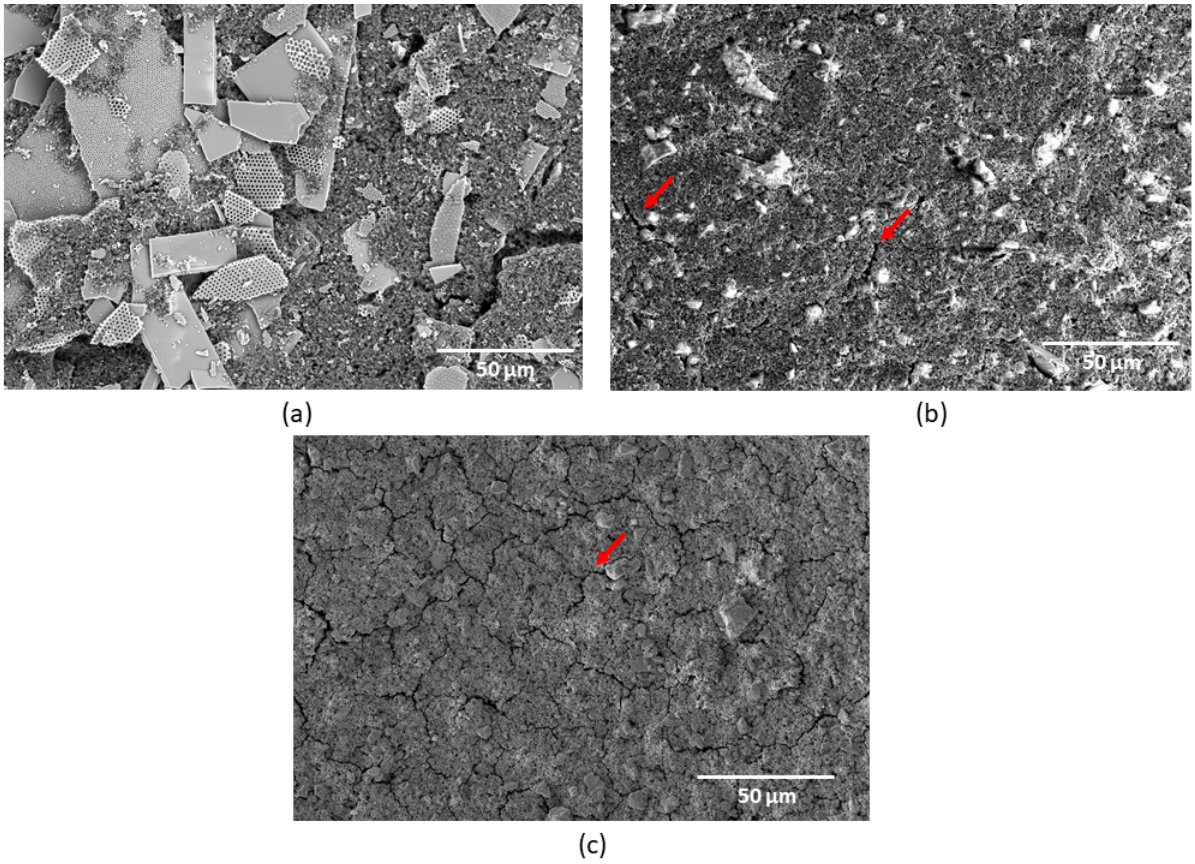

Figure 4.20: SEM images of electrodes. (a) uncycled P-35CB, (b) uncycled PM-35CB and (c) SM-35CB-EC/H48 after 50 cycles. Arrows indicate crack formation in the electrode.

A large variety in surface film formation was found after cycling. Figure 4.21 and Figure 4.22 present SEM images of surface film formation on electrodes with pristine SiO_2 and carbon coated SiO_2 respectively.

Electrodes with pristine SiO_2

Figure 4.21 presents up-close micrographs of electrodes with pristine SiO_2 (PM-35CB-EC/H48 and PM-35CB-FEC/H48) after cycling. In most cases, the SiO_2 particles on the surface of the electrodes showed no signs of film formation. Moreover, the nanostructure of the particles was mostly intact (4.21b, 4.21e), indicating limited volume expansion during cycling. However, as demonstrated in Figure 4.21c, 4.21f, some film formation was identified on a limited number of the SiO_2 particles. No significant difference was

found in the amount of film formation in cells cycled in FEC or EC. However, the surface films appear to have different morphologies. The film formed on electrodes cycled FEC contained more spherical decomposition products. This in demonstrated in Figure 4.21f, and is in agreement with the SEI films observed in similar material systems in the literature [60].

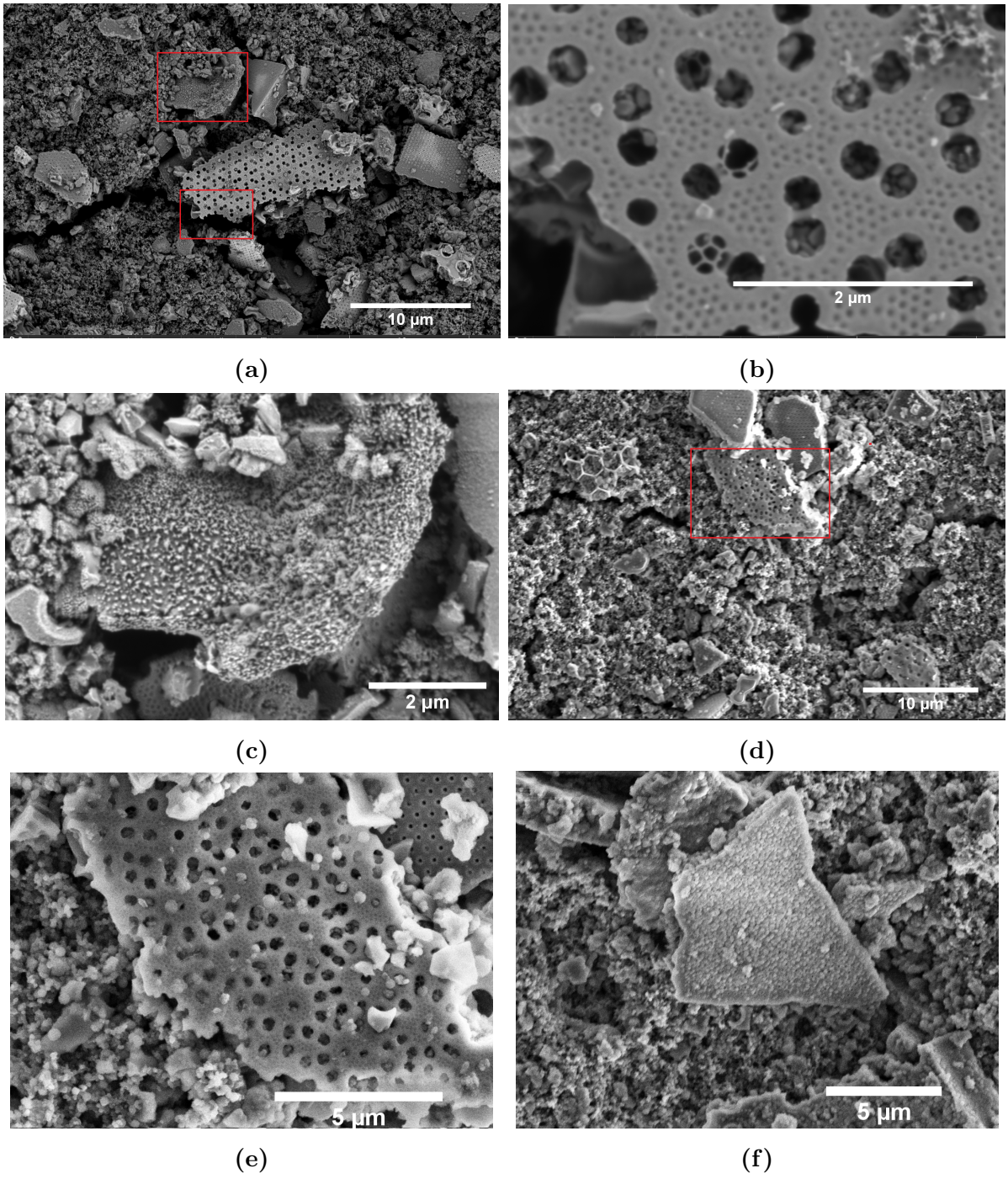

Figure 4.21: SEM micrographs of SiO_2 particles on; (a)-(c) PM-35CB-EC/H48 and (d)-(f) PM-35CB-FEC/H48, after 50 cycles.

Electrodes with carbon coated SiO_2

Film formation was observed on all carbon coated SiO_2 particles (Figure 4.22). In both SM-35CB-EC/H48 (Figure 4.21a, 4.21b) and SM-35CB-FEC/H48 (Figure 4.21c, 4.21d) thick films completely cover the SiO_2 particles, making it impossible to see the morphology of the SiO_2 particles. That the structures observed in Figure 4.21 indeed were SiO_2 particles, was confirmed by exposing the structure to a high current electron beam, thereby removing the surface film and exposing the SiO_2 particles. The result of this exposure can be seen in the Appendix, section A5.

The morphology of the film formed on the particles was also in this case dependent on the electrolyte composition. The decomposition products formed on SM-35CB-FEC/H48 (Figure 4.21c, 4.21d) were more spherical than the decomposition products seen in SM-35CB-EC/H48 (Figure 4.21a, 4.21b).

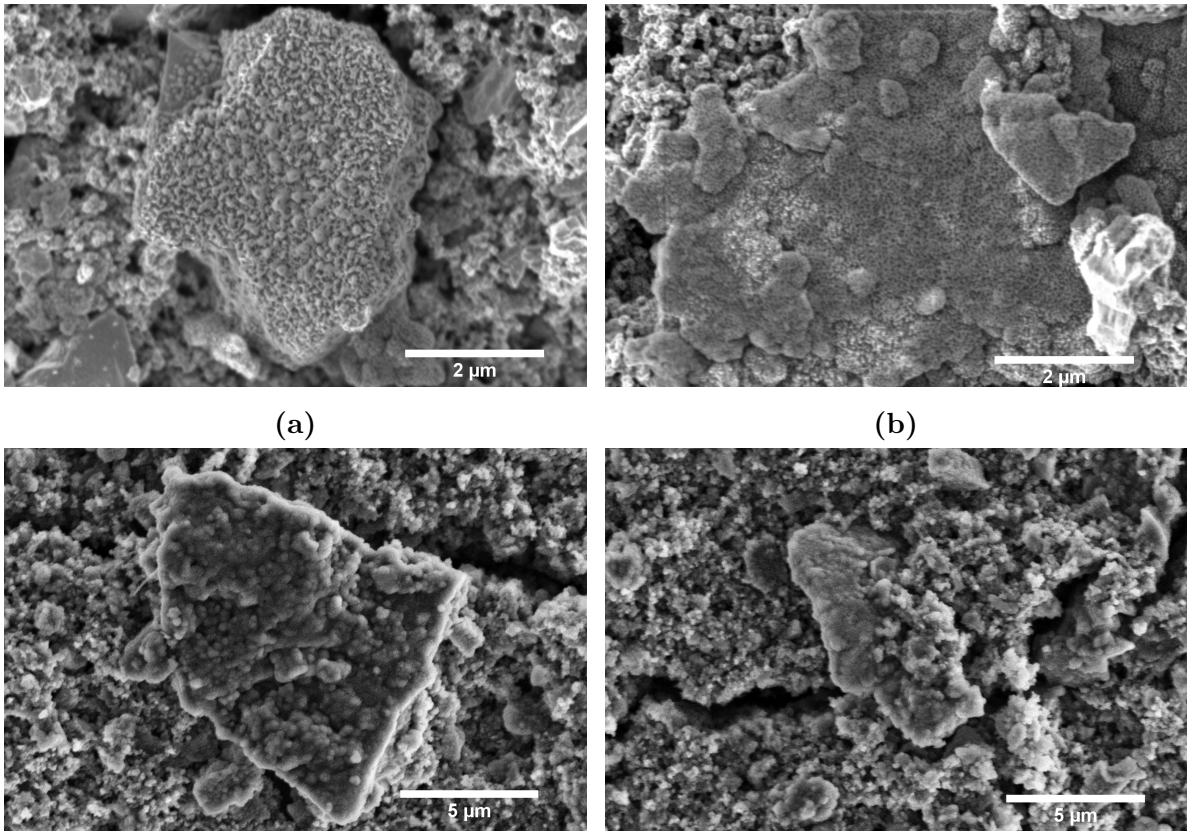

Figure 4.22: SEM micrographs of film formation on SiO_2 particles on; (a)-(b) SM-35CB-EC/H48 and (c)-(d) SM-35CB-FECVC/H48, after 50 cycles.

4.4.1.2 FIB cross-section

FIB cross-sections of the electrodes in phase 2 are presented in Figure 4.23. Figure 4.23a and 4.23b, demonstrates large difference in the density and the number of cavities, in electrodes with milled (PM-25CB) and unmilled SiO_2 (P-25CB).

The cross-section micrographs of the electrodes with pristine SiO_2 (PM-35CB-EC/H48 and PM-35CB-FEC/H48) in Figure 4.23c and Figure 4.23d respectively, indicates that the microstructure of the SiO_2 particles in the bulk of the electrode is intact after cycling. In PM-35CB-EC/H48 (Figure 4.23c), film formation in the bulk of the electrode can be observed, as the CB particles appears to be "fused together". This form of bulk film formation appears to be limited in PM-35CB-FEC/H48 (Figure 4.23d), as a more porous structure can be observed.

The cross-section micrographs of the electrodes with carbon coated SiO_2 (SM-35CB-EC/H48 and SM-35CB-FEC/H48) in Figure 4.23e and Figure 4.23f show extensive film formation in the bulk of the electrode. In SM-35CB-EC/H48 (Figure 4.23e) it is difficult to distinguish between CB and SiO_2 particles. Film formation in the bulk of the electrode was also observed in SM-35CB-FEC/H48 (Figure 4.23f). However, the structures in Figure 4.23f seems more porous than the structures in Figure 4.23e.

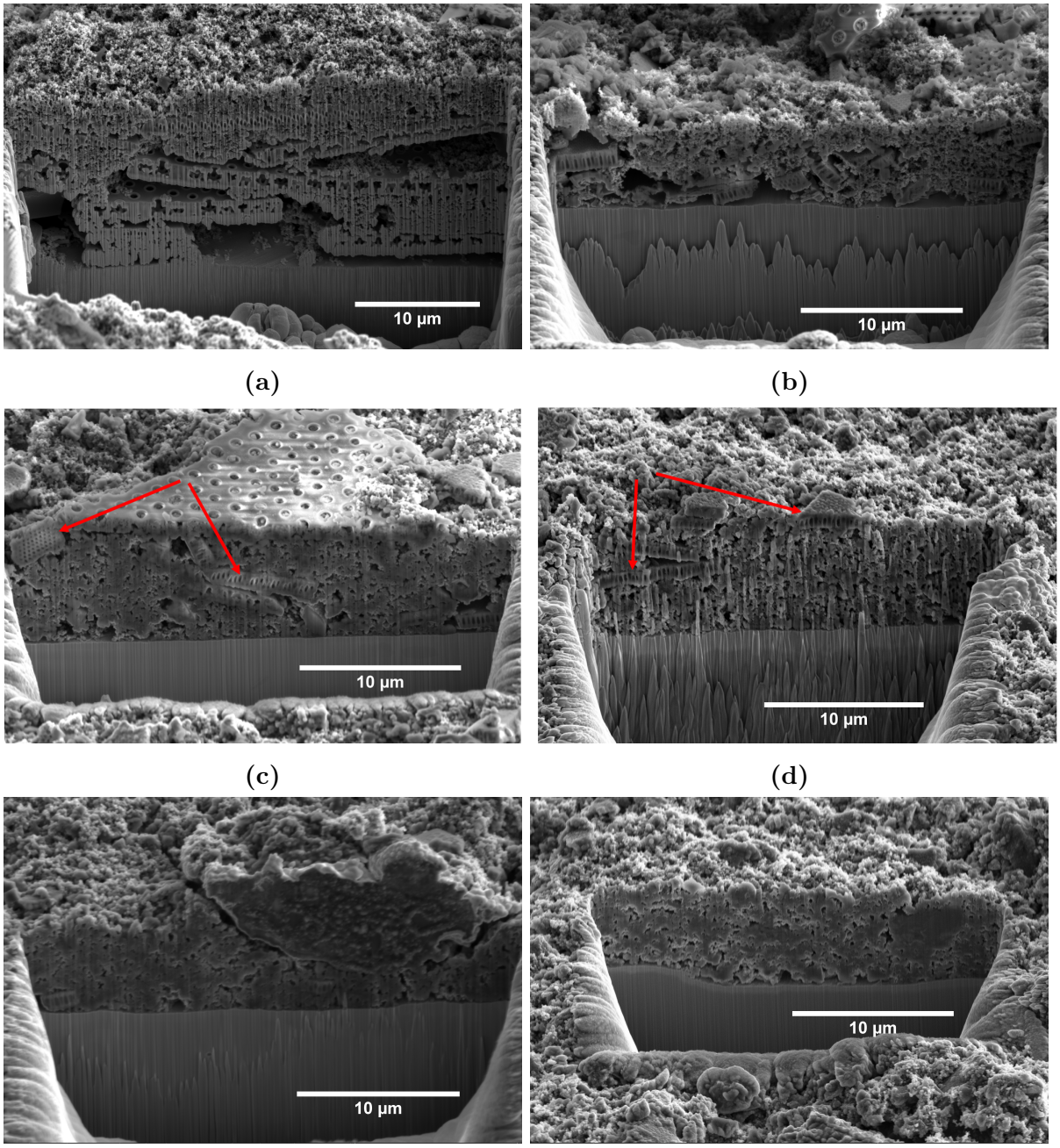

Figure 4.23: SEM micrographs of FIB cross-section of; (a) uncycled P-35CB, (b) uncycled PM-35CB, (c) cycled PM-35CB-EC/H48, (d) cycled PM-35CB-FEC/H48, (e) cycled SM-35CB-EC/H48 and (f) SM-35CB-FEC/H48. Arrows indicates the porous structure of the frustules still visible after cycling.

4.4.2 EDX mapping of electrode surface

EDX maps of a PM-35CB-EC electrode before and after cycling are presented in Figure 4.24 and Figure 4.25 respectively. Before cycling (Figure 4.24b), the O Kα1 and Si Kα1 signal coincide well. This indicates that most of the oxygen signals come form the SiO_2 particles. This is further illustrated by the fact that the signal from C Kα1_2 and O Kα1 is almost inverse, i.e. limited oxygen is observed on the CB.

After cycling (Figure 4.25b), the O Kα1 signal is present over the entire surface of the electrode, also in areas with C Kα1_2 signals. Moreover, the mapping of Si Kα1 show that the SiO_2 particles are scattered in confined domains, exuding the possibility of the O Kα1 signal being caused by a more homogeneous distribution of SiO_2 particles after cycling. Thus, it is reasonable to believe that the O Kα1 signals is caused by oxygen rich decomposition products formed during cycling. Furthermore, the presence of C Kα1_2 and O Kα1 signals from the same area indicates that the decomposition products also are present on the surface of CB. This observation is of importance, as it suggests that decomposition products most likely are over the entire surface of the electrodes, even though it cannot be seen in the SEM. This underscores the limitation of SEM as a characterization tool, as only thick films can be observed.

In an attempt to determine the relative concentration of fluorine on the surface of the electrodes of phase 2 after cycling, EDX mapping of the surface was conducted. The reported counts per second (cps) of fluorine from all electrodes in phase 2 is reported in Table 4.11. The values were acquired by reading off the value on the respective spectra, presented in the Appendix section A6. The results show that more fluorine is present on the electrodes with carbon coated SiO_2. Moreover, the result also indicates that cells cycled in FEC has a higher fluorine content after cycling, than equivalent cells with EC.

Table 4.11: Tabulated values of the cps of fluorine in the EDX spectra of electrodes in phase 2 after cycling.

Electrode	cps
PM-35CB-EC/H48	0.62
PM-35CB-FEC/H48	0.7
SM-35CB-EC/H48	2.0
SM-35CB-FEC/H48	11

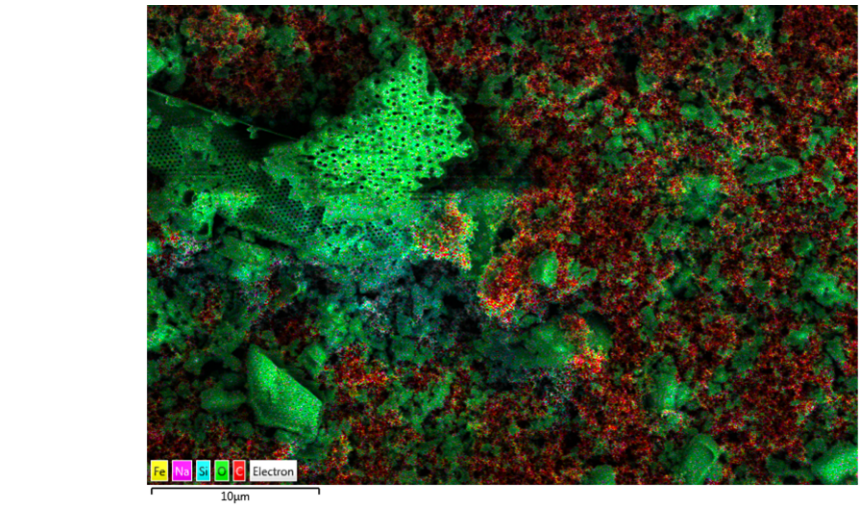

(a)

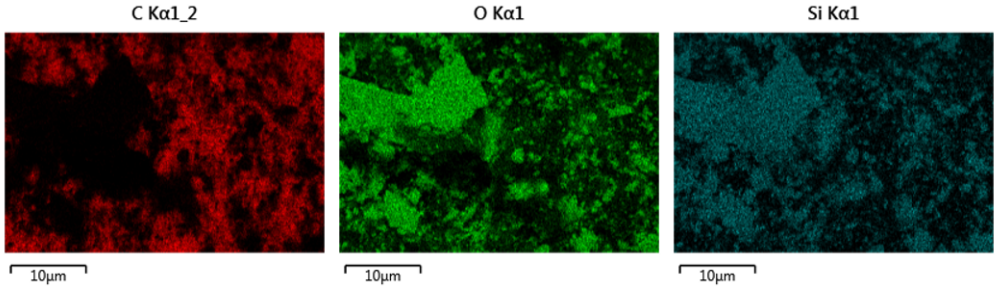

(b)

Figure 4.24: EDX mapping of PM-35CB-EC/H48 before cycling. (a) Layered mapping of all elements, (b) mapping of C Kα1_2, O Kα1 and Si Kα1 respectively. EDX conducted at 5.00 kV.

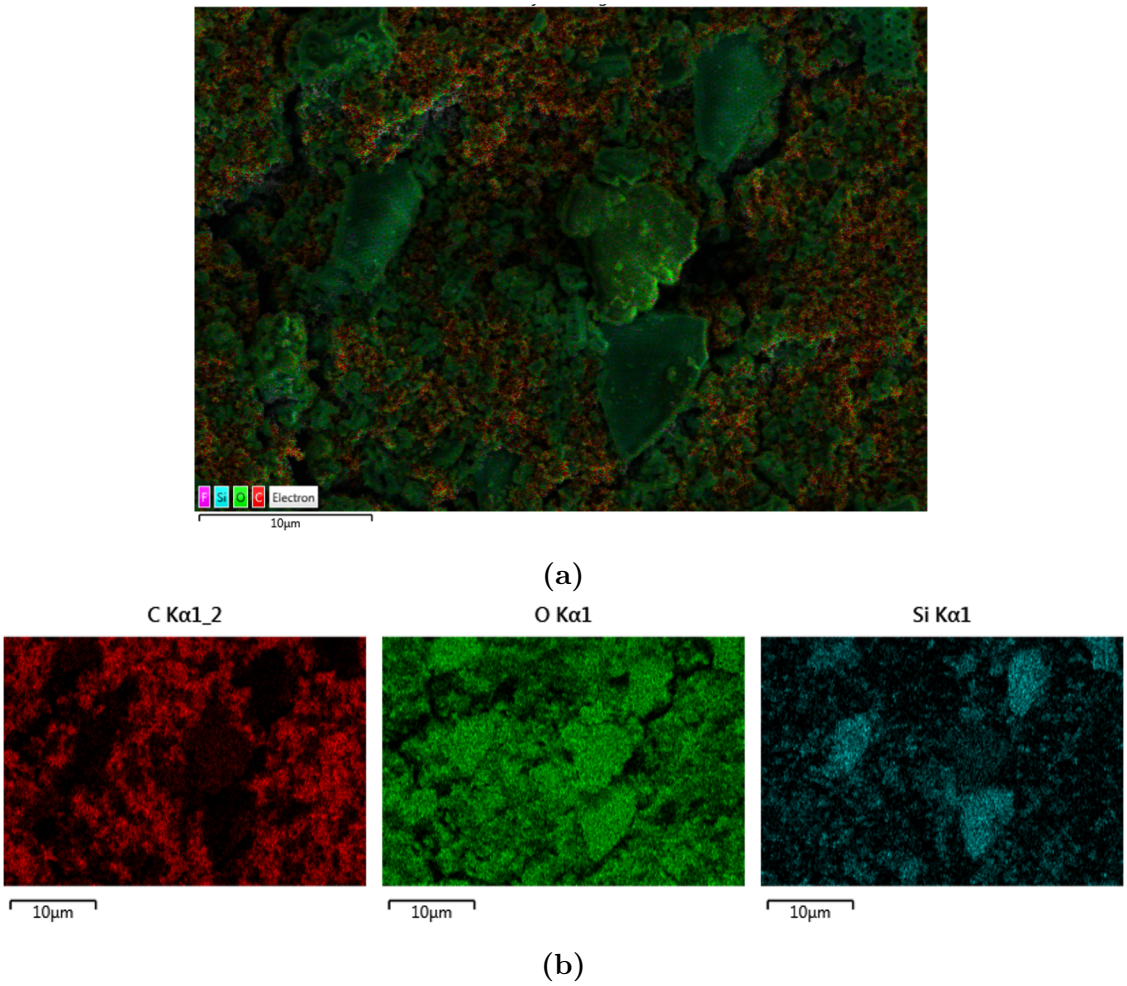

Figure 4.25: EDX mapping of PM-35CB-EC/H48 after cycling. (a) Layered mapping of all elements, (b) mapping of C Kα1_2, O Kα1 and Si Kα1 respectively. EDX conducted at 5.00 kV.

Chapter 5: Discussion

5.1 Characterization of extracted SiO_2 and active material

5.1.1 Notes on extracted SiO_2

The SEM micrographs in Figure 4.2 are representative of SEM micrographs acquired from all batches of processed diatoms. Large accumulation of organic materials are relative easily observed in SEM, but no such observations were made. This indicates that most of the organic material was removed during the washing and calcination process. The broad peak at 22 ° in the XRD plot indicates that the purified frustules mainly consist of amorphous SiO_2. Finally, the lack of any crystalline peaks in Figure 4.1 also demonstrates that most inorganic material, such as NaCl and KCl, was successfully removed.

Even though the SEM micrographs and XRD diffractograms give compelling evidence for the purity of extracted SiO_2 frustules, the purity of this sample should be considered as low compared to that supplied by the chemical industry. SEM micrographs only gives snapshots of the sample, thus the presence of large organic impurities cannot be excluded. Furthermore, XRD diffractograms can only detect crystalline impurities and the detection limit is about 2-3 wt%. Thus, small amounts of inorganic impurities could be present.

5.1.2 Characterization of active material

5.1.2.1 Size, morphology and surface area of the frustules

The SEM micrographs and the laser diffraction data demonstrated that the size of the frustules was quite large, 40 um before milling and 3.09 um after milling. Moreover, the nitrogen adsorption data seen in Table 4.2 show that the increase in surface area after milling is mainly in the external area. This imply that the milling has not change the fundamental microstructure of the frustules, but rather broken the larger frustules participles into smaller pieces.

By consulting section 2.4.1, it is evident that most of the SiO_2 used in the literature is smaler than a couple of hundred nm and often exhibits a mesoporous structures. The largest structures identified in the literature, is that by Wang et al., who used highly mesoporous and hollow spheres with a diameter of 0.5 um - 1 um [13]. Thus, the macro structure of the frustules both before and after milling is significantly larger than most of the SiO_2 used in the literature. This might hamper the performance of the silica, as lithiation of SiO_2 traditionally is attributed to nano-silica [67]. However, the relative high fraction of external t-plot area observed (Figure 4.4), and the microstructures observed in the SEM micrographs (Figure 4.2), indicates that the frustules have a mesoporous nature similar to that used in the literature. If this is the case, anodes with SiO_2 from frustules might exhibit some of the benefits of porosity described in section 2.4.4.

5.1.2.2 Characterization of the carbon coating

The large surface area yielded by the sucrose coating relative to the cornstarch coating (Figure 4.4), might be attributed to differences in the carbon coating, or it could be caused by the increased amount of carbon in the sucrose coated SiO_2 (Table 4.3). From Figure 4.4 it is also evident that the sucrose precursors yield a larger external surface area than the cornstarch precursor. The distinction between micropores and external area is of importance, as the radius of micropores is smaller than the solvated radius of Li^+ ions, limit transportation of Li^+ through the carbon coating [100]. Thus, a carbon coating with a large concentration of micropores might prevent transportation of Li^+ from the electrolyte to the SiO_2 surface. Nevertheless, the exposure of the micropores to the electrolyte may result in increased SEI formation. Thus, an increase in the micropore area over the external area is unwanted, as it facilitates SEI formation and may limit Li^+ diffusion to the surface.

5.2 Capacity contribution from carbon

The high capacity of the pyrolyzed sucrose may be attributed to the high surface area of pyrolyzed sucrose observed in Figure 4.4. Even though the capacity of the pyrolyzed sucrose far exceed that of graphite, the capacity is in agreement with that reported for amorphous carbon by Dahn et al. [37]. Finally, it should also be noted that the standard deviation of the carbon cells is quite large. This suggest that the capacity contribution of carbon in individual SiO_2 cells might vary, and that the presence of carbon could be a significant source of uncertainty in cells with SiO_2.

5.3 Initial screening of SiO_2 derived from diatom frustules

5.3.1 Capacity of SiO_2 anodes

The capacity of both of pristine and carbon coated SiO_2 was low. The best performing cell with unmilled and pristine SiO_2 (P-35CB-EC/L) had a final capacity of 170.6 $mAhg^{-1}$, which is far lower than the reported capacity of milled SiO_2 (α quarts) by Chang et al., at approximately 800 $mAhg^{-1}$ [8]. The best performing cell with unmilled carbon coated SiO_2 (S-25CB-EC/L) had a final capacity of 188 $mAhg^{-1}$, only slightly higher than the cell with pristine SiO_2. This is somewhat surprising, as the capacity contribution from carbon alone was estimated to 224.7 $mAhg^{-1}$ (Table 4.5). Moreover, the capacity of the carbon coated SiO_2 is significant lower than the 437 $mAhg^{-1}$ reported by Nysteen, for almost the identical material system [16].

The difference in capacity of the carbon coated SiO_2 could be caused by a verity of factors. In Nysteens work, the cells were cycled between 0.00 V - 3.00 V at 50 mAg^{-1}. As demonstrated in Figure 4.7f, utilizing a cycling window between 0.01 V and 3.00 V significantly increase the capacity of the cell. In addition, as the cells were cycled to 0.00 V, the capacity measured by Nysteen could also be partially caused by Li-plating. It is also possible that the lower specific current (50 mAg^{-1}) used by Nysteen might increase the capacity of the cell. Moreover, as seen in Figure 4.7b, the carbon coated and milled SiO_2 (SM-35CB-EC/L) had a capacity closer to that reported by Nysteen. Thus, it is possible that the large difference observed in this work and that of Nysteen, is caused by differences in processing, leading to SiO_2 with different size distribution.

Effect of milling on electrochemical properties

Milling of the SiO_2 appears to significantly improve the capacity of the cells, which is in agreement with the work done on milling of SiO_2 by Chang et al [8]. Figure 4.7, demonstrates that this is the case both for pristine SiO_2 and carbon coated SiO_2.

The origin of this effect could be two fold. Lepoivre et al. have hypothesized the insulating nature of SiO_2 could limit reactions with Li^+ beyond a depth of 45/50 nm [70]. If this is the case, the increase in observed surface area of the milled frustules (Figure 4.4) will significantly increase the volume of SiO_2 that may react with Li^+. Second, a reduction of size might hamper the nonconductive nature of SiO_2, by supplying more surface area that can form contact points to CB. Thus, electrons are better supplied to the SiO_2 particles. This is supported by the SEM micrographs of the cross-sections (Figure 4.23a and Figure 4.23b), which indicate that electrodes with milled SiO_2 is more densely packet, allowing for more points of contact between SiO_2 and CB. From these micrographs it is also evident that the ball milling of the slurry was unable to reduce the size sufficiently, as large cavities can be observed in the electrode with unmilled SiO_2. Therefore, pre-milling of the SiO_2 appears to be necessary.

Effect of conductive additives

Three different sets of conductive additives were explored, 25 wt% CB, 35 wt% CB and 35 wt% (50:50 wt%) CB:CNT. As demonstrated in Figure 4.7e, the composition of the different conductive additives had little influence on capacity of the cells. As the variation in conductive additives appeared to have limited effect on the system, the phase 2 standard for conductive additives was set to 35 wt% CB. CNT was no longer considered as a conductive additive in phase 2, due to the limited benefits and the high material cost.

Electrolyte composition

The effect of electrolyte composition only appeared to be of significance in cells with milled SiO_2. Moreover, the addition of FEC and VC to the electrolyte appeared to affect cells with pristine SiO_2 and carbon coated SiO_2 differently. As cells with pristine SiO_2 experienced an increase in capacity with the FEC electrolyte, while the opposites was observed in carbon coated SiO_2 (Figure 4.7).

This observation could be explained by the increase in surface area of the milled SiO_2,

making the electrode more sensitive to SEI formation. That pristine SiO_2 and carbon coated SiO_2 exhibit different responses to the electrolyte composition, could potentially be cause by the different surface chemistry of carbon and SiO_2. However, as limited literature is available on this topic and that these observations are only based on one set of cells, it is difficult to draw any decisive conclusion based on these data.

5.3.2 Options for improving the capacity

Due to the low capacity reported in section 5.3.2, two approaches were explored to improve the capacity. First, SiO_2/Si composites were prepared, to explore if the high capacity of Si and good cycling stability of SiO_2 could be combined. Second, an electrochemical reduction program was applied. This, to determine if holding the cells at low potentials could improve the conversion rate of SiO_2 to Si.

5.3.2.1 SiO_2/Si composites

As demonstrated in Figure 4.8, all cells with Si showed a high initial capacity. However, the cycling stability of the cells was poor and the the capacity of all cells quickly faded to levels comparable to that of cells with SiO_2 as the main active material (Figure 4.7).

The poor cycling stability of the composite anodes indicates that the Si and SiO_2 used in this work has incompatible operation parameters. The the cut-off potential used, 0.01 V and 2.00 V, might lead to extensive lithiation and volume expansion of the Si. Therefore, it is possible that the large size of the SiO_2 and Si particles limited the ability of SiO_2 to buffer the expansion of Si. This is supportet by the fact that composites of Si and SiO_2 have been successfully demonstrated in the literature with similar cut-off potentials, but smaller SiO_2 and Si particles [78]. In these case, the composites were made by nano Si/SiO_2-particles. Based on these observations, SiO_2/Si composites were abandoned as an option for improving the capacity of the SiO_2 anodes.

5.3.2.2 Electrochemical reduction

Introducing an electrochemical reduction step by holding the cells at 2 mV for 48 h in the second cycle, significantly improved the capacity of both the carbon coated SiO_2 and the pristine SiO_2. Moreover, the capacity increase over the following cycles in PM-35CB-EC/H48 indicate a high level of conversion SiO_2 to Si, and subsequent lithiation of Si.

This is further supported by the differential capacity curves in Figure 4.10c, showing peak formation in PM-35CB-EC/H48 after the hold step.

By comparing the peak potential in the differential capacity plot of PM-35CB-EC/H48 and the Si-anode in Table 4.6, it can be seen that the peaks of the PM-35CB-EC/H48 cell is the same as the Si cell, only shifted by a potential of 0.05 - 0.06 V. This suggests that the peaks seen in Figure 4.10d is cause by lithiation/delithiation of Si. As the anodic and cathodic peaks are shifted to higher and lower potentials respectively, the shift is most likely caused by a significant overpotential in the electrode. This is likely caused by a rather poor conductivity of the electrode matrix. This hypothesis is further supported by the work of Lepoivre et al., which observed peak formation in differential capacity plots at similar potentials after electrochemical reduction of SiO_2 nanoparticles [70].

5.3.3 Summary of initial screening

Based on the significant increase in capacity observed after the electrochemical reduction step, electrochemical reduction of SiO_2 was further studied in phase 2, and will be discussed in more detail in section 5.4.1. Moreover, based on the observations in this section, only milled SiO_2 was further tested. To limit the number parameters in phase 2, only sucrose was used as carbon precursor. This, due to the higher amount of external area in sucrose coated SiO_2, compared to cornstarch coated SiO_2.

5.4 Electrochemical reduction as a performance enhancing technique

5.4.1 Increase in capacity by electrochemical reduction

The improvement in capacity by electrochemical reduction was confirmed by the additional testing of two cells for each material system, with the average capacity presented in Figure 4.13. In addition to the gain in capacity observed under the electrochemical reduction step, the cells in Figure 4.13 experienced a significant gain in the capacity over the subsequent cycles (cycle 3 - cycle 50) (Table 4.7). This was especially prevalent in cells with pristine SiO_2. This increase in capacity with cycle number could be explained by the formation products of the conversion reaction of SiO_2 (Li_2O, Li_4SiO_4 and $Li_2Si_2O_5$), improving the ionic conductivity of the electrode. Moreover, it is also possible

that partially lithiated SiO_2 (Li-SiO_2) improves the electrical conductivity of the anodes by reducing the bandgap of SiO_2, as proposed by Zhang et al. [95]. The combination of improved ionic conductivity and electrical conductivity might increase the volume of SiO_2 active towards lithiation.

The total capacity increase by electrochemical reduction in this work, exceeds that reported by similar cases in the literature. Lapoivre et al. achieved a capacity of only 400 $mAhg^{-1}$, after subjecting 500 nm SiO_2 particles to a 250 h hold step at 2 mV [70]. They attributed the low capacity to the insulating nature of SiO_2, limiting Li^+ ability to react with SiO_2 beyond a depth of 45-50 nm. That SiO_2 from diatom frustules achieved a capacity far exceeding that of 500 nm SiO_2 particles, may be attributed to the porous nature of the frustules observed in the SEM micrographs, limiting the amount of bulk SiO_2 further than 50 nm away from the surface.

The origin of the capacity increase observed in both the electrochemical reduction step and subsequent cycles, can be attributed to the conversion of SiO_2 to Si by the proposed reactions 2.22a-2.22c. As elaborated on in section 5.3.2.2, this hypothesis is supported by the emerging peaks in the differential capacity plots corresponding to the lithiation potential of Si. These peaks were also observed in differential capacity plots of cells in phase 2 (Figure 4.15). In addition, the hypothesis is supported by the average CE of the initial cycles (Figure 4.14) of cells in phase 2 being far below the CE of the carbon dummy cells (Table 4.4). Thus, it is reasonable to believe that a significant fraction of ICL in the first cycles is caused by the irreversible conversion of SiO_2 to Si by the reaction 2.22a-2.22c, not by SEI formation. Which of the reaction contribute to capacity increase will be further discussed in section 5.4.3.

The existence of two peaks in both the anodic and cathodic direction may be attributed to the different lithiation potentials of Li_xSi phases proposed by Ogata et al. [52]. However, which Li_xSi phases the lithiation potentials corresponds to is considered to be beyond the scope of this work.

5.4.2 Cycling stability and rate performance

The cells subjected to electrochemical reduction also exhibit excellent cycling stability, with a capacity retention well above 100 % at cycle 50, relative to cycle 1. This can most likely be attributed to the formation products (Li_2O, Li_4SiO_4 and $Li_2Si_2O_5$) by the conversion of SiO_2 to Si (reaction 2.22a-2.22c), buffering the volume expansion of Si. This is supported by the SEM images of the electrode surface after cycling, which show limited

crack formation in the electrodes compared to that experienced in Si-anodes [120]. This theory is also supported by similar reporting in the literature [77, 78, 10, 79].

The cells also showed good rate capability up to 1000 mAg^{-1}, which is of importance to the power density (equation 2.10). All cells had a capacity retention above 80 % at 1000 mAg^{-1}, exceeding that reported in the literature for similar specific current [15, 85, 89].

The good rate capability experienced up to 1000 mAg^{-1} might be caused by the decreasing band gap of SiO_2 with lithiation, improving the electrical conductivity of the electrode, as proposed by Zhang et al. [95]. In addition, the formation products of reactions 2.22a-2.22c, such as Li_4SiO_4 and $Li_2Si_2O_5$, are proposed to increase the diffusivity of Li^+ in the electrode, which could benefite the rate performance [96, 8]. That the conductivity of the electrode is improved by cycling is supported by the EIS data, as R_{ct} of all cells is reduced from cycle 3 to cycle 10. Moreover, the differential capacity data in Figure 4.15 supports this, at the onsetpotential of peak formation in the cathodic direction, i.e. lithiation, shifts to higher potentials with cycling. However, it should also be assumed that better impregnating of the electrolyte into the porous structure of the materials contributes to improve the impedance of the cell. This can be seen by the increase in capacitance with cycle number (Table 4.10), which is proportional to the electrochemical active area of the electrode.

The low capacity experienced by all cells at 2000 mAg^{-1} could be caused by an overpotential, resulting either by limited availability of Li^+ species around the active material, or by the inability of the electrode to consume Li^+ species at the rate at which electrons are supplied. A reasonable rate performance of SiO_2 have been demonstrated at 2000 mAg^{-1} by Meng et al. [15]. However, in this case graphene was a conductive additive. Thus, it is possible that better conductive additives, such as CNT, might improve the rate performance at high specific currents.

5.4.3 Identifying the lithiation mechanism of SiO_2

In an effort to identify the lithiation mechanism of SiO_2, a model was developed based on previous work by Lepoivre et al. [70]. In this model, the resulting capacity gain (Q_G) caused by a given ICL ($\frac{Q_G}{ICL}$-ratio) for the reactions 2.22a-2.22c, is used to indicate which of the three reactions contribution to the capacity gain in a SiO_2 cell.

This is achieved by plotting the theoretical $\frac{Q_G}{ICL}$-ratio of the aforementioned reactions with the experimental $\frac{Q_G}{ICL}$-ratio of different cells for a given cycle range. If one assume; (1) no SEI formation, (2) that all the Si is lithiated and (3) that no Li^+ is stored in

the anode in-between cycles, this plot can be used to estimate the reaction mechanisms contributing to the capacity gain of a cell. However, as not all Si can be expected to be lithiated and SEI could form in each cycle, the model cannot be use to exclude any reaction with a higher $\frac{Q_G}{ICL}$-ratio than reported experimentally for a given cycle. However, any experimental $\frac{Q_G}{ICL}$-ratio higher than the theoretical limit given by any of the proposed reactions 2.22a-2.22c, must imply at least some contribution from a reactions with higher $\frac{Q_G}{ICL}$-ratio.

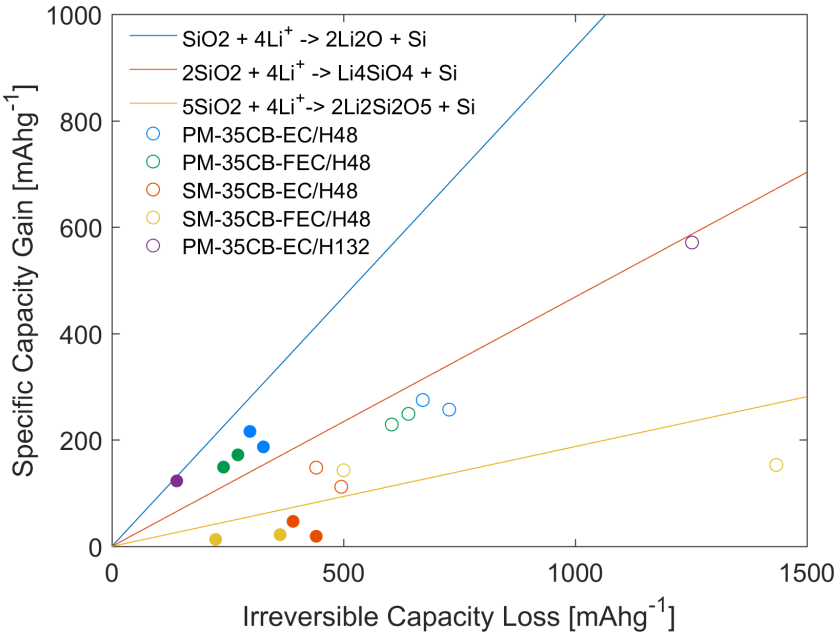

Figure 5.1: Increase in specific capacity gain (Q_G) as a function of ICL. The three lines (yellow, red and blue) show the theoretical capacity gain as a function of ICL for the three lithiation mechanisms of SiO_2 (reactions 2.22a-2.22c). The scatter dots show the increase in capacity as a function of the ICL over the electrochemical reduction step, cycle 2 - cycle 3 (hollow) and over cycle 3 - cycle 50 (filled).

In Figure 5.1, the $\frac{Q_G}{ICL}$-ratio profile of the reactions (I-III) are plotted with the experimental data from phase 2. The experimental $\frac{Q_G}{ICL}$-ratio was calculated for two cycle ranges, cycle 2 - cycle 3 and cycle 3 - cycle 50, representing the capacity increase over the electrochemical reduction step and regular cycling. Cycle 1 was excluded, as a large fraction of the ICL loss in this cycle may be assumed to be caused by SEI formation. To further test the validity of the model, a PM-35CB-EC cell was assembled and subjected to a 132 h hold step.

Lithiation mechanism over electrochemical reduction step

In Figure 5.1, the $\frac{Q_G}{ICL}$-ratio over the electrochemical reduction step (hollow dots) appears to be slightly below the $\frac{Q_G}{ICL}$-ratio of reaction 2.22b for all cells. That the experimental $\frac{Q_G}{ICL}$-ratio is slightly below the theoretical value, is reasonable, as not all the assumptions of the model can be met experimentally. Based on this observation it is reasonable to believe that the capacity gain during the electrochemical reduction step is mainly driven by reaction 2.22b. However, some contribution from reaction 2.22a , 2.22c cannot be excluded.

Lithiation mechanism during regular cycling

In the case of regular cycling, the $\frac{Q_G}{ICL}$-ratio of the cells with pristine SiO_2 is above the theoretical limit of reaction 2.22a and 2.22b, implying a significant contribution from reaction 2.22c to this capacity gain. However again, contributions from 2.22a, 2.22b cannot be excluded. In the case of cells with carbon coated SiO_2, virtually no capacity increase is seen in cycle 3-50. Thus, it is likely that most of the ICL is caused by SEI formation. This is also supported by SEM micrographs of the electrode surface after cycling (Figure 4.22), showing decompositions products on the surface.

Origin of the difference in the lithiation mechanism

The difference in $\frac{Q_G}{ICL}$-ratio experienced during the electrochemical reduction step and the subsequent cycles, could be caused by SEI formation during the hold step, as SEI formation will reduce the $\frac{Q_G}{ICL}$-ratio. In this case, there would be no true difference in the reaction mechanism. However, it could also be effected by the rate of conversion by the reactions 2.22a-2.22c, at different potentials. Zhang et al. have proposed that reaction 2.22c takes place first in the reduction process [95]. Thus, it is possible that a larger contribution from 2.22c is experienced from cycle 3 - cycle 50, because the relative contribution from 2.22c is larger at higher potentials.

No difference was observed in the $\frac{Q_G}{ICL}$-ratio of cells with the same electrode, but different electrolyte composition. Therefore, it is unlikely that electrolyte composition have a significant effect on the lithiation mechanism of SiO_2.

5.4.4 Effect of carbon coating

As noted in section 5.4.1, distinct differences can be seen in the capacity of cells with pristine SiO_2 and carbon coated SiO_2. From Figure 4.13, two main trends can be observed. The capacity of cells with carbon coated SiO_2 have initially higher capacity than cells with pristine SiO_2. In addition, the capacity of cell with carbon coated SiO_2 is fairly stable through cycling. In contrast, the average capacity of cells with pristine SiO_2 increase with cycle number, before stabilize towards cycle 50. The presence of FEC and VC appears to impact cells with pristine SiO_2 and carbon coated SiO_2 differently. However, this topic will be addressed in the section 5.4.5.

The behavior described in the aforementioned paragraph could be caused by two mechanisms. In the first mechanism, the initially higher capacity of cells with carbon coated SiO_2 is mainly caused by the capacity contribution from Li^+ intercalation into the amorphous carbon coating. In this case, the limited capacity increase in capacity during the electrochemical reduction step and the subsequent cycles, may be caused by an overpotential created by extensive SEI formation on th carbon coated SiO_2 particles. This overpotential could then limiting the conversion reactions of SiO_2 to Si. A possible second mechanism, is that the high initial capacity of carbon coated SiO_2 is caused by a higher initial conversion of SiO_2 to Si, facilitated by the carbon coating ability to distributing electrons efficiency around the SiO_2 particles. In this case, the limited increase in capacity observed in the subsequent cycles may be caused by the limiting reactivity of SiO_2 beyond a certain penetration depth, as hypothesized by Lepoivre et al. [70](i.e. most of the available SiO_2 is already converted after the first cycle). A combination of the two mechanisms is also possible.

The SEM micrographs of the electrode surface and the FIB cross-section in Figure 4.22 and Figure 4.23e, 4.23f respectively, show extensive film formation on the carbon coated SiO_2 particles compared to the pristine SiO_2 particles. The presence of such film formation could create an overpotential, which would support the first mechanism. If the film formation causes an overpotential, this should be observable in both the differential capacity plot and EIS data. However, no significant overpotential is observable in the differential capacity plot of either cycle 1, cycle 3 or cycle 50 in Figure 4.16a, 4.16b, 4.16c respectively. In these figures, peaks can be seen to form on roughly the same potentials, implying that there is no significant overpotential in the electrode. This observation is further supported by the EIS data in Figure 4.19, where R_3 can be assumed to be representative of R_{ct}. In this figure, R_{ct} of SM-35CB-EC/H48 is lower than PM-35CB-EC/H48 at all cycles, and at the 10th cycle, SM-35CB-EC/H48 has the lowest R_{ct} of all

cells. Thus, it is likely that the carbon coating results in a thicker SEI, but that the SEI layer exhibit good Li^+ conductivity, limiting the overpotential caused by the SEI.

If the observations made in Figure 4.13 are caused by the second mechanism, the capacity in terms of m_{SiO_2}, of the cells with carbon coated SiO_2 should be higher in the first cycles, relative to the cell with pristine SiO_2. Moreover, if the reactivity of SiO_2 is limited to a certain depth, there should exist a fixed volume of SiO_2 available for conversion in the anode. Thus, there should be an upper capacity limit to all cells, that the cells converge to with increasing cycle number.

In an attempt to explore if this is the case, the capacity of cells in phase 2 (Figure 4.13) was recalculated. This was done by subtracting the average capacity contribution pr cycle of all sources of carbon, and then normalize the capacity in terms of m_{SiO_2} [1]. It should be noted that this type of calculation is inherently uncertain. The standard deviation of the average capacity of the carbon cells is quite large. Thus, there might be significant differences in the capacity contribution from carbon in each cell. It is also uncertain if the average capacity of carbon is the same in a pure carbon cell and in a cell with SiO_2. Finally, the estimated capacity contribution of carbon in each cell relies heavily on the carbon content of the carbon coated SiO_2. Thus, small uncertainness in the TGA data might lead to large uncertainties in this data.

[1] In Figure 4.13, the specific capacity was calculated on the basis of active material, which is the standard in the literature. The amount of active material is the same in all cell, but as the cells with carbon coated SiO_2 contain 46.5 wt% carbon, the wt % SiO_2 is lower in these cells

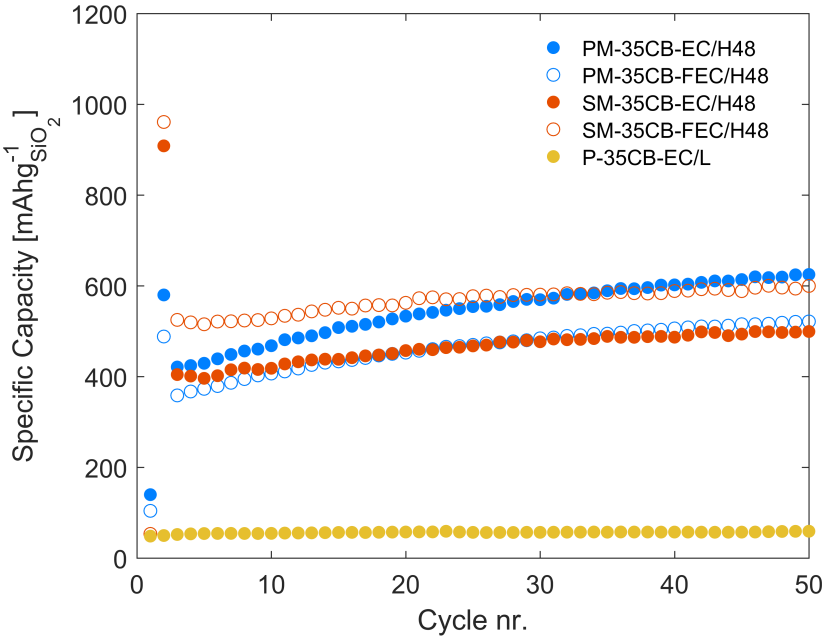

Figure 5.2: Recalculated average capacity of cells in phase 2. Average capacity contribution pr. cycle from carbon additives is subtracted and the capacity normalized to m_{SiO_2}.

The recalculated average capacities are presented in Figure 5.2. The figure suggests that a large fraction of the capacity in all cells originates from the SiO_2, with the highest estimated capacity originating from SiO_2 at 625 $mAhg^{-1}$ for PM-35CB-EC/H48. The figure also suggests that a significant part of the capacity of the carbon coated SiO_2 originate from SiO_2, not the pyrolysed carbon. The capacity of PM-35CB-EC/H48 and SM-35CB-FEC/H48 also appears to converge with cycling. However, for this to proven, more cycles have to be conducted.

The higher initial capacity of SM-35CB-FEC/H38 compared to PM-35CB-EC/48, also suggests that the carbon coating contributes to increase the initial conversion of SiO_2 to Si. This observation is further supported by the plot of the specific ICL, presented in Figure 5.3. In this plot, the average ICL pr cycle of the different carbon additives have been subtracted and the ICL re-normalized to m_{SiO_2}. Thus, the data in the figure can be viewed as an estimate of the ICL caused by conversion of SiO_2 to Si.

The figure indicates that the specific ICL of SM-35CB-FEC/H48 is significantly higher than the other cells in both the 1st and the 2nd cycle. This suggests that a larger amount of SiO_2 is converted to Si over the two first cycles in SM-35CB-FEC/H48 compared to the other cells. This observation is also supported by the current profile of the electrochemical reduction step in Figure 4.12. Initially, a larger current can be seen going through cells

with carbon coated SiO_2 compared to the cells with pristine SiO_2.

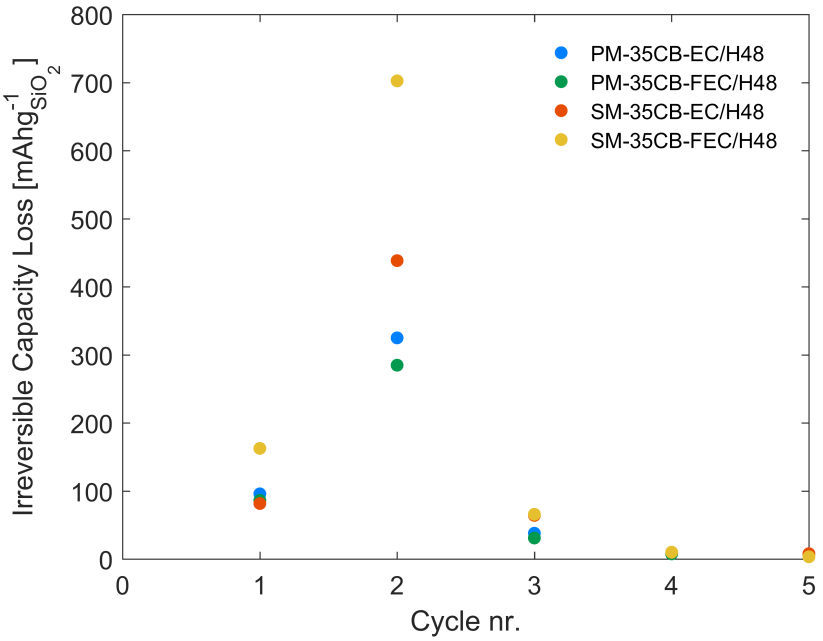

Figure 5.3: Average specific ICL of cells in phase 2. Average ICL pr. cycle from carbon additives is subtracted and the ICL normalized to m_{SiO_2}.

Based on the observation in this section, it is likely that carbon coating the SiO_2 result in a faster conversion of SiO_2 to Si, relative to pristine SiO_2. This is probably caused by the carbon coatings ability to distribute electrons around the entire SiO_2 particle, thereby counteracting the limited conductivity of the SiO_2. This observation is also in agreement with the improved capacity of carbon coated SiO_2 relative to pristine SiO_2 reported in the litterture [13, 69, 98, 88].

5.4.5 Effect of electrolyte composition

As noted in the previous section, the electrolyte additives, FEC and VC, appears to affect the capacity of carbon coated SiO_2 and pristine SiO_2 differently. In addition, the additives were found to affect the morphology and chemistry of the SEI layer, the extent of SEI formation in the bulk of the electrodes and the impedance of the electrodes.

In the differential capacity plots of the first cycle of cells in phase 2 (Figure 4.16a), the initial decomposition of FEC and VC at $\sim$ 1.5 V in PM-35CB-EC/H48, SM-35CB-EC/H48, appears to limit peak formation at 0.8 V relative to cells with the EC electrolyte

(PM-35CB-EC/H48, SM-35CB-EC/H48). This suggests that the initial decomposition of FEC and VC, limits decomposition of EC at 0.8 V, and thereby alters the chemistry of the SEI layer.

This is further supported by the difference in SEI morphology observed in the SEM micrographs of the electrodes cycled in electrolytes in the two electrolytes (Figure 4.21 for cells with pristine SiO_2 and Figure 4.22 for cells with carbon coated SiO_2). Moreover, SEM micrographs of the FIB cross-sections show that cells cycled in FEC and VC appear to have less SEI formation in the bulk of the electrode. This was observed in both cells with pristine SiO_2 and carbon coated SiO_2. Finally, EDX mapping of the electrode surface after cycling resulted in a higher EDX signal of fluorine (Table 4.11) on electrodes cycled in FEC and VC. It should be noted quantifying chemical composition by EDX is an inherently uncertain technique. However, as the same working distance, acceleration voltage and electron current were used in all EDX mappings, and that similar results are reported in the literature, should justify the use of the EDX data as indicative of the chemical composition of the SEI layer [121].

Effect on electrode performance

In Figure 4.13, FEC and VC appears to increase the capacity of carbon coated SiO_2, while hampering the capacity of pristine SiO_2. This behaviour could potentially be caused by the aforementioned differences in the SEI formed on carbon coated SiO_2 and pristine SiO_2.

The SEM micrograph in Figure 4.21 showed limited SEI formation on pristine SiO_2, while the SEM micrograph of the carbon coated SiO_2 (Figure 4.22) indicated extensive SEI formation. Thus, a possible hypothesis is that the first cycle decomposition of FEC and VC affect the two materials systems differently. In the case of pristine SiO_2, the initial decomposition of FEC and VC might increase the thickness of the SEI layer compared to electrolytes without the additive. In the case of carbon coated SiO_2, the initial decomposition of FEC and VC might limit further extensive decomposition of EC, which is found to be the case in the literature for Si-anodes [62].

However, limited evidence supporting this hypothesis can be found in this work. The SEM micrographs of the electrode surfaces showed neglectable differences in film thickness when comparing cells with the same electrode, but cycled in different electrolytes (PM-35CB-EC/H48 vs PM-35CB-FEC/H48 and SM-35CB-EC/H48 vs SM-35CB-FEC/H48). In the FIB cross-section, FEC and VC was found to reduce the bulk film formation in both cells with pristine SiO_2 and carbon coated SiO_2, indicating that the additives have

the same effect on both pristine SiO_2 and carbon coated SiO_2. Moreover, the differential capacity plots show no sign of overpotential when comparing cell with and without FEC and VC.

By comparing the Nyquist plots (Figure 4.19) of cells with pristine SiO_2 (PM-35CB-EC/H48 and PM-35CB-FEC/H48), the presence of FEC an VC appears to dramatically reduce both R_{SEI} and R_{CT}. This could be explained by the hypothesis put forth by Jaumann et al., which proposed that the addition of FEC increase the amount of LiF crystals in the SEI layer, creating a more porous SEI than better conduct Li^+ [58]. This might be the case, as an increase in fluorine was detected by EDX for cells cycled in FEC. However, there is no way of knowing if the fluorine actually was in the form of LiF crystals. It should also be noted that the EIS data only were measured once. Thus, it is possible that the large variation in impedance is a results experimental uncertainties. Unfortunate, limited time prevented the collection of experimental data on Nyquist plot of SM-35CB-FEC/H48. Therefore, it was not possible to explore if FEC and VC affects R_{SEI} and R_{CT} differently in cells with pristine SiO_2 and carbon coated SiO_2.

Based on this discussion it is evident that the electrolyte additives, FEC and VC, effect the chemistry and morphology of the SEI. Moreover, this effect appears to translated into cell performance, as cells with the same electrode, but different electrolyte compositions, exhibit different capacities and impedance. However, the results of this work failed to identify the underlying mechanism.

5.5 SiO_2 from diatom frustules as an anode material

To be a viable option as an anode material, the diatom frustules must be a competitive alternative as a SiO_2 feedstock, and in the long run, be a viable option for replacing carbon anodes.

Compared to the reported capacities of SiO_2 anodes in the literature (Table 2.6), the highest average capacity in this work, 723 $mAhg^{-1}$ after 50 cycles (PM-35CB-EC/H48), is among the highest reported of SiO_2 anodes. In addition, most of the publications in Table 2.6 with higher reported capacities use cut-off potentials above 2.00 V, which unrealistic in terms of full cell applications [85, 14, 12]. However, this work has also demonstrated some serous limitations related to the use of SiO_2 from diatom frustules.

The need for an electrochemical reduction step to achieve sufficient capacities is a major drawback, as it might impose huge costs on potentially commercial applications. Thus,

the need for such a reduction step rises the question of whether or not large scale bulk reduction of diatom frustules by magnesiothermic reduction, as demonstrated by Campbell et al., is a better approach [74]. This might be the case, but magensiothermic reduction also have serious downs sides, such as safety consideration and the need for an air free environment during reduction. Moreover, further optimization of milling, carbon coatings and electrolyte composition might make the electrochemical reduction step obsolete. Therefore, based on the discussion in this section, there seems to be little reason for discarding diatom frustules as an promising SiO_2 feedstock.

The high capacity, cycling stability and rate capability demonstrated in this work, also makes SiO_2 from diatom frustules an interesting option for replacement graphite. However, this work has also demonstrated limitations related to the use of SiO_2 in full cells.

The voltage profile of SiO_2 in this work (Figure 4.11) is considerable more sloping than the voltage profile of graphite anodes. In accordance with equation 2.8 (energy density of a battery), this imply that the improved capacity of SiO_2 anodes do not result in a proportional increase in energy density. Another significant disadvantage is the low CE of the first cycles observed in Figure 4.14. Even though the low CE is related to the capacity increase in a half cell, most full cells are cathode limited, implying that the capacity increase of the anode cannot be exploited in a full cells configuration. Moreover, the low CE of the first cycles might deplete the limited Li^+ available in a full cell, and thereby reduce the capacity. Thus, the capacity increase of SiO_2 anodes have to be achieved before the anode is assembled in to a full cell, and from this point out, any increase in capacity should be limited to prevent consumption of Li^+.

Finally, it should also be noted that the results in this work was achieved by electrodes with a fairly low loading and relative large amounts of conductive additives. Thus, it is yet to be proven if the same results can be achieved with a loading relevant for industrial applications.

Chapter 6: Conclusion

The primary goal of this work was to investigate the potential of SiO_2 from diatom frustules as a potentially high performance, low cost and environmentally friendly anode material. Initial trails revealed that milling the SiO_2 is necessary to achieve densely packed electrodes. In addition, the highest achieved capacity, 409 $mAhg^{-1}$ after 100 cycles, was found insufficient compared to the capacities of SiO_2 already reported in the literature.

In an attempt to increase the capacity, both SiO_2/Si composites and electrochemical reduction of the SiO_2 were explored as capacity enhancing techniques. The SiO_2/Si composites experienced an initial increase in capacity proportional to the Si content. However, the capacity quickly faded, and after 100 cycles the capacity of all composites had reduced to levels equivalent to that of pure SiO_2 cells. The rapid fade in capacity can be attributed to the incompatible operation parameters of SiO_2 and Si, resulting in massive volume expansion of Si. Electrochemical reduction was found to significantly increase the capacity of the SiO_2 cell.

Further investigation of the electrochemical reduction confirmed that the technique was successful in achieving high capacity SiO_2 anodes, with excellent cycling stability at practical operating conditions (200 mAg^{-1}, 0.01 V-2.00 V). In addition, the anode showed good rate performance up to 1000 mAg^{-1}. The best performing material system, consisting of pristine SiO_2, achieved a final average capacity of 723 $mAhg^{-1}$. Of this, the capacity contribution of SiO_2 was estimated to 625 $mAhg^{-1}$. Although electrodes with pristine SiO_2 had a higher final capacity, carbon coated SiO_2 had a higher initial capacity. This can most likely be attributed to the carbon coating facilitating an even distribution of electrons around the SiO_2 particles in the electrode, increasing the amount of active SiO_2 in the electrode.

Evaluating the gain in capacity as a function of the irreversible capacity loss, revealed that the increase in capacity under the electrochemical reduction step was most likely caused by the conversion reaction, $2\,SiO_2 + 4\,Li^+ + 4\,e^- \rightarrow Li_4SiO_4 + Si$. However, the model

suggests that the capacity gain over regular cycling shows significant contribution from the conversion reaction, $SiO_2 + 4\,Li^+ + 4\,e^- \rightarrow 2Li_2O + Si$, which has a higher theoretical capacity. Therefore, it is reasonable to believe that the capacity might be significantly improved if processes that increase the conversion of SiO_2 to Si by the latter reaction are identified.

With a capacity 723 $mAhg^{-1}$ after 50 cycles, the SiO_2 from frustules resulted in some of the highest reported capacities found in the literature on SiO_2 anodes. In addition to the high capacity, the cycling stability and good rate capability contributes to counterbalance the drawbacks of a sloping voltage profile. Moreover, this was achieved by cycling conducted at relatively high specific currents and over a practical voltage window. Thus, SiO_2 from diatom frustules appears to be a potential high performance, low cost and environmentally friendly anode material. However, for wide spread applications of the SiO_2 to take place, the performance must be confirmed at higher loadings, and the drawbacks of the electrochemical reduction process and the high ICL must be addressed.

Chapter 7: Further work

Aim of this chapter

This chapter on further work is divided into two main section. The first section will provide suggestions for how some of the challenges identified in this work might be resolved, and highlight some interesting observations made that could not be pursued in this report. The second section has a broader focus, and will attempt to address how the main challenges of using SiO_2 from diatom frustules in full cell applications might be solved.

Addressing challenges identified in this work

Improved understanding of lithiation mechanism of SiO_2

For SiO_2 anodes to reach the theoretical capacity of 1673 $mAhg^{-1}$, a better understanding of the multiple lithiation mechanisms of SiO_2 (reaction 2.22) and the relative contribution from the different lithiation mechanisms is needed. It is also important to gain insight into how cycling parameters, such as; SiO_2 particle size, the chemistry of carbon coatings and cycling conditions might affect these reaction mechanisms.

X-ray photoelectron spectroscopy (XPS) is a powerful technique for identifying the chemical composition of a sample. XPS can also be used to determine the relative amount of each the different reaction products. A detailed XPS analysis of the formation products present in cells with different carbon coating, electrolyte composition and cells which are cycled at different rates and cut off potentials, might contribute to improve the understanding of the reaction mechanisms 2.22a-2.22c, and how to optimize towards reaction 2.22c. If this can be achieved, the capacity of SiO_2 might increase towards the theoretical capacity of 1673 $mAhg^{-1}$.

Optimization of carbon coating

The results of this work suggest that carbon coating the SiO_2 particles is important in ensuring a fast and uniform conversion of SiO_2 to Si. However, as the theoretical capacity of the carbon coating is lower than SiO_2, and that the carbon surface is prone so extensive SEI formation, the amount of carbon should be minimized. Thus, a study on the resulting properties of different carbon coatings, and subsequent optimization of the carbon content might significantly improve the capacity of the cell

Optimization of milling

Milling was one of the few parameters in the initial screening of this work that resulted in a significant increase in capacity. Furthermore, if the accessible volume of SiO_2 indeed is limited by the insulating nature of SiO_2, further milling might significantly improve the capacity by increasing the surface area. In addition, Guo et al. hypothesized that the size of the SiO_2 particles might affect which of the conversion reactions 2.22a-2.22c are most prevalent [11]. Thus, it is possible that detailed understanding on the effect milling might be key in approaching the theoretical capacity of SiO_2 at 1673 $mAhg^{-1}$.

Proving long time cycling stability

The cycling stability of cell in this work was superb. However, this stability was only proven up to 100 cycles. Even though there is little reason to believe that cycle stability of will fade with increasing cycle number, this is yet to be proven. Thereby, efforts should be made to prove the cycle stability of the cell up to the industry standard for cycle life time at 1000 cycles.

Optimization of electrolyte composition

This work demonstrated that electrolyte additives such as FEC and VC have an impact on the performance of electrode. Even though this work was not able to identify the underlying mechanism causing these differences, further exploring the effect of electrolyte composition on the performance of SiO_2 anodes might prove fruitful. This might especially be the case, if carbon coating SiO_2 is deemed necessary, as this work have shown that FEC and VC significantly improved the performance of carbon coated SiO_2. Thus, further exploration of electrolyte solvents, such as: DMC, EMS and PC and other

electrolyte additives, such as NO_3^-, might result in further improvements of the electrode performance.

Challenges of SiO_2 in full cell applications

As elaborated on in the previous chapter, two fundamental challenges have to be overcome for SiO_2 from diatom frustules to become a viable option as anode material in full cells. First, a processes have to be developed for fast conversion of SiO_2 to Si. Second, after this conversion has taken place, the capacity must be stabilized in order to limit Li^+ consumption in full cells configurations.

As proved in this work, the first challenge may be resolved by electrochemical reduction. However, this technique has limitations related to cost and scalability. Further size reduction of the SiO_2 might render the electrochemical reduction step unnecessary. If primitive and low cost size reduction methods, such as ball milling, can further reduced the SiO_2 to 100 nm - 200 nm, the surface area of the SiO_2 will increase significantly. This will increase the volume of SiO_2 that is readily accessible for lithiation. Thus, it is possible that the electrochemical reduction step will be unnecessary.

As previously noted the, capacity gain with cycle number in a full cell must be limited to prevent consumption of Li^+. This problem might be eliminated by investigation techniques for ensuring close to 100 % conversion of SiO_2 before full cell assembly. This work showed that the increase in capacity with cycle number was significantly lower for carbon coated SiO_2 compared to pristine SiO_2. Therefore, it is possible that a more in-depth study on effect of carbon coating, electrolyte composition and the resulting SEI might identify processes that limit the capacity gain with cycle number. In addition, it is possible that this problem can be circumvent by monitoring the CE and limit the charging/discharging. However, this depend on whether or not the irreversible conversion reactions of SiO_2 to Si are taking place over the entire charging cycle, or if they only take place at the limiting potentials, i.e. only at low potentials.

Bibliography

[1] Perumal Raman et al. "Opportunities and challenges in setting up solar photo voltaic based micro grids for electrification in rural areas of India". In: *Renewable and Sustainable Energy Reviews* 16.5 (2012), pp. 3320–3325.

[2] Charles Kirubi et al. "Community-Based Electric Micro-Grids Can Contribute to Rural Development: Evidence from Kenya". In: *World Development* 37.7 (2009), pp. 1208–1221.

[3] Bruce Dunn et al. "Electrical energy storage for the grid: a battery of choices". In: *Science* 334.6058 (2011), pp. 928–935.

[4] David L. Wood et al. "Prospects for reducing the processing cost of lithium ion batteries". In: *Journal of Power Sources* 275 (2015), pp. 234–242.

[5] Kirti Richa et al. "A future perspective on lithium-ion battery waste flows from electric vehicles". In: *Resources, Conservation and Recycling* 83 (2014), pp. 63–76.

[6] Matthew T. McDowell et al. "25th Anniversary Article: Understanding the Lithiation of Silicon and Other Alloying Anodes for Lithium-Ion Batteries". In: *Advanced Materials* 25.36 (2013), pp. 4966–4985.

[7] Xiuxia Zuo et al. "Silicon based lithium-ion battery anodes: A chronicle perspective review". In: *Nano Energy* 31 (2017), pp. 113–143.

[8] Won-Seok Chang et al. "Quartz (SiO2): a new energy storage anode material for Li-ion batteries". In: *Energy & Environmental Science* 5.5 (2012), p. 6895.

[9] Wei Wang et al. "Monodisperse Porous Silicon Spheres as Anode Materials for Lithium Ion Batteries". In: *Scientific Reports* 5 (2015), p. 8781.

[10] Hua-Chao Tao et al. "Double-walled core-shell structured Si@SiO2@C nanocomposite as anode for lithium-ion batteries". In: *Ionics* 20.11 (2014), pp. 1547–1552.

[11] Bingkun Guo et al. "Electrochemical reduction of nano-SiO2 in hard carbon as anode material for lithium ion batteries". In: *Electrochemistry Communications* 10.12 (2008), pp. 1876–1878.

[12] Xi Cao et al. "A three layer design with mesoporous silica encapsulated by a carbon core and shell for high energy lithium ion battery anodes". In: *J. Mater. Chem. A* 3.45 (2015), pp. 22739–22749.

[13] Chien-Wen Wang et al. "Mesoporous SiO 2/carbon hollow spheres applied towards a high rate-performance Li-battery anode". In: *Inorganic Chemistry Frontiers* 3.11 (2016), pp. 1398–1405.

[14] Nan Yan et al. "Hollow Porous SiO2 Nanocubes Towards High-performance Anodes for Lithium-ion Batteries". In: *Scientific Reports* 3 (2013).

[15] Jingke Meng et al. "Facile Fabrication of 3D SiO2@Graphene Aerogel Composites as Anode Material for Lithium Ion Batteries". In: *Electrochimica Acta* 176 (2015), pp. 1001–1009.

[16] Lars-Henrik Nysteen. "Exploring lithium ion batteries for wind powered water injection". MA thesis. NTNU, 2016.

[17] Keith Oldham et al. *Electrochemical science and technology: fundamentals and applications*. John Wiley & Sons, 2012, p. 60.

[18] Arumugam Manthiram et al. "Rechargeable Lithium–Sulfur Batteries". In: *Chemical Reviews* 114.23 (2014), pp. 11751–11787.

[19] Christian Julien et al. *Lithium Batteries: Science and Technology*. Springer, 2016, p. 32.

[20] Christian Julien et al. *Lithium Batteries,Science and Technology*. Springer, 2016, p. 49.

[21] John B. Goodenough et al. "The Li-Ion Rechargeable Battery: A Perspective". In: *Journal of the American Chemical Society* 135.4 (2013), pp. 1167–1176.

[22] Eliezer Gileadi et al. *Physical electrochemistry: fundamentals, techniques and applications*. Wiley, 2011, pp. 57–58.

[23] Richard Jow et al. *Electrolytes for lithium and lithium-ion batteries*. Vol. 58. Springer, 2014, p. 1.

[24] Shuo Zhang et al. "Advanced electrolyte/additive for lithium-ion batteries with silicon anode". In: *Current Opinion in Chemical Engineering* 13 (2016), pp. 24–35.

[25] Kang Xu. "Nonaqueous liquid electrolytes for lithium-based rechargeable batteries". In: *Chemical reviews* 104.10 (2004), pp. 4303–4418.

[26] Richard Jow et al. *Electrolytes for lithium and lithium-ion batteries*. Vol. 58. Springer, 2014, p. 15.

[27] Christian Julien et al. *Lithium Batteries: Science and Technology*. Springer, 2016, pp. 589–590.

[28] Steven E Sloop et al. "Chemical Reactivity of PF 5 and LiPF6 in Ethylene Carbonate/Dimethyl Carbonate Solutions". In: *Electrochemical and Solid-State Letters* 4.4 (2001), A42–A44.

[29] Steven Sloop et al. "The role of Li-ion battery electrolyte reactivity in performance decline and self-discharge". In: *Journal of power sources* 119 (2003), pp. 330–337.

[30] Richard Jow et al. *Electrolytes for lithium and lithium-ion batteries*. Vol. 58. Springer, 2014, p. 94.

[31] Meng Hu et al. "Recent progress in high-voltage lithium ion batteries". In: *Journal of Power Sources* 237 (2013), pp. 229–242.

[32] Christian Julien et al. *Lithium Batteries: Science and Technology*. Springer, 2016, p. 51.

[33] Pallavi Verma et al. "A review of the features and analyses of the solid electrolyte interphase in Li-ion batteries". In: *Electrochimica Acta* 55.22 (2010), pp. 6332–6341.

[34] Mark Weller et al. *Inorganic chemistry*. Oxford, 2014, p. 682.

[35] Vinodkumar Etacheri et al. "Challenges in the development of advanced Li-ion batteries: a review". In: *Energy & Environmental Science* 4.9 (2011), p. 3243.

[36] François Béguin et al. *Carbons for electrochemical energy storage and conversion systems*. CRC Press, 2010, p. 278.

[37] Jeff R Dahn et al. "Mechanisms for lithium insertion in carbonaceous materials". In: *Science* 270.5236 (1995), p. 590.

[38] François Béguin et al. *Carbons for electrochemical energy storage and conversion systems*. CRC Press, 2010, p. 280.

[39] Christian Julien et al. *Lithium Batteries,Science and Technology*. Springer, 2016, p. 355.

[40] Khalil Amine et al. "Nanostructured Anode Material for High-Power Battery System in Electric Vehicles". In: *Advanced Materials* 22.28 (2010), pp. 3052–3057.

[41] Christian Julien et al. *Lithium Batteries,Science and Technology*. Springer, 2016, p. 89.

[42] Delong Ma et al. "Si-Based Anode Materials for Li-Ion Batteries: A Mini Review". In: *Nano-Micro Letters* 6.4 (2014), pp. 347–358.

[43] Wei-Jun Zhang. "A review of the electrochemical performance of alloy anodes for lithium-ion batteries". In: *Journal of Power Sources* 196.1 (2011), pp. 13–24.

[44] Christian Julien et al. *Lithium Batteries: Science and Technology*. Springer, 2016, p. 88.

[45] Jordi Cabana et al. “Beyond Intercalation-Based Li-Ion Batteries: The State of the Art and Challenges of Electrode Materials Reacting Through Conversion Reactions”. In: *Advanced Materials* 22.35 (2010), E170–E192.

[46] Seung-Ho Yu et al. “Conversion Reaction-Based Oxide Nanomaterials for Lithium Ion Battery Anodes”. In: *Small* 12.16 (2015), pp. 2146–2172.

[47] Zhengcheng Zhang and Sheng Shui Zhang. *Rechargeable Batteries*. Springer, 2015.

[48] Christian Julien et al. *Lithium Batteries,Science and Technology*. Springer, 2016, p. 323.

[49] Nam-Soon Choi et al. “Recent Progress on Polymeric Binders for Silicon Anodes in Lithium-Ion Batteries”. In: *Journal of Electrochemical Science and Technology* 6.2 (2015), pp. 35–49.

[50] Alexandre Magasinski et al. “Toward Efficient Binders for Li-Ion Battery Si-Based Anodes: Polyacrylic Acid”. In: *ACS Applied Materials & Interfaces* 2.11 (2010), pp. 3004–3010.

[51] K. Varoon et al. “Dispersible Exfoliated Zeolite Nanosheets and Their Application as a Selective Membrane”. In: *Science* 334.6052 (2011), pp. 72–75.

[52] K. Ogata et al. “Revealing lithium–silicide phase transformations in nano-structured silicon-based lithium ion batteries via in situ NMR spectroscopy”. In: *Nature Communications* 5 (2014).

[53] LY Beaulieu et al. “Colossal reversible volume changes in lithium alloys”. In: *Electrochemical and Solid-State Letters* 4.9 (2001), A137–A140.

[54] S Xun et al. “The effects of native oxide surface layer on the electrochemical performance of Si nanoparticle-based electrodes”. In: *Journal of The Electrochemical Society* 158.12 (2011), A1260–A1266.

[55] John Wen et al. “Chemical Diffusion and in IntermediateP and hases in the Lithium-Silicon and System”. In: *JOURNAL OF SOLID STATE CHEMISTRY* 37.28 (1981), pp. 271–278.

[56] Vijay Sethuraman et al. “Analysis of electrochemical lithiation and delithiation kinetics in silicon”. In: *Journal of the Electrochemical Society* 160.2 (2013), A394–A403.

[57] Hong Li et al. “A high capacity nano Si composite anode material for lithium rechargeable batteries”. In: *Electrochemical and Solid-State Letters* 2.11 (1999), pp. 547–549.

[58] Tony Jaumann et al. “Lifetime vs. rate capability: Understanding the role of FEC and VC in high-energy Li-ion batteries with nano-silicon anodes”. In: *Energy Storage Materials* 6 (2017), pp. 26–35.

[59] Magali Gauthier et al. "Electrode–Electrolyte Interface in Li-Ion Batteries: Current Understanding and New Insights". In: *The Journal of Physical Chemistry Letters* 6.22 (2015), pp. 4653–4672.

[60] Nam-Soon Choi et al. "Effect of fluoroethylene carbonate additive on interfacial properties of silicon thin-film electrode". In: *Journal of Power Sources* 161.2 (2006), pp. 1254–1259.

[61] Libao Chen et al. "Effect of vinylene carbonate (VC) as electrolyte additive on electrochemical performance of Si film anode for lithium ion batteries". In: *Journal of Power Sources* 174.2 (2007), pp. 538–543.

[62] Hideki Nakai et al. "Investigation of the solid electrolyte interphase formed by fluoroethylene carbonate on Si electrodes". In: *Journal of The Electrochemical Society* 158.7 (2011), A798–A801.

[63] Vinodkumar Etacheri et al. "Effect of Fluoroethylene Carbonate (FEC) on the Performance and Surface Chemistry of Si-Nanowire Li-Ion Battery Anodes". In: *Langmuir* 28.1 (2012), pp. 965–976.

[64] Aude A. Hubaud et al. "Interfacial study of the role of SiO2 on Si anodes using electrochemical quartz crystal microbalance". In: *Journal of Power Sources* 282 (2015), pp. 639–644.

[65] Seong Jin An et al. "The state of understanding of the lithium-ion-battery graphite solid electrolyte interphase (SEI) and its relationship to formation cycling". In: *Carbon* 105 (2016), pp. 52–76.

[66] JS Gnanaraj et al. "The role of carbonate solvents on lithium intercalation into graphite". In: *Journal of The Electrochemical Society* 154.3 (2007), A185–A191.

[67] Bo Gao et al. "Alloy formation in nanostructured silicon". In: *Advanced Materials* 13.11 (2001), pp. 816–819.

[68] Qian Sun et al. "Lithium electrochemistry of SiO2 thin film electrode for lithium-ion batteries". In: *Applied Surface Science* 254.13 (2008), pp. 3774–3779.

[69] Xuelian Liu et al. "SiO 2 @C hollow sphere anodes for lithium-ion batteries". In: *Journal of Materials Science & Technology* 33.3 (2017), pp. 239–245.

[70] Florent Lepoivre et al. "Electrochemical Activation of Silica for Enhanced Performances of Si-Based Electrodes". In: *Journal of The Electrochemical Society* 163.13 (2016), A2791–A2796.

[71] A Hohl et al. "An interface clusters mixture model for the structure of amorphous silicon monoxide (SiO)". In: *Journal of Non-Crystalline Solids* 320.1-3 (2003), pp. 255–280.

[72] Herbert R Philipp. "Optical and bonding model for non-crystalline SiOx and SiOxNy materials". In: *Journal of Non-Crystalline Solids* 8 (1972), pp. 627–632.

[73] Tianwen Zhang et al. “Porous silicon nano-aggregate from silica fume as an anode for high-energy lithium-ion batteries”. In: *RSC Adv.* 6.36 (2016), pp. 30577–30581.

[74] Brennan Campbell et al. “Carbon-Coated, Diatomite-Derived Nanosilicon as a High Rate Capable Li-ion Battery Anode”. In: *Scientific Reports* 6 (2016), p. 33050.

[75] Peibo Gao et al. “Porous silicon from the magnesiothermic reaction as a high-performance anode material for lithium ion battery applications”. In: *Electrochimica Acta* 228 (2017), pp. 545–552.

[76] Kyoung Hwan Kim et al. “Complete magnesiothermic reduction reaction of vertically aligned mesoporous silica channels to form pure silicon nanoparticles”. In: *Scientific Reports* 5 (2015), p. 9014.

[77] Yu Zhou et al. “Scalable synthesis of Si/SiO2@C composite from micro-silica particles for high performance lithium battery anodes”. In: *Powder Technology* 284 (2015), pp. 365–370.

[78] Mahmut Dirican et al. “Flexible binder-free silicon/silica/carbon nanofiber composites as anode for lithium–ion batteries”. In: *Electrochimica Acta* 169 (2015), pp. 52–60.

[79] Dmitry Novikov et al. “Electrochemical performance and surface chemistry of nanoparticle Si@SiO2 Li-ion battery anode in LiPF6-based electrolyte”. In: *Electrochimica Acta* 208 (2016), pp. 109–119.

[80] Soojin Sim et al. “Critical Thickness of SiO2Coating Layer on Core@Shell Bulk@Nanowire Si Anode Materials for Li-Ion Batteries”. In: *Advanced Materials* 25.32 (2013), pp. 4498–4503.

[81] Xianhua Hou et al. “High yield and low-cost ball milling synthesis of nano-flake Si@SiO2 with small crystalline grains and abundant grain boundaries as a superior anode for Li-ion batteries”. In: *Journal of Alloys and Compounds* 639 (2015), pp. 27–35.

[82] Jing Wang et al. “Nano-sized SiOx/C composite anode for lithium ion batteries”. In: *Journal of Power Sources* 196.10 (2011), pp. 4811–4815.

[83] Mingqi Li et al. “Fabrication of graphene nanoplatelets-supported SiOx-disordered carbon composite and its application in lithium-ion batteries”. In: *Journal of Power Sources* 293 (2015), pp. 976–982.

[84] Qianjun He et al. “A novel mesoporous carbon@silicon–silica nanostructure for high-performance Li-ion battery anodes”. In: *Chem. Commun.* 50.90 (2014), pp. 13944–13947.

[85] Jiguo Tu et al. “Straightforward Approach toward SiO2Nanospheres and Their Superior Lithium Storage Performance”. In: *The Journal of Physical Chemistry C* 118.14 (2014), pp. 7357–7362.

[86] Joong-Yeon Kim et al. "Facile synthesis and stable cycling ability of hollow submicron silicon oxide–carbon composite anode material for Li-ion battery". In: *Journal of Alloys and Compounds* 633 (2015), pp. 92–96.

[87] Xifei Li et al. "Nanoporous tree-like SiO2 films fabricated by sol–gel assisted electrostatic spray deposition". In: *Microporous and Mesoporous Materials* 151 (2012), pp. 488–494.

[88] Pengpeng Lv et al. "Facile preparation and electrochemical properties of amorphous SiO2/C composite as anode material for lithium ion batteries". In: *Journal of Power Sources* 237 (2013), pp. 291–294.

[89] Zhiming Xiang et al. "Submicro-sized porous SiO2/C and SiO2/C/graphene spheres for lithium ion batteries". In: *Journal of Solid State Electrochemistry* (2017).

[90] Huan-Huan Li et al. "Dual-Porosity SiO2/C Nanocomposite with Enhanced Lithium Storage Performance". In: *The Journal of Physical Chemistry C* 119.7 (2015), pp. 3495–3501.

[91] Mingqi Li et al. "Nanosilica/carbon composite spheres as anodes in Li-ion batteries with excellent cycle stability". In: *J. Mater. Chem. A* 3.4 (2015), pp. 1476–1482.

[92] Hideharu Takezawa et al. "Electrochemical behaviors of nonstoichiometric silicon suboxides (SiOx) film prepared by reactive evaporation for lithium rechargeable batteries". In: *Journal of Power Sources* 244 (2013), pp. 149–157.

[93] Alireza Ostadhossein et al. "Atomic Insight into the Lithium Storage and Diffusion Mechanism of SiO2/Al2O3Electrodes of Lithium Ion Batteries: ReaxFF Reactive Force Field Modeling". In: *The Journal of Physical Chemistry A* 120.13 (2016), pp. 2114–2127.

[94] J. Saint et al. "Towards a Fundamental Understanding of the Improved Electrochemical Performance of Silicon–Carbon Composites". In: *Advanced Functional Materials* 17.11 (2007), pp. 1765–1774.

[95] Yuefei Zhang et al. "Lithiation of SiO2in Li-Ion Batteries: In Situ Transmission Electron Microscopy Experiments and Theoretical Studies". In: *Nano Letters* 14.12 (2014), pp. 7161–7170.

[96] A. R. WEST et al. "Ionic conductivity of oxides based on Li4SiO4". In: *Journal of applied electrochemistry 3* (1973), pp. 327–334.

[97] François Béguin et al. *Carbons for electrochemical energy storage and conversion systems*. CRC Press, 2010, pp. 275–276.

[98] Yu Yao et al. "Carbon-coated SiO2 nanoparticles as anode material for lithium ion batteries". In: *Journal of Power Sources* 196.23 (2011), pp. 10240–10243.

[99] Huiqiao Li and Haoshen Zhou. "Enhancing the performances of Li-ion batteries by carbon-coating: present and future". In: *Chem. Commun.* 48.9 (2012), pp. 1201–1217.

[100] Haitao Zhou et al. "High capacity nanostructured Li2FexSiO4/C with Fe hyperstoichiometry for Li-ion batteries". In: *Journal of Power Sources* 235 (2013), pp. 234–242.

[101] Dusan Losic et al. "Atomic force microscopy (AFM) characterisation of the porous silica nanostructure of two centric diatoms". In: *Journal of Porous Materials* 14.1 (2006), pp. 61–69.

[102] Nils Kroger et al. "Diatom cell wall proteins and the cell biology of silica biomineralization". In: *Protist* 149.3 (1998), pp. 213–219.

[103] Tadashi Nakajima et al. "3, 4-Dihydroxyproline: a new amino acid in diatom cell walls". In: *Science* 164.3886 (1969), pp. 1400–1401.

[104] Anna-Maria Schmid et al. "Wall morphogenesis in diatoms: deposition of silica by cytoplasmic vesicles". In: *Protoplasma* 100.3 (1979), pp. 267–288.

[105] François Béguin et al. *Carbons for electrochemical energy storage and conversion systems*. CRC Press, 2010, p. 16.

[106] Christian Julien et al. *Materials for Lithium-ion Batteries*. Kluwer Academic Publishers, NATO Scientific Affairs, 2000, p. 529.

[107] Fritz Scholz et al. *Electroanalytical methods*. Vol. 1. Springer, 2010, p. 159.

[108] François Béguin et al. *Carbons for electrochemical energy storage and conversion systems*. CRC Press, 2010, p. 24.

[109] Fritz Scholz et al. *Electroanalytical methods*. Vol. 1. Springer, 2010, p. 168.

[110] Eliezer Gileadi et al. *Physical electrochemistry: fundamentals, techniques and applications*. Wiley, 2011, p. 241.

[111] Ib Chorkendorf et al. *Concepts of modern catalysis and kinetics*. John Wiley & Sons, 2015, pp. 183–187.

[112] Kiyoshi Nogi et al. *Nanoparticle technology handbook*. Elsevier, 2012, p. 299.

[113] David Brandon et al. *Microstructural Characterization of Materials*. Whiley, 2008.

[114] Nan Yao. *Focused ion beam systems: basics and applications*. Cambridge University Press, 2007, p. 10.

[115] Nan Yao. *Focused ion beam systems: basics and applications*. Cambridge University Press, 2007, p. 31.

[116] Mario Marinaroand others. "Toward pre-lithiatied high areal capacity silicon anodes for Lithium-ion batteries". In: *Electrochimica Acta* 206 (2016), pp. 99–107.

[117] JC Burns et al. "Introducing symmetric Li-ion cells as a tool to study cell degradation mechanisms". In: *Journal of The Electrochemical Society* 158.12 (2011), A1417–A1422.

[118] *User Manual ECC-Ref*. URL: `https://el-cell.com/wp-content/uploads/downloads/manuals/Manual_ECC-Ref_Release_2.43.pdf` (visited on 06/18/2017).

[119] Hiroshi Fukui et al. "A Si-O-C Composite Anode: High Capability and Proposed Mechanism of Lithium Storage Associated with Microstructural Characteristics". In: *ACS Applied Materials & Interfaces* 2.4 (2010), pp. 998–1008.

[120] D Mazouzi et al. "New insights into the silicon-based electrode's irreversibility along cycle life through simple gravimetric method". In: *Journal of Power Sources* (2012), pp. 180–184.

[121] Ran Elazari et al. "Li ion cells comprising lithiated columnar silicon film anodes, TiS2 cathodes and fluoroethyene carbonate (FEC) as a critically important component". In: *Journal of The Electrochemical Society* 159.9 (2012), A1440–A1445.

[122] Kaland Henning. "On the Cycling Performance and Stability of Silicon-Based Anodes in Lithium-Ion Batteries". MA thesis. NTNU, 2017.

Appendix

A1 Supplementary notes on experimental work

A1.1 Slurry preparation

A1.1.1 Actual composition used for carbon coating

The actual compositions used under the carbon coating procedure of SiO_2 and for the fabrication of pyrolysed carbon are presented in Table A1.

Table A1: Actual compositions of SiO_2, carbon precursor and solvent used.

Batch	SiO_2 [g]	Carbon precursor	[g]	Solvent	[g]
Cornstarch coated SiO_2	0.2400	Cornstarch	0.9609	Ethanol	6.5
Sucrose coated SiO_2	0.2799	Sucrose	1.1203	DI-Water	7.2
Sucrose coated milled SiO_2	0.2002	Sucrose	0.7996	DI-Water	3
Pyrolysed cornstarch	-	Cornstarch	2.00	Ethanol	2
Pyrolysed sucrose	-	Sucrose	3.5086	DI-Water	4

A1.1.2 Actual Slurry Compositions

An overview of the actual composition of the caste produced is found in Table A2. What constitutes the active material in the individual casts can be seen in section 3.4, Table 3.1. Alg gel represents the amount of the gelled alginate used, while Alg pow. constitutes the amount of Na-alg powder in that volume of alg gel.

Table A2: Actual composition of casts.

Cast	Alg gel [g]	Alg pow. [g]	Active material [g]	CB [g]	CNT [g]
P-25CB	3.0216	0.0504	0.2006	0.0833	-
P-35CB	3.0112	0.0502	0.1667	0.1167	-
PM-35CB	3.0103	0.0502	0.1667	0.1159	-
C-25CB	4.0200	0.0670	0.2660	0.1112	-
S-25CB	4.0126	0.0668	0.2668	0.1111	-
SM-35CB	2.9966	0.0500	0.1665	0.1166	-
P-35CBCNT	3.0073	0.0501	0.1661	0.0501	0.0584
PM-35CBCNT	3.0071	0.0501	0.1671	0.0582	0.0582
Si25	4.0101	0.0668	0.0667 Si + 0.1999 $CSiO_2$	0.1115	-
Si50	3.0484	0.0508	0.1335 Si + 0.1327 $CSiO_2$	0.1111	-
Si75	3.0484	0.0508	0.2005 Si + 0.0665 $CSiO_2$	0.1112	-
Si50M	3.0484	0.0508	0.0832 Si + 0.0833 SiO_2	0.0583	0.0583
CD	3 ml	0.0693	0.2350	0.1250	-
SD	4.0011	0.0667	0.2666	0.1105	-
CB	3.0172	0.0502	-	0.2838	-

A1.2 Electrolyte preparation

Actual amount of solvents used to fabricate the FEC electrolyte.

Table A3: Actual composition of prepared electrolyte

Nomencalture	Composition	Solvent [uL]
FEC	$\sim$ 0.94 M $LiPF_6$ in 47:47:5:1 ED:DEC:FEC:VC	$V_{Pre} = 3760$ $V_{FEC} = 200$ $V_{VC} = 40$

A2 Supplementary data on characterization of frustules and active material

A2.1 X-ray diffraction

Figure A1 show the XRD data from all batches prepared in this work. Some variation can be observed in the different batches. However, the same general observation can be made from each batch, no crystalline peaks can be observed and the broad peak at 22 ° representing SiO_2.

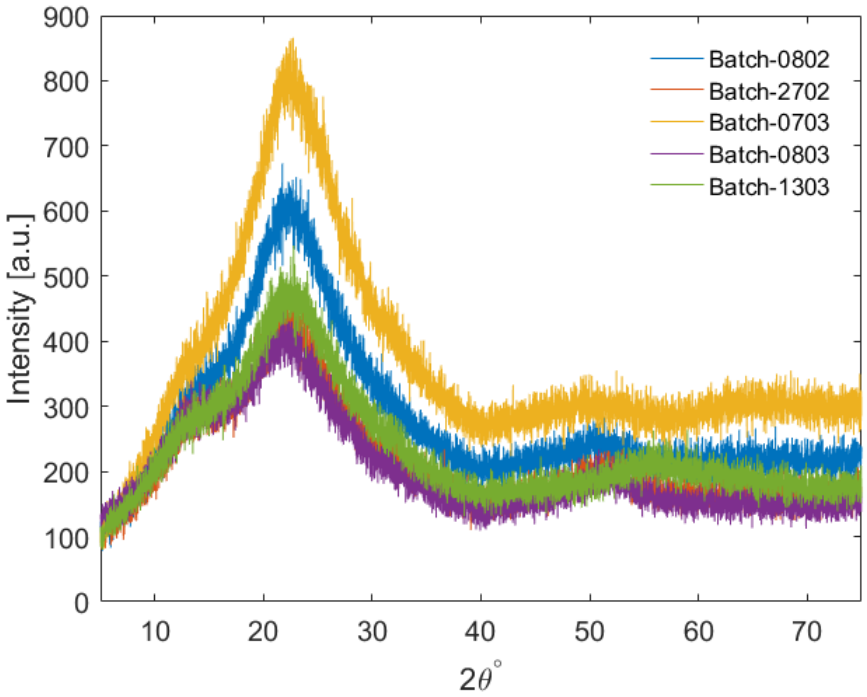

Figure A1: XRD diffractogram of all batches of extracted SiO_2.

A2.2 Laser diffraction

Figure A2 presents all the laser diffraction data from this work. To ensure some statistical significance three measurements were conducted for each sample. After the measurements, the sample was subjected 5 min additional ultrasound before 2 additional measurements were conducted. This was done to confirm that most of the agglomerates were removed by the pre ultrasonication.

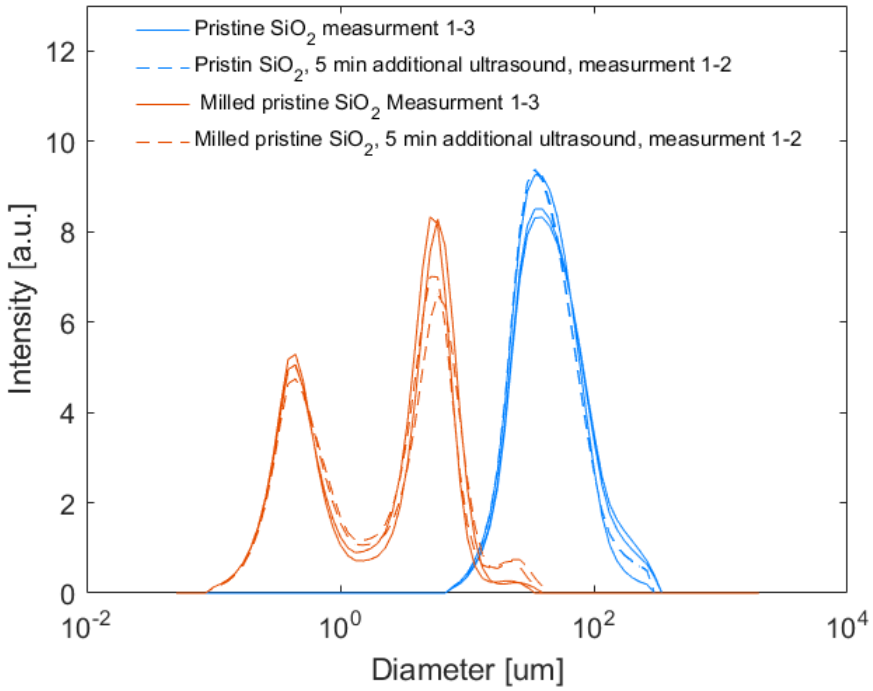

Figure A2: Overview of all measurements conducted by laser diffraction.

A2.3 SEM micrographs of diatoms

This section presents a more extensive collection of SEM micrographs of the extracted diatoms. The different layers was attempted identifies by comparing the micrographs to the AFM data coscinodiscus presented by Losic et al [101]. Suggestion for which layer the different micrographs show is written in the caption.

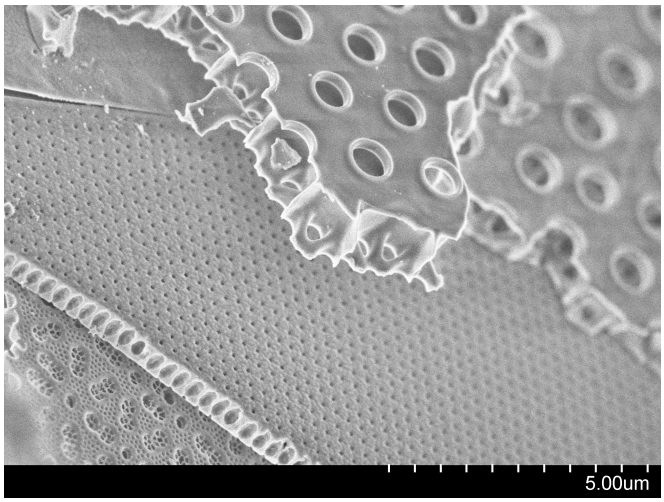

(a)

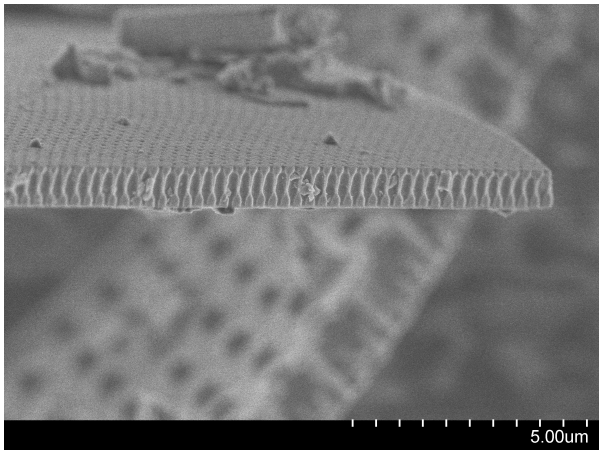

(b)

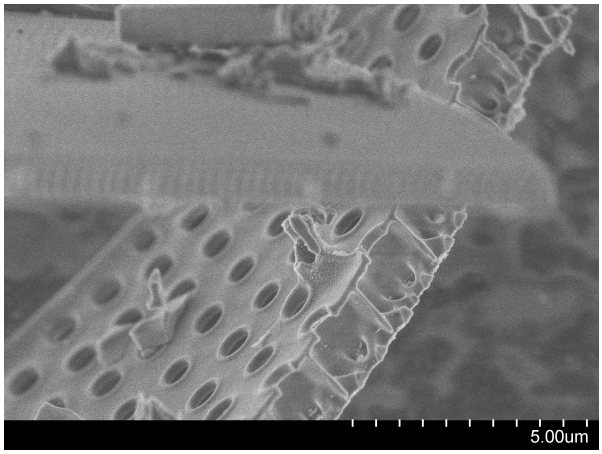

(c)

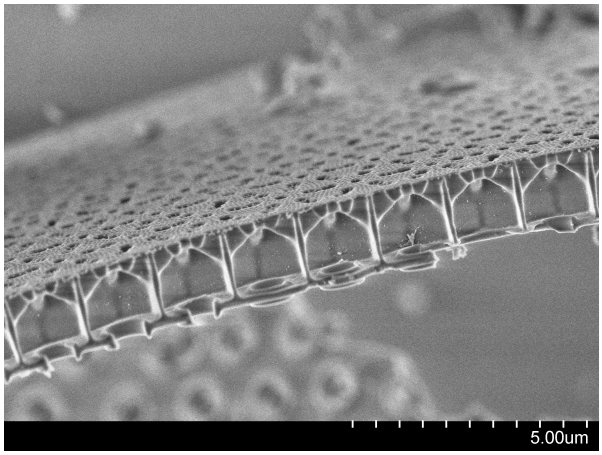

(d)

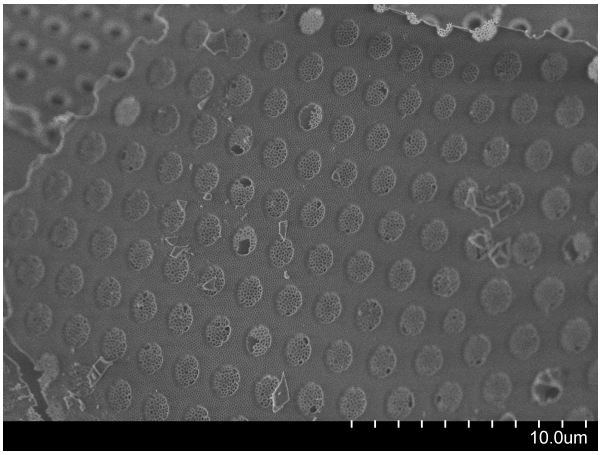

(e)

Figure A3: SEM micrographs of the diatom frustules. (a) Overview of multiple layers (b) potentially the cribrum layer, (c)-(d) the Cribellum layer and (e) possibly the foramen layer .

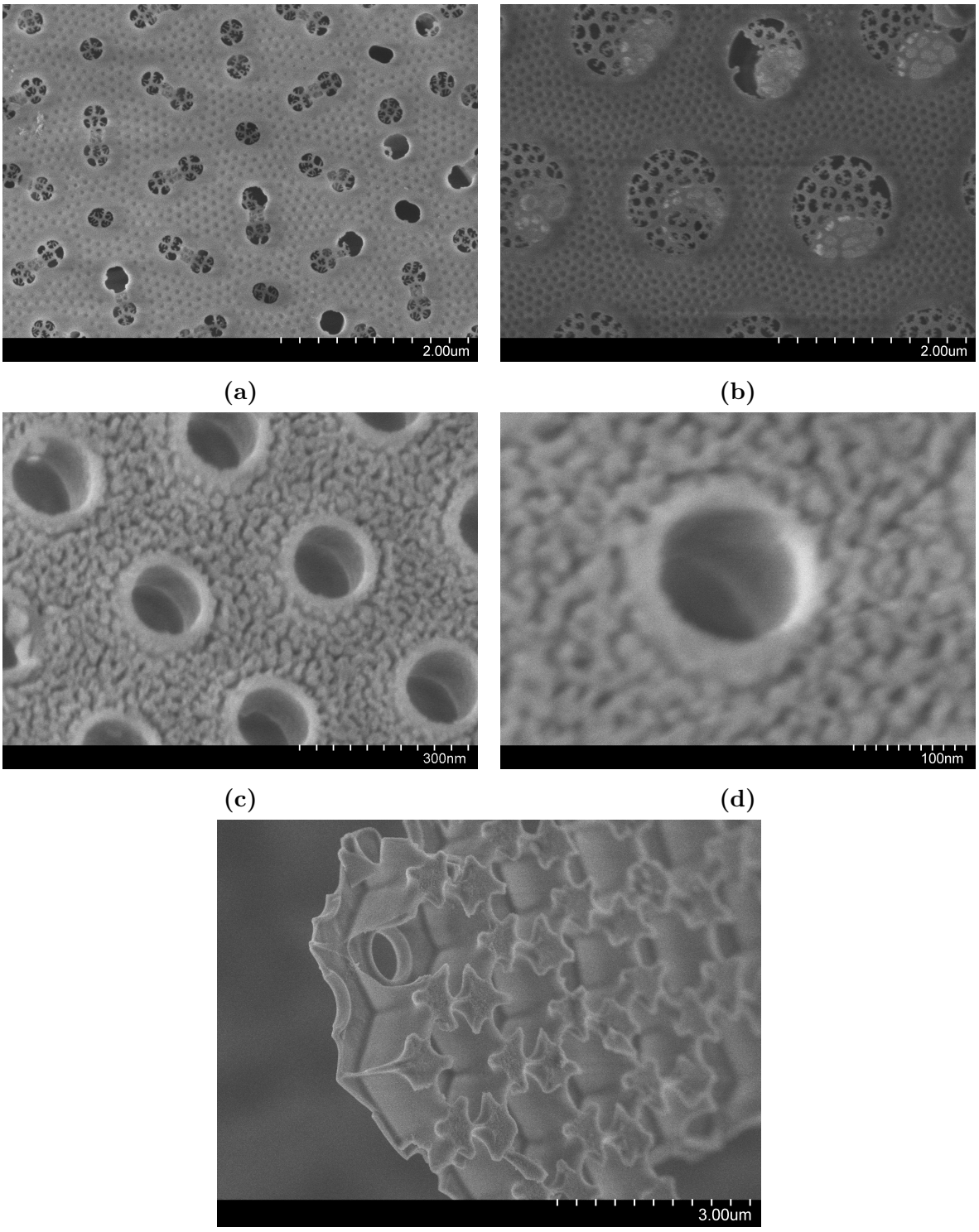

(a) **(b)** **(c)** **(d)** **(e)**

Figure A4: SEM micrographs of the different structures on the frustules. (a) Cribellum layer, (b) foramen, (c)-(d) porosity of unidentified structure, (e) bulk porosity of the cribellum layer.

A3 Experimental matrix for electrochemcial characterization

Table A4 shows an overview of cells assembled and cycled in phase 1 of this work.

Table A4: Experimental matrix for phase 1.

Material system	Galvanostatic Cycling (# cells, Program)	EIS	Rate	Loading [mgcm^{-1}]
Carbon Cells				
CD-25CB-EC	3x, L	-	-	0.30/0.27/0.27
SD-25CB-EC	3x, L	-	-	0.15/0.21/0.21
CB-EC	3x, L	-	-	0.21/0.21/0.21
SiO_2 Cells				
P-25CB-EC	1x, L	-	-	0.21
C-25CB-EC	1x, L	-	-	0.60
S-25CB-EC	1x, L	-	-	0.39
S-25CB-FEC	1x, L	-	-	0.45
P-35CB-EC	1x, L	-	-	0.30
P-35CB-EC	1x, L3	-	-	0.34
P-35CB-FEC	1x, L	-	-	0.20
P-35CBCNT-EC	1x, L	-	-	0.28
PM-35CB-EC	1x, L	-	-	0.23
PM-35CB-FEC	1x, L	-	-	0.23
PM-35CB-EC	1x, H48	-	-	0.15
SM-35CB-EC	1x, L	-	-	0.28
SM-35CB-FEC	1x, L	-	-	0.23
SM-35CB-EC	1x, H48	-	-	0.28
SiO_2/Si Cells				
Si25-25CB-EC	1x, L	-	-	0.36
Si50-25CB-EC	1x, L	-	-	0.33
Si75-35CB-EC	1x, L	-	-	0.33
Si50M-35CBNT-FEC	1x, L1	-	-	0.78

Table A5 shows an overview of cells assembled and cycled in phase 1 of this work.

Table A5: Experimental matrix for phase 2.

Material system	Galvanostatic Cycling (# cells, Program)	EIS	Rate	Loading [mgcm^{-1}]
Pristine SiO_2				
PM-35CB-EC	1x, H132	-	-	0.23
PM-35CB-EC	2x, H48	1x	1x	0.2, All Cells
PM-35CB-FEC	2x, H48	1x	1x	0.2, All Cells
Carbon coated SiO_2				
SM-35CB-EC	2x, H48	1x	1x	0.2, All Cells
SM-35CB-FEC	2x, H48	-	1x	0.2, All Cells
Reference				
P-35CB-EC	3x, L	-	-	0.2, All Cells

A4 Supplementary data on electrochemical characterization

A4.1 Voltage profiles.

Figure A5a, A5b show the voltage profile of PM-35CB-EC/H48 and P-35CB-EC/L. PM-35CB-EC/H48, which has undergone electrochemical reduction, show an increase in the length of the plateaus initiated at approximately 0.25 V.

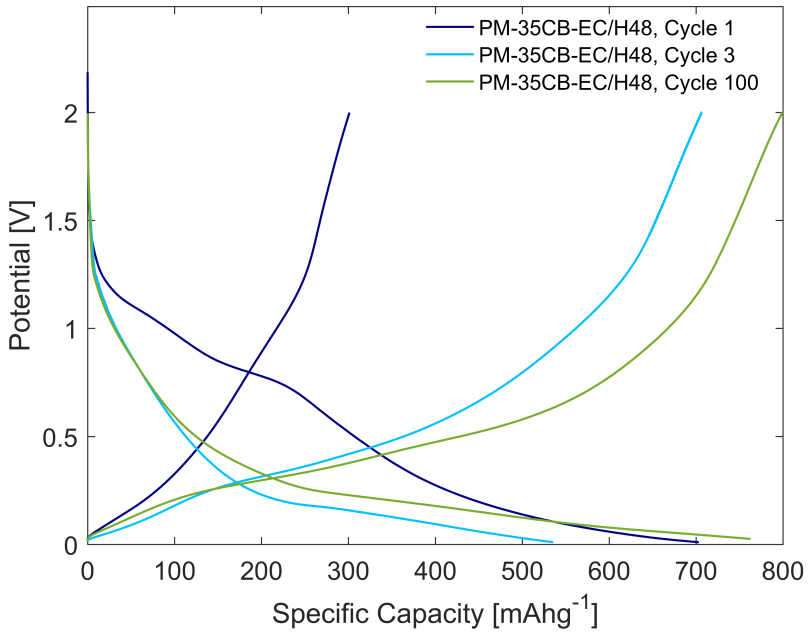

(a)

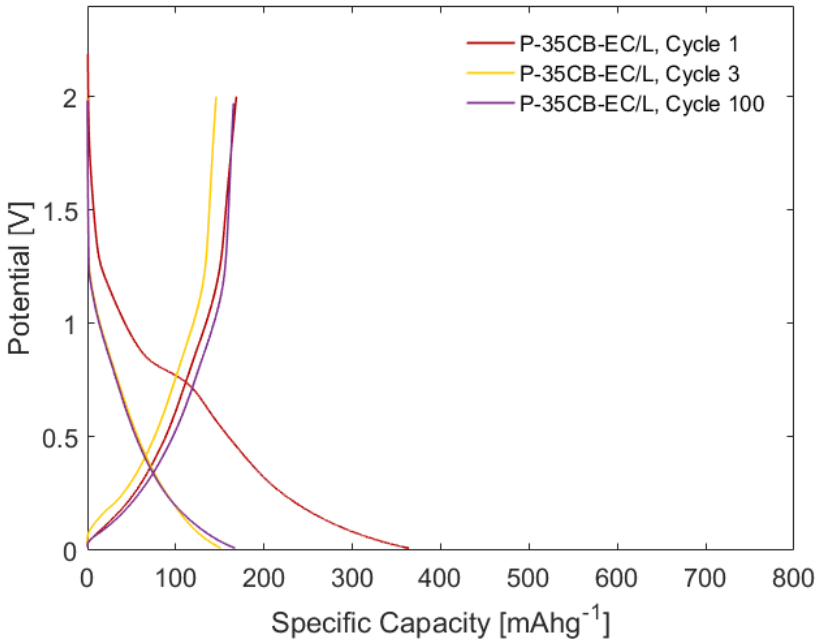

(b)

Figure A5: Voltage profile of cycle 1, cycle 2 and cycle 3 for (a) P-35CB-EC/L and (b) PM-35CB-EC/H48.

A4.2 Additional capacity plots from phase 1

Figure A6a, A6b, show Figure 4.7c,4.7d with additional cells. In Figure A6a, the limited effect electrolyte composition had on cells with umilled SiO_2 (S-25CB-EC/L and P-35CB-EC/l) can be seen. In Figure A6b, milling can be seen to increase the capacity of both carbon coated and prestine SiO_2. However, the effect appears to be greater in carbon coated SiO_2 (SM-35CB-EC/L).

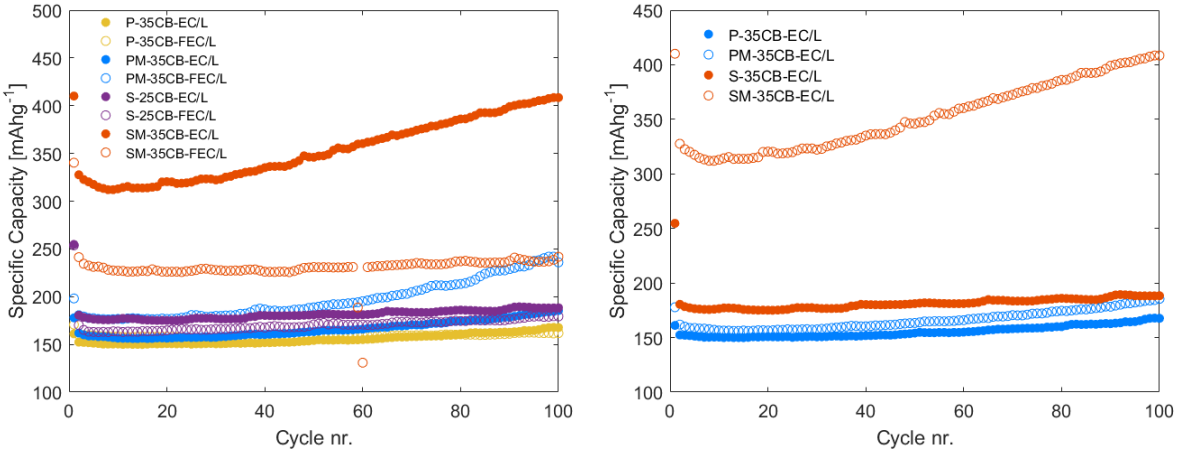

Figure A6: Additional Phase 1 capacity plots. (a) Cells with the same electrode composition but different electrolytes, (b) cell with milled and unmilled SiO_2.

A4.3 Additional plots of the coulombic efficiency of cells in phase 2

Figure A7 presents the average CE of cells in phase 2. Error bars show one standard deviation. Tabulate values of selected cycles can be found in Table A6.

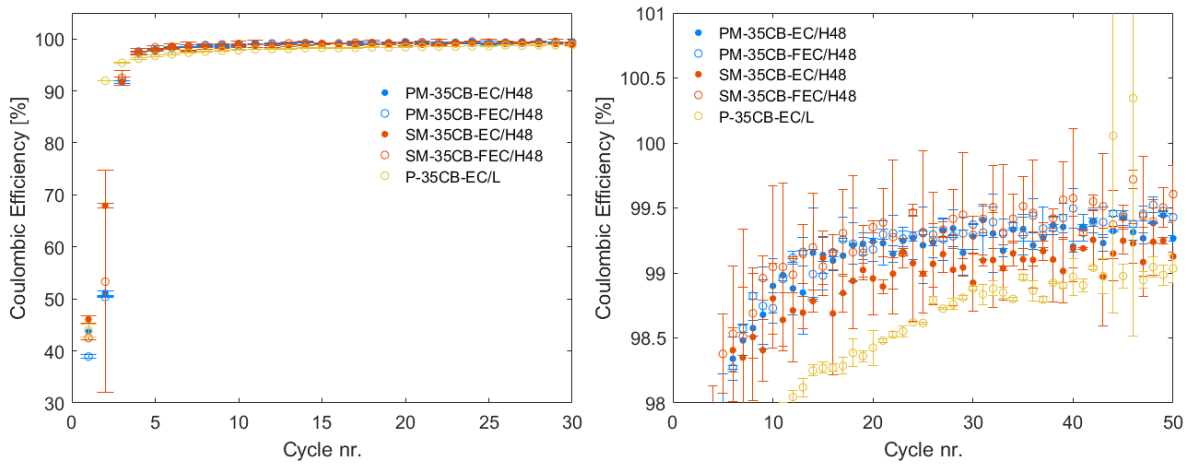

Figure A7: Average Coulombic efficiency of cells in phase 2. (a) General trend of the coulombic efficiency of all 50 cycle. (b) Enlarged view of (a). Error bars show one standard deviation.

Table A6: Average coulombic efficiency of all cells in phase 2. Uncertainty is given as ± one standard deviation

Cycle	PM-35CB-EC/H48	PM-35CB-FEC/H48	SM-35CB-EC/H48	SM-35CB-FEC/H48
	Coulombic E. [%]	Coulombic E.[%]	Coulombic E.[%]	Coulombic E.[%]
1	43.68 ± 1.494	38.91 ± 0.3551	46.06 ± 0.7404	42.47 ± 0.2477
2	51.15 ± 0.4462	50.36 ± 0.1041	67.91 ± 0.3881	52.32 ± 21.27
3	91.63 ± 0.2671	92.02 ± 0.0029	91.84 ± 0.7668	92.51 ± 1.343
10	98.90 ± 0.2080	98.73 ± 0.1173	98.80 ± 0.2722	99.05 ± 0.6245
50	99.26 ± 0.0197	99.43 ± 0.0293	99.13 ± 0.0341	99.61 ± 0.2201

A4.4 Electrochemical impedance spectroscopy

Figure A8 sow the Nyquist plot of PM-35CB-EC/H48, PM-35CB-FEC/H48, SM-35CB-EC/H48 in both lithiated and delithiated state, for all cycles EIS was conducted. EIS was not conducted on SM-35CB-FEC/H48 due to limited time.

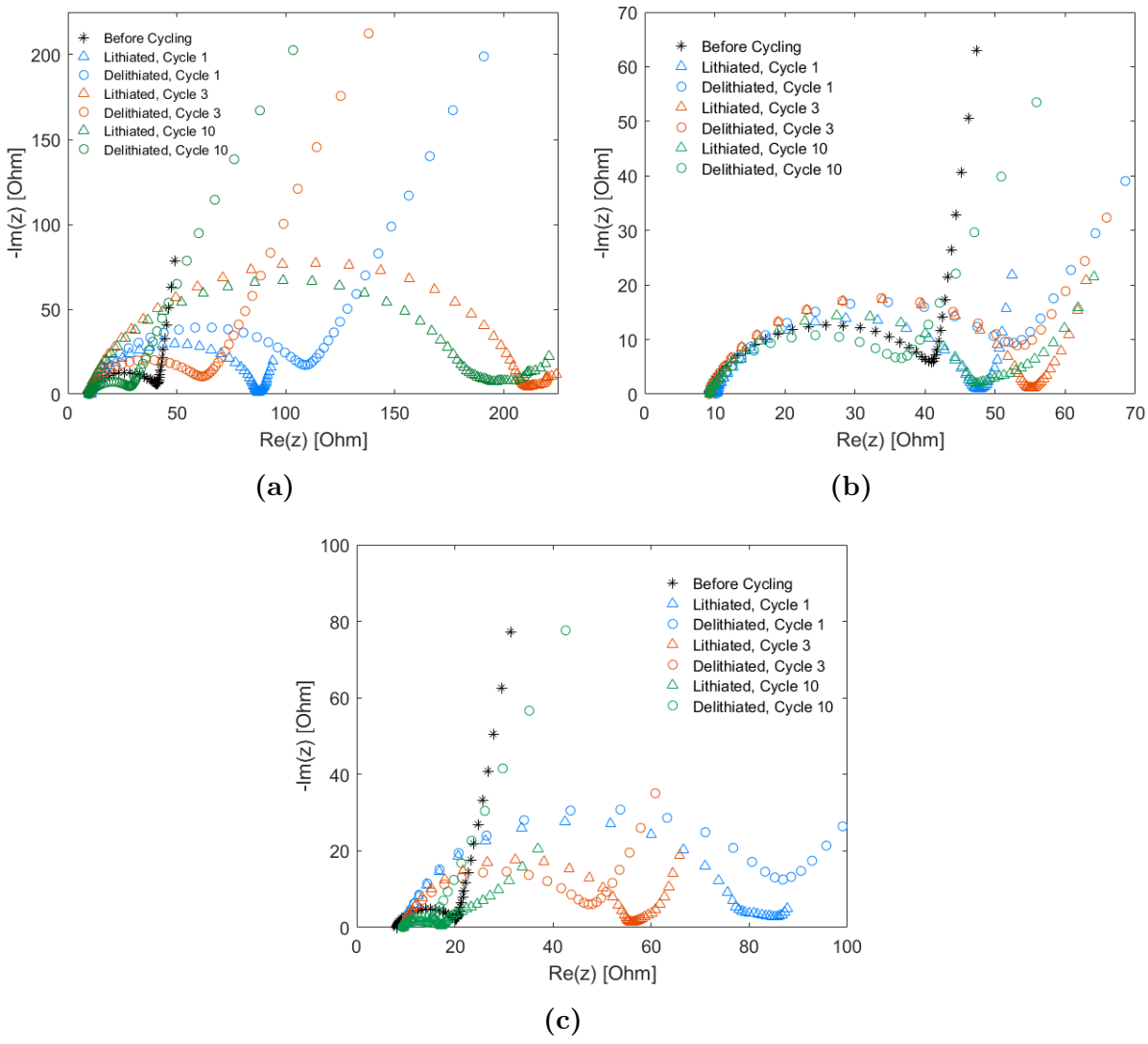

Figure A8: Nyquist plot of three electrode cells with different anode and electrolyte composition. (a)PM-35CB-EC/H48, (b) PM-35CB-FEC/H48 and (c) SM-35CB-EC/H48.

A5 Supplementary SEM micrografs of electrodes

A5.1 Additional SEM micrographs of electrode surfaces

This section show additional SEM micrographs of electrode surfaces from cells in phase 2. As stated in section 4.4.1.1, limited crack formation is observed in every electrode. The amount of cracks and the crack depth, appears to be of the same order in all electrodes. Some limited differences can be observed. However, these difference is not large enough to exclude the possibility of them being formed by differences in brightness/contrast levels, different surface films and local differences in surface morphology.

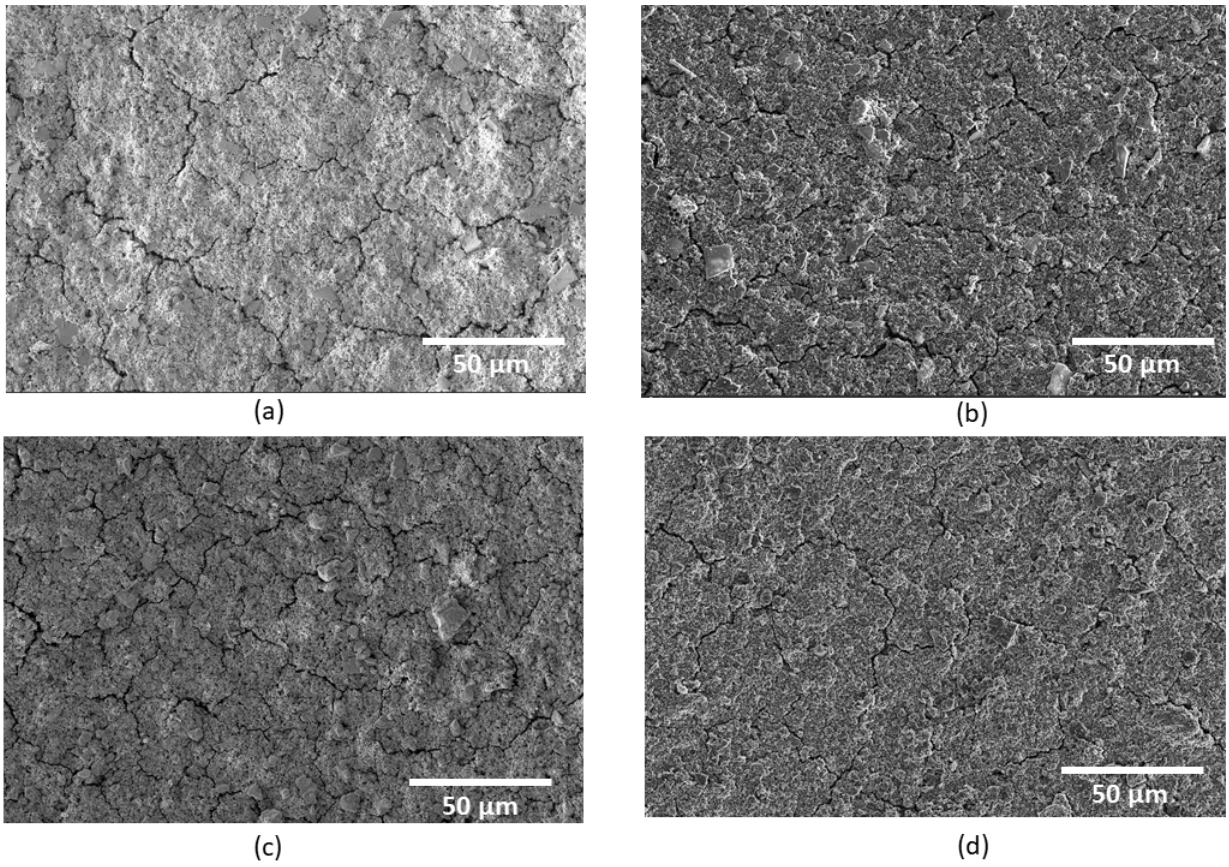

Figure A9: SEM images of cycled electrodes (a) PM-35CB-EC/H48, (b) PM-35CB-EC/H48 (c) SM-35CB-EC/H48 (d) SM-35CB-FEC/H48

A5.2 Removal of SEI layer on electrode surface structure

Figure A10a show a SiO_2 particle on a SM-35CB-FEC/H48 electrode after 50 cycles. By exposing the surface to a high potential/high current electron beam, the surface film was removed. The removal of the surface film confirm that the covered structures observed in SM-35CB-EC/H48 and SM-35CB-FEC/H48 (Figure 4.22) indeed are SiO_2 structures with thick film formation.

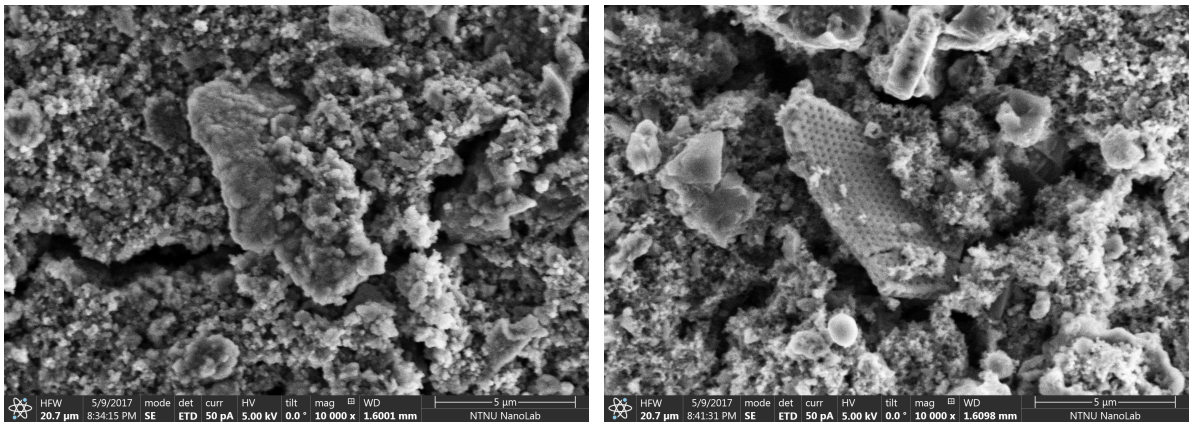

(a) **(b)**

Figure A10: (a) Structure observed on SM-35CB-FEC/H48 electrode surface after cycling.(b) Same structure as in (a), now exposed to a high voltage/current electron beam.

A6 Supplementary EDX spectra

EDX was used to to estimate the fluorine composition of the electrode surface after cycling. This was done by comparing the cps of fluorine in the EDX measurements of the electrodes seen in Figure A11-A14. The noted values can be found in Table 4.11 in section 4.4.2. Figures A11-A14(a) show the EDX spectra of all electrodes in phase 2 after cycling. Figure A11-A14(b) show a close-view of the fluorine peaks.

It should be noted that these kind of measurements are inherently uncertain. However, as the same WD, acceleration voltage and electron current were used, the results could be indicative of the actual fluorine content. It should also be noted that the wt % should not be used as an estimate of the actual wt % of fluorine, as this value also is dependent on the cps from other elements.

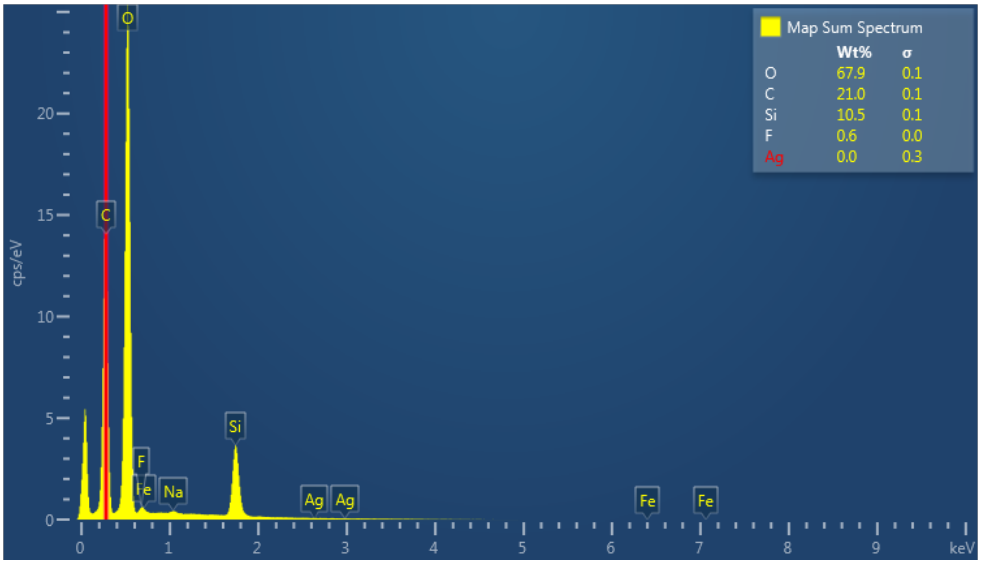

(a)

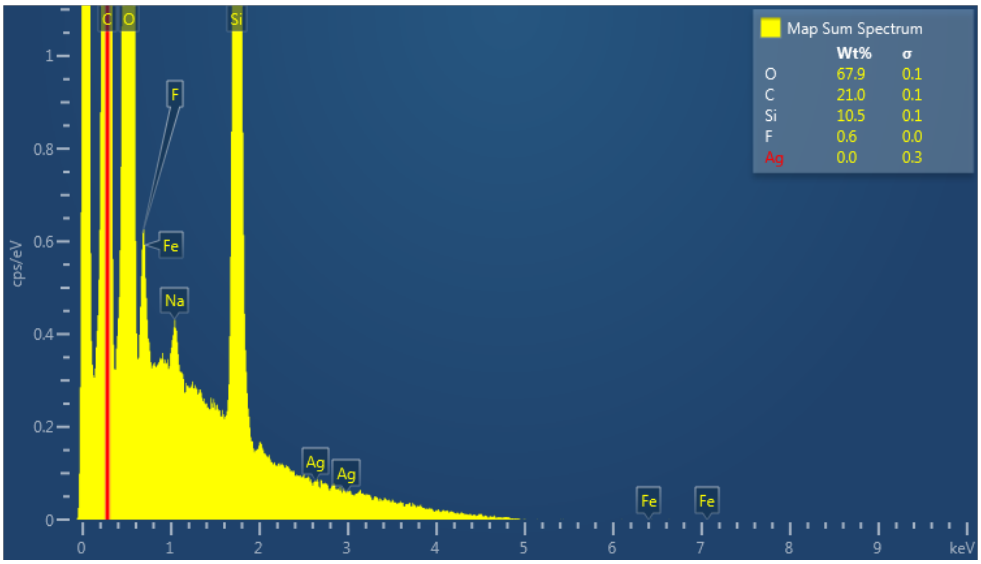

(b)

Figure A11: EDX mapping of PM-35CB-EC/H48 surface after cycling. (a) Full EDX spectrum, (B) close up of fluorine peak.

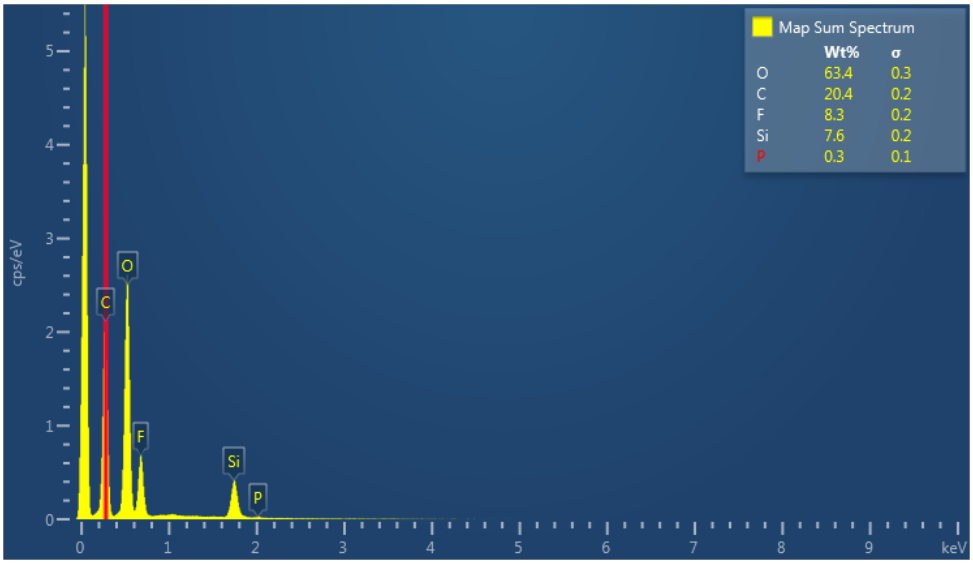

(a)

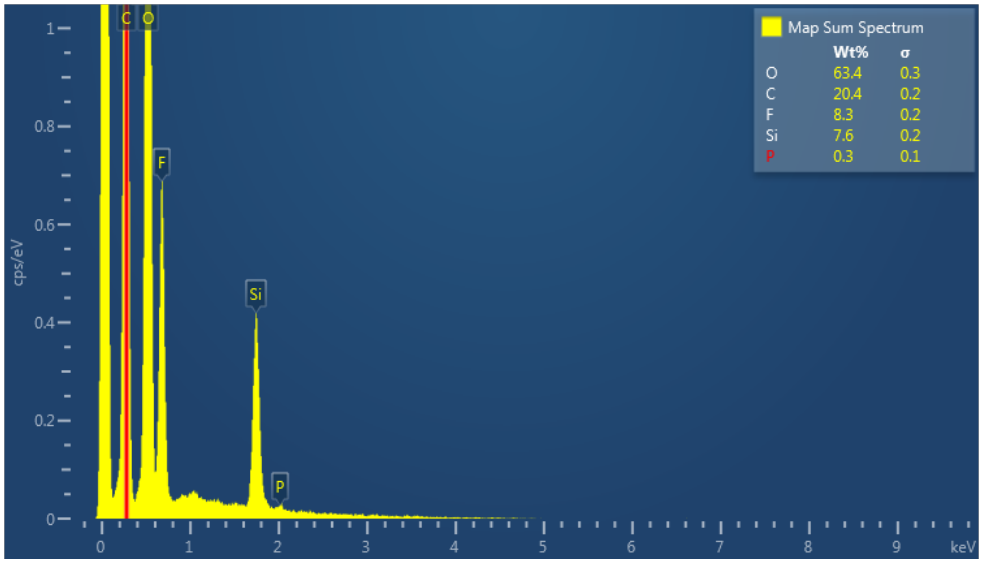

(b)

Figure A12: EDX mapping of PM-35CB-FEC/H48 surface after cycling.(a) Full EDX spectrum, (B) close up of fluorine peak.

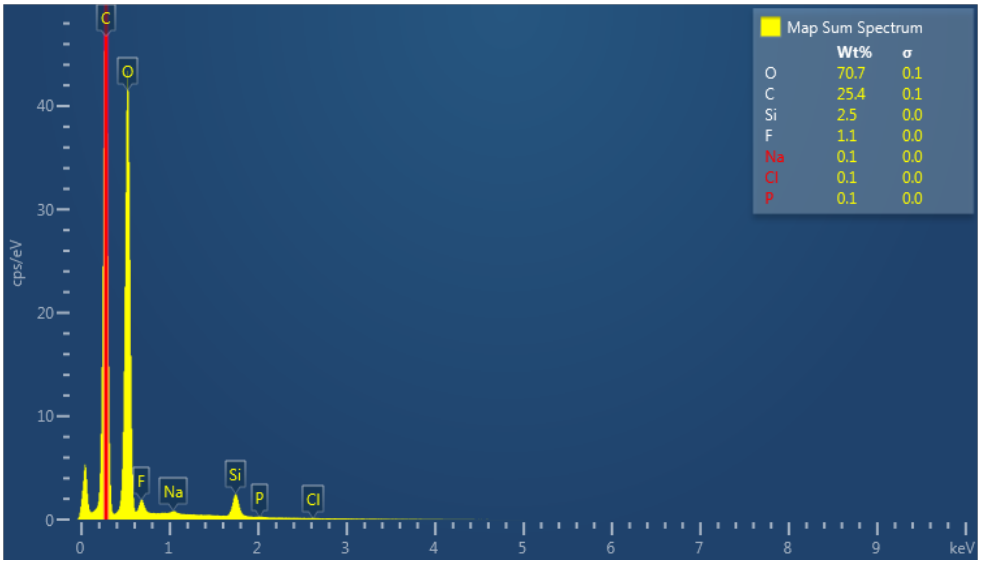

(a)

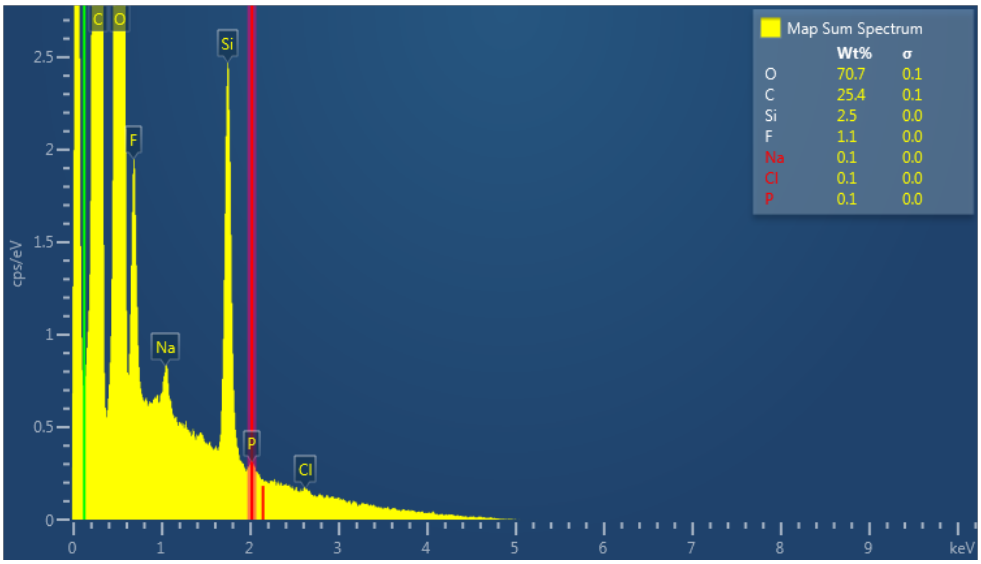

(b)

Figure A13: EDX mapping of SM-35CB-EC/H48 surface after cycling. (a) Full EDX spectrum, (B) close up of fluorine peak.

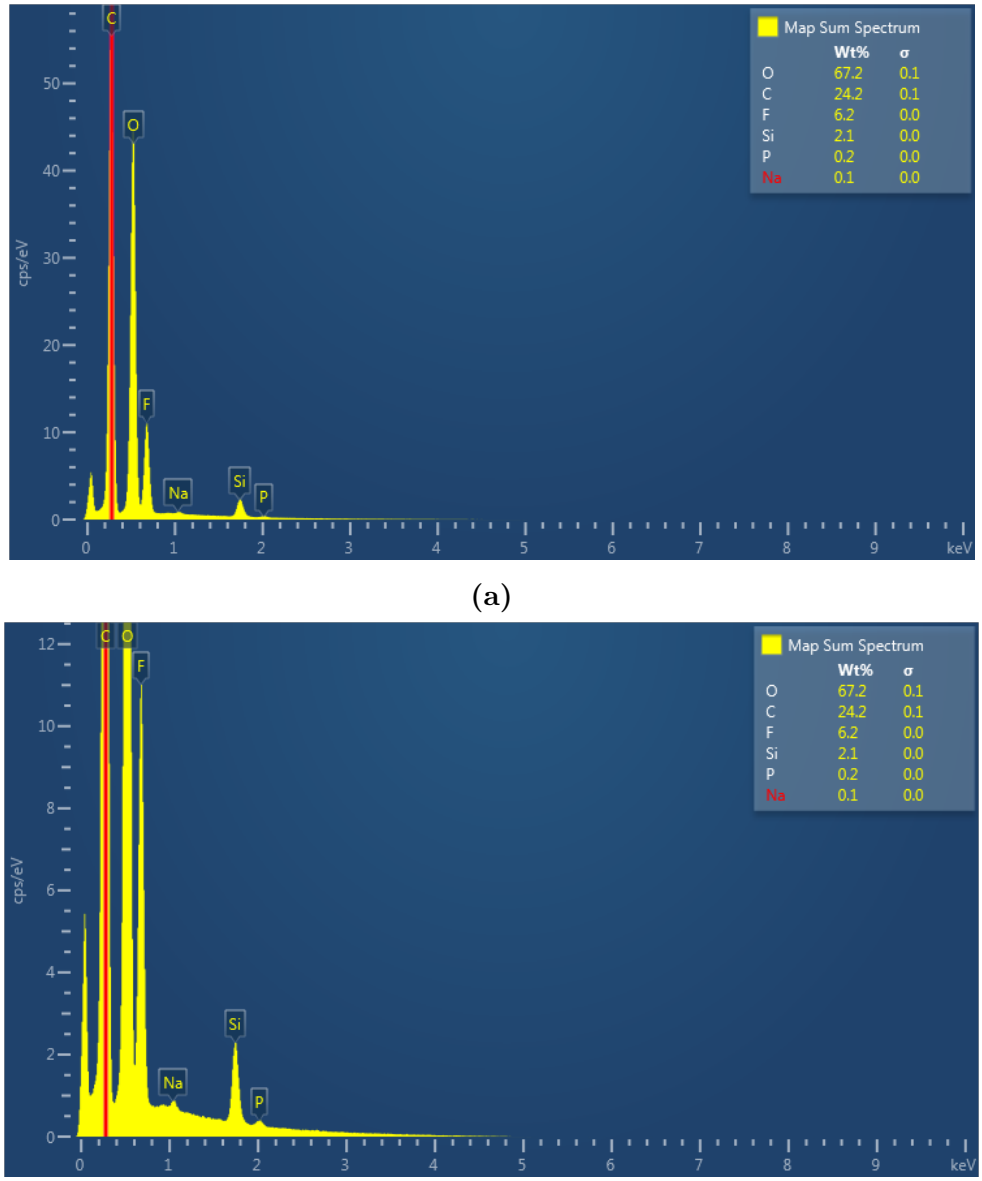

(a)

(b)

Figure A14: EDX mapping of SM-35CB-FEC/H48 surface after cycling. (a) Full EDX spectrum, (B) close up of fluorine peak.

A7 Notes on Si anodes and collaboration with Henning Kaland

This work was done in parallel with master students Henning Kalands work on Si anodes [122]. Due to the similarities of SiO_2 anodes and Si anodes, a collaboration was initiated. This include the casting of SiO_2/Si composites and sharing of data that was found valuable to the other.

In terms of the collaboration on SiO_2/Si composites, preprocessing of the SiO_2 was done by the author, while pre processing of the Si was done by Kaland. The composition of the casts and the cycling parameters were decided after a common discussion, and prepared and assembled together. In addition, Kaland was gracious enough to help with the milling of SiO_2 and to supply data from galvanostatic cycling of Si anodes. Differential capacity analysis was conducted on this data, and it was used to compare the lithiation potentials of SiO_2 to Si.

Differential capacity curve of Si anode

The differential capacity curve presented in this section is based on galvanostatic cycling conducted by Henning Kaland [122]. However, the differential capacity analysis were conducted by the author according to the same procedure described in the experimental chapter, section 3.7.1.

The differential capacity curve of an Si anode can be seen in Figure A15. Two distinct peaks can be observed in both the anodic and cathodic direction. Two anodic peaks at 0.26 V and 0.43 V, and two cathodic peaks at 0.09 V and 0.25 V. The two peaks can probably be described by the different lithiation potentials of the Li_xSi phases described in section 2.3.2.

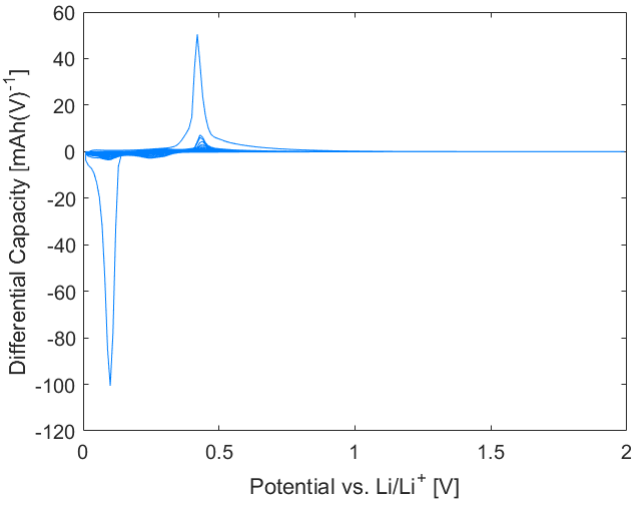

(a)

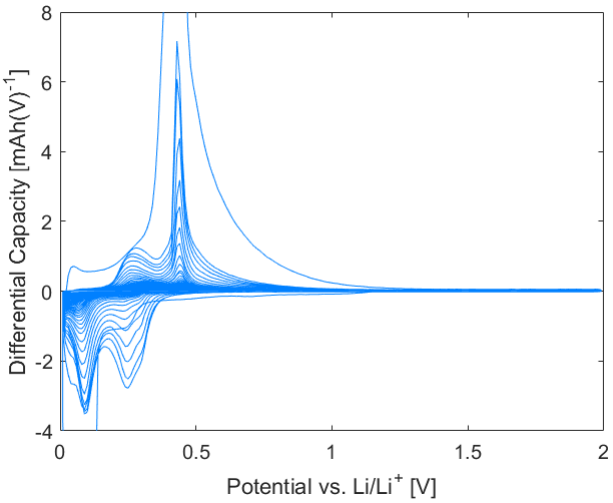

(b)

Figure A15: (a) Differential capacity plot of Si anode. (b) Up close view of (a). Resolution of plot is $\Delta E = 10$ mV.

Notes on Si50M

Based on the limited cycling stability of Si25, Si50 and Si75, a new composite cast, Si50M, was prepared. A buffered CMC solution was used in an attempt to improve the bonds between the Si particles and the binder. This binder was prepared by Kaland, and a description of the preparation process can be found in his work [122].